Final Report

UAS for Post-Fire Forensic Investigation and Scene Mapping

AE3200: Design Synthesis

Group 23: Fire-Eye

Delft University of Technology

TU Delft

Final Report: Fire-Eye

UAS for Post-Fire Forensic Investigation and Scene Mapping

by

Ameen, Amran	5578620
Brunner, Olivier	5552222
Dahmen, Daniel	5491762
Delnoij, Niels	5768233
Keating, Nina	5728924
Ma, Di-Kun	5547172
Sabel, Jasper	5473640
Torreño Diez, Helena	5695325
Wassenaar, Maas	5299470
Zaheer, Nabihah	5694582

Course Coordinator:	Ir. J. Melkert
Principle Tutor:	Prof.dr.ir. R. Benedictus
Coaches:	T. Eker & S. Wang
Clients:	Dr. H. Mickleburgh (UVA)
	Prof.dr. M. Aalders (UVA)
Faculty:	Faculty of Aerospace Engineering, Delft
Date:	June 24, 2025
Version Number:	2
Cover:	Original work by Nabihah Zaheer

TU Delft

Executive Overview

This report aims to provide the reader with a compelling design for an Unmanned Aerial System (UAS) design, which is designed to revolutionize forensic research and mapping in structurally-compromised buildings. This is made possible through the design and operation of a modular quadcopter used for the Fire-Eye mission.

Project Overview

The Mission Need Statement and the Project Objective Statement were formulated in a previous report[1]. To restate these:

Mission Need Statement: There is a need to conduct forensic investigations, map interiors, and locate human remains in confined and structurally compromised post-fire interiors, without human presence.

Project Objective Statement: To develop a compact, unmanned system operating in fire-damaged structures, providing spatial mapping and detecting human remains using UV-fluorescence, while minimizing environmental disturbances, by 10 students in 10 weeks.

Operations and Logistics

Operational procedures, and the logistics that support them, are central to the practical deployment of Fire-Eye in real-world use cases. By setting out the system's full mission cycle, from storage to deployment, operation, maintenance and return, key integration points with existing infrastructure can be identified, and areas where new infrastructure may be required can be flagged.

Figure 1 illustrates the operational and logistical concept for the Fire-Eye system, depicting the 16 phases of a standard mission, including storage, transport and maintenance, as well as operations. Each phase has been designed with compatibility in mind, ensuring that Fire-Eye can be embedded within current forensic and emergency response frameworks with minimal new infrastructure required.

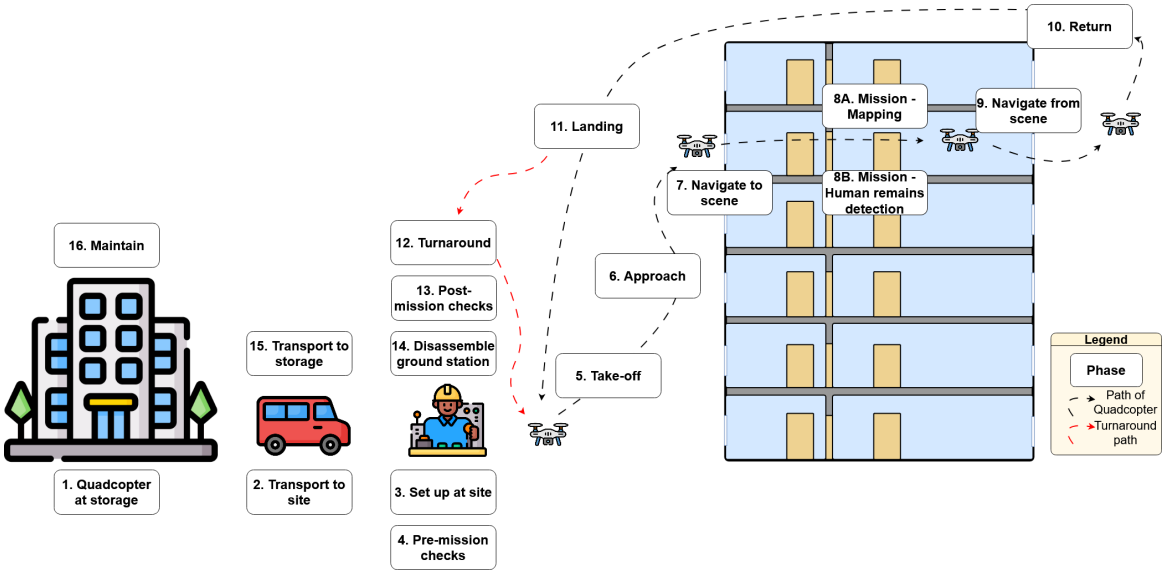

Figure 1: Operations and logistics concept diagram

The mission begins from storage, moves through deployment and operations, and finishes with inspections and maintenance or return to storage. Most phases rely on existing vehicles, facilities and operational practices, such as storage areas and secured perimeters. Where new capabilities are required, efforts are made to aim for integration over overhaul, taking advantage of existing forensic

infrastructure while introducing only the essential portable support elements required to facilitate its mission. This approach minimizes disruption, reduces deployment complexity, and increases the system's viability for rapid field use.

Market Analysis

The market analysis for the Fire-Eye Unmanned Aerial System (UAS) targeted a niche yet critical sector(post-fire forensic investigation). With increasing urbanization and fire-related incidents, there is a growing demand for autonomous systems capable of entering structurally compromised environments to assist forensic teams. Currently, no UAS on the market is specifically built for post-fire evidence detection, which positions the Fire-Eye with an unmet need.

A detailed competitive analysis & market identification identified a significant gap in the forensic drone segment. Existing systems either focus on general mapping or surveillance and lack forensic-specific features such as UV fluorescence detection or minimal disturbance flight profiles. Therefore, the Fire-Eye's modular architecture distinguishes it from existing traditional solutions.

Lastly, the SWOT analysis highlighted Fire-Eye's strengths in innovation, adaptability, and mission specificity, while also noting the challenge of entering a market with limited awareness of forensic UAVs. Nonetheless, this presents a first-mover advantage in a sector expected to grow with rising demand for safer and smarter disaster response tools.

Payload Selection

Mapping

Mapping refers to the 3D reconstruction of interior spaces. Two primary technologies used for this purpose are photogrammetry and LiDAR. Whereas photogrammetry performs passive sensing, meaning it relies on an external light source to capture images, LiDAR performs active sensing, meaning it emits its own laser beams and measures how long they take to reflect off surfaces.

A trade-off was performed scoring two LiDAR options (mechanical and solid-state) and two photogrammetry options (stereo and monocular). These four technologies were scored based on the following criteria: depth precision, mass, resolution, field of view and light sensitivity. Solid state LiDAR emerged as the preferred technology, capable of producing high resolution maps while adding minimal weight to the system. The Voyant Helium solid-state LiDAR was selected for integration.

Forensics

The forensic payload subsystem is designed to detect burnt human remains using ultraviolet-induced fluorescence. Through a literature review, it was found that UV light at 365nm can induce fluorescence in burnt bones, though effectiveness varies with burn severity. Due to limited quantitative data, a target irradiance of $5W/m^2$ was conservatively selected based on other fluorescence applications.

Four UV LED options were evaluated based on irradiance, efficiency, and power consumption. The Seoul Viosys CUN66B1G was selected for its high efficiency and low power draw. Nine of these LEDs will be mounted on the drone and pulsed intermittently to reduce heat and energy use. They will be placed on metal-core PCBs for improved thermal performance.

To capture the resulting fluorescence, four camera options were assessed. The Arducam IMX462 NoIR was chosen due to its exceptional low-light sensitivity and auto-exposure capability, critical for identifying faint fluorescence in complex indoor scenes.

Together, the chosen UV LEDs and camera provide a compact, power-efficient solution to enhance forensic capability in fire-damaged environments.

Propulsion Subsystem

The propulsion subsystem was optimized through systematic analysis of configurations of combined propellers, airfoils and motors from a database constructed from commercially available components. The design process employed XROTOR simulations and a novel NPPS scoring metric to evaluate motor-propeller-airfoil combinations. Note that a non-tilted configuration was ultimately selected over a tilted design after careful analysis revealed its superior overall performance. While tilting the

rotors by 30° did provide a modest 13.5% reduction in downwash velocity, this marginal benefit came at the significant cost of a 20% decrease in system efficiency.

The final configuration, as can be seen in Table 1, combines a XING 2814 880 kV brushless motor with custom 10x4.5-inch propellers featuring Selig S1223 airfoils, achieving 11.7 N total thrust at 342 W (68.27% efficiency) for thrust-to-weight ratio of 2, while cruise operation at thrust-to-weight ratio of 1 delivers 5.3 N thrust at 140 W with improved 75.82% efficiency.

Table 1: Final Propulsion Subsystem Configuration

Component	Specification	Value	Unit	Notes
Airfoil	Model	Selig S1223	–	High-lift low-Re airfoil
Propeller	Model	MR Series 10x4.5	–	
	Number of blades	2	–	
	Diameter	25.4	cm	(10 in)
	Pitch	4.5	in	
Motor	Model	XING 2814	–	
	KV Rating	880	RPM/V	
	Max Thrust	1924	g	Manufacturer rating
	Power	342	W	At 80% throttle
	Mass	88.3	g	

Power Subsystem

The power subsystem was designed to meet Fire-Eye's demanding energy requirements while minimizing mass and ensuring reliable operation. After evaluating numerous battery configurations from a constructed database, the SMC HCL-HP 22.2V 7600mAh 150C LiPo was selected as the optimal solution (Table 2), providing 137.64 Wh of energy at a weight of 1065 g. This single battery approach simplifies the system while delivering sufficient power for both propulsion and payloads.

Table 2: Final Battery Specifications

Specification	Value
Type	LiPo 6S
Capacity [mAh]	7600
Voltage [V]	22.2
Energy Capacity [Wh]	137.64
C-rating [-]	150
Mass [g]	1065

Structures and Materials

The Fire-Eye system uses an 'X' configuration, which aims to balance performance with stability and control properties, due to the LiDAR mapping system the central hub was moved forwards. All other internal components were placed in the hub according to Figure 2, they were placed to ensure a low center of gravity close to the centroid of the hub.

The structural analysis of the Fire-Eye quadcopter involved the sizing of the propeller arms based on the maximum deliver by the propulsive system, determining the thickness of the skin according to mounting point of the propeller arms and load introduction, as well as sizing the landing gear based on a drop from 0.25 m height. It was determined that the propeller arms are a hollow circular cross section with an outer diameter of 2 cm and a thickness of 2 mm made out of 30% carbon fiber filled thermoplastic PEEK. The material of the hub skin is polycarbonate, with a thickness all around of 1 mm, except for the base plate which is 2 mm and acts as the load introduction to the landing gear. The

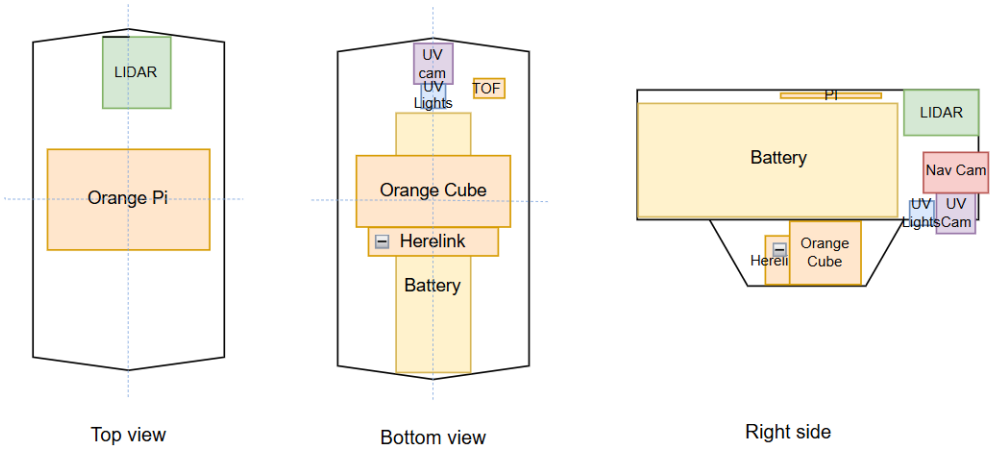

Figure 2: Packing arrangement of hardware within the hub

four strut, 13 cm long, landing gear, mounted at a 45 degree angle ensures a clearance of 5 cm to the ground, it is made of carbon fiber reinforced polymer to absorb the impact when dropped from 0.25 m height.

To ensure adequate cooling of vital internal components an elliptical cutout is made along the propeller arm, allowing air to be funneled through into the body of the drone. The 2.5 cm long and 1 cm wide cutout is placed at the location along the propeller arm where the induced velocity due to the propeller is largest. To avoid dust and debris ingestion the a mesh covers the cutout. Further structural analysis of the cutout is needed through FEA analysis or experimental tests. In addition to this the structure should be validated through experimental tests of simplified load cases to ensure the used design tools achieve an accurate result.

Navigation and Control

It is important to know if the system can be deemed stable, and if it is able to perform all the necessary maneuvers. The system employs both hardware and software to achieve this goal. The hardware that is used for flight control are the Inertial Measurement Units (IMUs), which measure the velocities and accelerations experienced by the system. Additionally, use is made of Time of Flight (ToF) laser systems that are able to detect objects up to 50 meters away. The ToF sensors are mostly used to determine the altitude of the system in addition to object avoidance.

In order to assess the controllability of the system, a custom controller was build using Matlab Simulink. The model was made to be a simpler version of programs such as ArduPilot, which are widely employed for the control of drones. The control model is a Proportional Integral and Derivative (PID) controller. This controller was chosen due to the wide range of applications and easy implementation.

Within the model three gains can be adjusted to achieve a desired response of the system. A desired response is one where given an input, there is no excessive overshoot or oscillations. This is crucial for any controller, but is of extra importance for the Fire-Eye system, as it has to operate in confined environments. Therefore little overshoot is desired. In addition, short system response times are disered to aid the operator in accurately maneuvering the quadcopter. The PID control block was tuned using a combination of the auto-tuning tool in MatLab SimuLink and manual tuning. The gains that are changed are the proportional gain (K_c), integral gain (K_i) and the derivative gain (K_d), with each gain for their respective control loop displayed in Table 3.

The Navigation and Control system was developed using a cascaded PID architecture, with validation confirming effective angular and altitude tracking under both isolated and simultaneous input conditions. Sensitivity analysis demonstrated that the controller tolerates moderate variations in mass but is susceptible to oscillatory behavior under reduced thrust coefficients due to saturation and voltage budget limitations. The absence of X and Y translational control was identified as a current

Table 3: PID Controller Gains and Derivative Filter Coefficients

Controller	P	I	D	N
Altitude (Z)	-3.049	-0.725	-3.009	450
Roll Rate	0.700	0.500	0.080	17.20
Pitch Rate	0.700	0.600	0.020	36.47
Yaw Rate	3.164	6.052	-0.067	17.20
Roll Angle	8.000	—	—	—
Pitch Angle	6.919	—	—	—
Yaw Angle	5.340	—	—	—

limitation, resulting in drift during pitch and roll maneuvers. Although angular tracking performance is promising, further controller tuning and integration of horizontal position loops are required to ensure safe operation in constrained environments, such as navigation through narrow openings.

Downwash

Since the disturbing of the scene should be avoided at all costs, it is critical to quantify the disturbance. This is done by analysing the downwash of the quadcopter at the ground when flying at a certain altitude. To quantify this disturbance, the induced axial velocity is analyzed.

The first two methods for doing this used one-dimensional momentum theory using the weight and thrust respectively to determine the velocity as an approximation.

The more extensive way to quantify the induced velocity is to make use of semi-empirical methods. The method employed in this report was taken directly from a paper by Khan [2]. Using this, an induced velocity heatmap is then generated, showing the axial velocity at all points in the flow. A heatmap for the system in hover is shown in Figure 3.

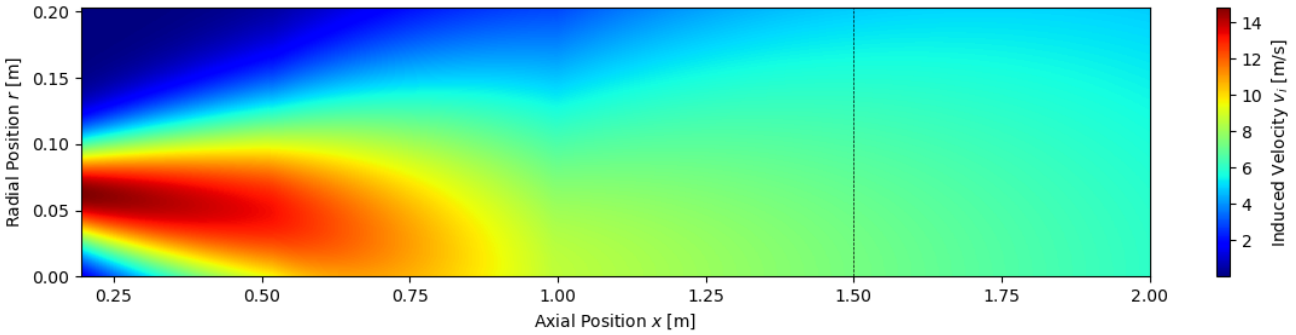

Figure 3: Induced velocity plot for hover

This plot includes a black line at a axial distance of 1.5 meters. This is the altitude at which the system operates. At this distance, the induced velocity should not exceed a value of 1.5 m/s. A plot showing the flow distribution at this location is shown in Figure 4.

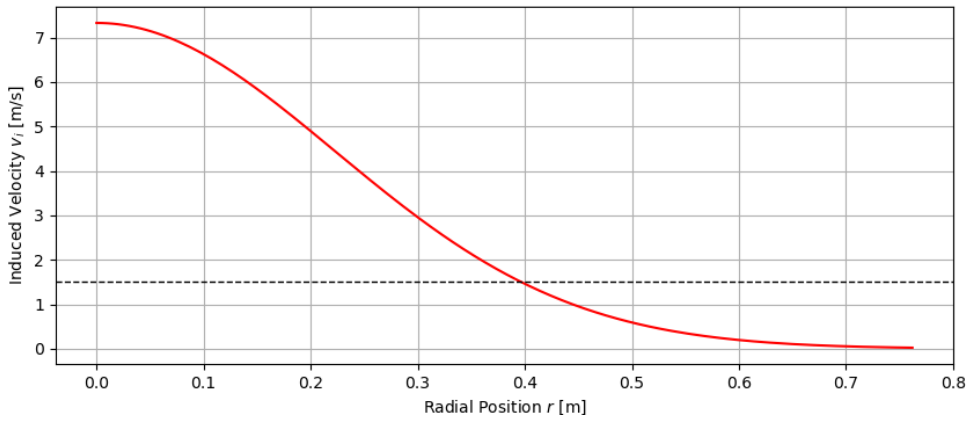

Figure 4: Induced velocity at the ground during hover

For comparison between the different methods employed, the maximum velocities for the three ways of calculating the induced velocity is shown in Table 4, for both the hover and maximum thrust case.

Table 4: Maximum velocities for all methods considered

	Hover	**Maximum Thrust**
Maximum velocity using thrust [m/s]	13.0	19.4
Maximum velocity using weight [m/s]	12.8	18.1
Maximum velocity using semi-empirical method [m/s]	14.9	22.2

However, it was found that the methods have a lot of limitations. For the first method, the calculation does not take into account the rate at which flow accelerates and decelerates. In addition, it is a calculation used for helicopters that is used for drones by taking the thrust of one propeller.

The semi-empirical method accounts for these limitations, but comes with notable limitations as well. These include not considering radial or tangential velocities, interactions between wakes of separate blades and rotors, as well as the consideration of outwash that occurs when the wake interacts with the ground. The latter of these was deemed insignificant given the flight altitude. Recommendations for improvements of this model include using experimentally gathered data as well as CFD for more accurate approximations.

The methods used were verified through unit testing as well as recreating the plots given in the original paper [2]. The validation was left for future design iterations due to a lack of experimental data on the downwash of similar propellers. Instead, a safety margin of 40% for the resulting induced velocity values was established.

Finally, further ways to potentially reduce downwash were suggested. These ideas proposed having structures underneath the propellers to disperse the flow. Most were deemed unfeasible due to the physics behind their workings, as well as the trade-off they provided between downwash reduction and efficiency reduction. Instead, it was proposed to either adjust the propeller sizing or reduce the weight of the quadcopter in operation, and hence the required thrust.

Performance Analysis

All design choices have been made, allowing for a final summary of each component. All components are presented below

The quadcopter its operations during flight have been grouped into three different phases. These are entry, mission and exit. The entry phase consists of take-off, approach, and navigation to the scene. The mission itself is divided into mapping and forensics. The recommended approach is mapping the entire building first, and then performing forensic research of the entire building afterwards. After finishing the mission phase, the Fire-Eye system exits the scene. Afterwards, these phases were analyzed, assuming that the entry and exit had a fixed flight time, and that thrust is constant during each mission phase. The mission phase performance metrics are calculated assuming peak performance, where the remaining battery is fully drained after the entry and exit phases had been fixed. All performance metrics are presented here in Table 10.2.

The entry phase duration is overestimated in terms of time, to account for any extra checks that might have to be performed during this phase. and has all components at work except for the mission payload. The motors provide constant thrust, which consumes nearly all of the power of this phase.

The mapping mission phase continuously consumes power. This consumption is much lower, because the motors are expected to provide less thrust, only providing enough to remain at a constant height during hover. The velocity of the quadcopter is 1m/s continuously, limited by motion blur of the navigation camera.

The forensic mission phase is the only phase where power consumption is not assumed to be constant. The UV LED array is powered in pulses. It flashes for 0.2 seconds every 2.2 seconds. Moreover, the forensic mission is done at a velocity of 0.5m/s, to avoid visible motion blur of the downward-facing camera.

The exit phase mirrors the entry phase, except it takes less time, since no checks have to be performed in flight. However, it is still likely an overestimation, which aids in accounting for unforeseen problems.

The performance metrics are presented in the table below:

Table 5: Power and energy consumption, phase duration, area coverage, and energy per unit area.

Phase	Power consumption (W)	Energy consumed (Wh)	Phase duration (min)	Total area covered per mission (m^2)	Energy per unit area (Wh/m^2)
Entry	1385.0	34.6	1.5	0.0	–
Mission: Mapping	534.4	111.0	12.5	1495.6	0.113
Mission: Forensics	502.4	111.0	13.3	445.5	0.379
Exit	1385.0	23.1	1.0	0.0	–

Verification has been performed on the charging time, the discharge rate. Moreover, validation has been performed to check whether the quadcopter could fully map the Grenfell Tower, and validates that this is possible in two working days and one hour.

Compliance Matrix

To illustrate which of the user requirements are met, a compliance matrix was generated. The full matrix and whether the requirement is met can be seen in Table 6.

Table 6: Requirements compliance matrix

ID	Requirement	Compliance
REQ-STK01	The system shall be able to fully map a typical apartment building of $500m^2$ within 1 week of operation.	✓
REQ-STK02	The system shall be able to create a 3D mapping of the scene with a resolution of 1 cm.	✓
REQ-STK03	The system shall be able to georeference the map with a resolution of 1 cm.	✓

Table 6: Requirements compliance matrix

ID	Requirement	Compliance
REQ-STK04	The system shall be able to geolocate detected human remains.	✓
REQ-STK05	The system shall be able to enter scenes through an opening of no larger than 70 x 70 cm.	✓
REQ-STK06	The system shall be able to employ UV fluorescence to detect human remains.	✓
REQ-STK07	The system shall comply with EASA requirements for safe operation of drones.	✓
REQ-STK08	The system shall comply with ILT requirements for safe operation of drones.	✓
REQ-STK10	The system shall not damage forensic evidence.	TBD
REQ-STK11	The system shall have an availability of 99% based on the Dutch climate.	TBD
REQ-STK12	The system shall be 75% by weight recyclable, excluding the payload.	X
REQ-STK13	The system shall have a unit purchase cost of no more than €50,000.	✓
REQ-STK14	The system shall be operable by a licensed 'certified' category UAS operator after 32 hours of training.	✓
REQ-STK15	The system shall be designed in 10 weeks time.	✓
REQ-STK16	The system shall be designed by 10 students.	✓
REQ-STK17	The system shall be manufacturable.	✓
REQ-STK18	The system shall be maintainable by a licensed technician.	✓
REQ-STK19	The system shall be able to operate beyond visual line of sight.	✓
REQ-STK21	The system shall be able to flag regions after localization of human remains.	✓
REQ-STK22	The project shall at all times adhere to the TU Delft code of conduct.	✓
REQ-STK23	The system shall be transportable to various locations in The Netherlands using existing fire department infrastructure.	✓
REQ-STK25	The system shall not cause harm or endanger the operating crew or bystanders.	✓
REQ-STK26	The system shall be operable in a temperature range of -5 to $50^{\circ}C$ for at least 60% of nominal operating time.	✓

RAMS analysis

The Reliability, Availability, Maintainability, and Safety analysis focuses on guaranteeing the system's operational effectiveness. Reliability referst to the likelihood that the system operates without failure over time. The Failure Rate (FR) is expressed as failures per unit of time to quantify this. The system's total failure rate is estimated using both bottom-up and top-down approaches. Both methods were applied allocating failure rates based on historical data and adjusted with coefficients for technological age, complexity, and role importance. The estimated total system failure rate is 1.5 failures per 1000 flight hours with the battery subsystem contributing the most due to its weight.

Availability indicates how often the quadcopter is operational. It is calculated usign the Mean Time Between Failures (MTBF) and Mean Time To Repair (MTTR). The estimated availability across all subsystems is 98.5%, where battery and propulsion subsystems have the lowest availability due to shorter MTBF's and higher MTTR's.

Maintainability assesses how easily and quickly the quadcopter can be returned to operational condition after a fault. It is measured in Maintenance Man Hours per Flight Hour (MMH/FH). Also,

preventive maintenance is categorized by frequency (high, medium, low) depending on component importance and failure likelihood. High-frequency tasks such as damage inspection, cleaning, and calibrating, occur before every flight, while medium tasks occur weekly, and low-frequency tasks, such as performing benchmark tests about once a month.

Safety analysis focuses on addressing potential risks and how they are mitigated. This is taken into consideration by developing several safety measures to mitigate various flight hazards. Fire-Eye's mission is unmanned, which notably reduces the risk to human life. Routine maintenance and redundancies minimize the risk of failure, which ensures that the quadcopter remains safe even if components fail.

Technical Risk Assessment

Throughout the life cycle of the system, failures may occur, and their likelihood and severity must be systematically assessed and managed. Risks were identified by analyzing each phase of the project, from manufacturing until end-of-life, and various subsystems involved in the mission. Each risk was assigned a probability and an impact score through a standardized procedure, and these scores were used to generate an initial risk map, to highlight the most critical risks.

For the most critical risks, mitigation strategies were developed to reduce their probability, and contingency plans were set out to minimize their impact. These measures ranged from changes in the design process to fallback protocols. After the implementation of these measures, the risks were objectively re-evaluated to ensure they were no longer critical. Almost every risk was lowered to a non-critical concern, with the exception of **TR-MIS-PROP-04**. This is the risk concerning excessive downwash causing damage to evidence. While attempts have been made to reduce this risk, it remains a concern and will be addressed in further design phases.

Sustainability Approach Strategy

Sustainability has been a constant presence throughout Fire-Eye's development, shaping both high-level design decisions and detailed subsystem trade-offs. Fire-Eye's sustainability strategy is structured around three core concepts: Environmental, Social and Economic Sustainability. Each was taken into account throughout the design process, but always with the understanding that sustainability measures should never compromise the system's ability to complete its mission. If different aspects of sustainability compromised each other, priority was always given to aspects tied to formal requirements. These include recyclability (**REQ-STK12**), ease of use (**REQ-STK14**), and unit cost (**REQ-STK13**).

The system was then evaluated on how well it meets its sustainability goals and requirements. For example, material recyclability was measured in detail across all structural components, revealing that while the system cannot fully meet the 75% recyclability requirement due to the battery's large mass share, significant efforts were made to maximize recoverability of other components. Similarly, energy efficiency, modular design, and ease of maintenance were emphasized to promote long-term sustainability and lifecycle performance.

Looking beyond the current design phase, a series of post-DSE actions were outlined to further improve the sustainability of the design. These include steps to reduce environmental impact, extend system lifespan, improve usability and increase recyclability. Implementing these steps will ensure that the realized Fire-Eye system balances technical innovation with long-term ecological and social responsibility.

Production Plan

The Production Plan outlines the structured workflow for manufacturing, assembling, and integrating the Fire-Eye system, divided into four key phases: material procurement, fabrication, assembly, and final quality assurance. The process begins with sourcing all raw materials, off-the-shelf components, and fabrication tools. Subsequently, structural components are manufactured using advanced techniques such as CNC machining, laser cutting, 3D printing, and hot plate welding. These components are then integrated during the assembly phase, where propulsion, structural, and payload systems are installed with precision. Finally, the system undergoes rigorous validation and calibration procedures.

Final Design

The final design of the quadcopter can be seen in Figure 5 below.

Figure 5: Drone final design.

Contents

Nomenclature

List of Abbreviations

Abbreviation	Definition
AIT	Assembly, Integration and Testing
BEC	Battery Eliminator Circuit
BMS	Battery Management System
CAP	Capacity
CBS	Cost Breakdown Structure
CF	Carbon Fiber
CFD	Computational Fluid Dynamics
CG	Center of Gravity
COM	Commissioning
CTRL	Control
CSI	Crime Scene Investigation
CUR	Current
DOT	Design Option Tree
DTH	Data Handling
EASA	European Union Aviation Safety Agency
EFF	Efficiency
EKF	Extended Kalman Filter
EOL	End-of-life
ESC	Electronic Speed Controller
FBD	Free Body Diagram
FEA	Finite Element Analysis
FRM	Frame Subsystem
GTOW	Gross Take-Off Weight
HMI	Human-Machine Interface
ILT	Human Environment and Transport Inspectorate (Inspectie Leefomgeving en Transport)
IMU	Inertial Measurement Unit
MAP	Mapping Subsystem
MAS	Mass
MAT	Materials Subsystem
MIS	Mission
MNT	Maintenance
MMOI	Mass Moment Of Inertia
MTOW	Maximum Take-Off Weight
NAV	Navigation Subsystem
NGO	Non-Governmental Organization
NPPS	Normalized Propeller Performance Score
PAY	Payload
PC	Polycarbonate
PEEK	Polyetheretherketone
PEEK CF30	30% carbon fiber filled PEEK
PID	Proportional–Integral–Derivative
PROP	Propulsion Subsystem
PP	Production Plan
PWM	Pulse Width Modulation
PWR	Power Subsystem
QC	Quality Control RC
Remote Control	
RDT	Requirements Discovery Tree
REQ	Requirement
RPM	Revolutions Per Minute
STK	Stakeholder
STR	Structure
SWOT	Strengths, Weaknesses, Opportunities, Threats
TEL	Telecommunications
THM	Thermal Conditions
TR	Technical Risk
UAS	Unmanned Aerial System
USR	User
UV	Ultraviolet
V&V	Verification and Validation
WBS	Work Breakdown Structure
WFD	Work Flow Diagram
ZFE	Zone of Flow Establishment
ZEF	Zone of Established Flow

List of Symbols

Symbol	Definition	Unit
α	Tilt angle	[°]
β	Neutral axis angle from x-axis	[°]
δ	Bending deflection	[mm]
Δx, Δy	Payload CG shift	[m]
ΔF_i	Additional thrust force at rotor i	[N]
ΔM_i	Additional moment at rotor i	[Nm]
ϵ	Blade pitch angle	[°]
η	Induced efficiency	[-]
$\overline{\eta_p}$	Average spanwise propeller efficiency	[-]
θ	Pitch angle	[°]
ν	Poisson's ratio	[-]
ρ	Air density	[kg/m^3]
σ	Normal stress	[MPa]
σ_{appl}	Applied stress	[MPa]
σ_{cr}	Critical buckling stress	[MPa]
σ_{ult}	Ultimate stress	[MPa]
σ_{yield}	Yield stress	[MPa]
σ_z	Axial stress due to asymmetric bending	[MPa]
τ	Shear stress	[MPa]
τ_{max}	Maximum shear stress	[MPa]
τ_{min}	Minimum shear stress	[MPa]
τ_{shear}	Shear tear-out stress	[MPa]
ϕ	Roll angle (rotation about X-axis)	[°]
ψ	Yaw angle (rotation about Z-axis)	[°]
A	Cross-sectional area	[m^2]
A_{prop}	Rotor disk area	[m^2]
A_y, A_z	Shear forces in y/z directions	[N]
b	Width of shear/cutout area	[mm]
C	Battery capacity	[mAh]
C_P	Power coefficient	[-]
C_T	Thrust coefficient	[-]
c	Chord length	[m]
d	Hole or bolt diameter	[mm]
d_0	Outer diameter of cross-section	[mm]
D	Propeller diameter	[m]
E	Young's modulus	[GPa]
E_{mat}	Elastic modulus of material	[GPa]
E_{pot}	Gravitational potential energy	[J]
E_{usable}	Usable battery energy	[Wh]
F	Thrust force per rotor	[N]
F_i	Thrust at rotor i	[N]
F_1 to F_4	Thrust force from motors 1–4	[N]
F_{max}	Peak impact force per strut	[N]
F_{vert}	Vertical thrust	[N]
F_T	Maximum thrust per rotor	[N]
g	Gravitational acceleration	[m/s^2]
G	Shear modulus	[GPa]
H	Height	[mm]
h	Drop height or arm vertical offset	[m], [mm]
I	Second moment of area	[m^4]
I_{xy}	Product moment of inertia	[kg·m^2]
J	Polar moment of inertia	[m^4]
k_b	Bending stiffness	[N/m]
L	Length or moment arm	[mm], [m]
L_{strut}	Strut length	[m]
l_h	Height of propeller above CG	[m]
l_r	Rotor arm length from center to motor	[m]
M	Moment or torque	[Nm]
M_i	Moment from rotor i	[Nm]
M_1 to M_4	Moments from motors 1–4	[Nm]
$\vec{M}$	Moment vector	[Nm]
m	Mass	[kg]
m_{motor}	Motor mass	[g]
m_{MTOW}	Max take-off weight mass	[kg]
n	Rotational speed or number of rotors	[-]
P	Power	[W]

Symbol	Definition	Unit
P_0	Airfoil resistance power	[W]
P_i	Induced power	[W]
P_m	Power for vertical movement	[W]
P_{hover}	Hover power consumption	[W]
P_{max}	Max battery power output	[W]
Q	First moment of area	[mm^2]
R	Propeller radius or evaluation radius	[m]
T	Thrust or torque	[N], [Nm]
T_{vert}	Vertical component of thrust	[N]
T/W	Thrust-to-weight ratio	[-]
t	Wall thickness	[mm]
t_{req}	Required thickness	[mm]
U_{bend}	Elastic energy in bending	[J]
V	Battery voltage	[V]
V_{up}	Vertical climb velocity	[m/s]
V_i	Induced velocity	[m/s]
V_2	Induced downwash velocity	[m/s]
W	Width	[mm]
W_b	Weight of drone body	[N]
W_p	Weight of payload	[N]
x, y, z	Cartesian coordinates	[m]

1 - Introduction

Large-scale building fires often leave behind dangerous, unstable structures that pose serious risks to forensic teams and emergency responders. These scenes can be structurally unstable, poorly lit, and contaminated with hazardous debris, making human entry both dangerous and inefficient. Investigation teams tasked with entering these dangerous scenes are faced not only with the challenge of navigating this unsafe environment, but also with identifying human remains that may be partially or severely burned. In response to this, the Fire-Eye project was initiated to address the mission need statement:

There is a need to conduct forensic investigations, map interiors, and locate human remains in confined and structurally compromised post-fire interiors, without human presence.

The objective of Fire-Eye is:

To develop a compact, unmanned system operating in fire-damaged structures, providing spatial mapping and detecting human remains using UV-fluorescence, while minimizing environmental disturbances, by 10 students in 10 weeks.

The result is the Fire-Eye system: a lightweight, modular quadcopter designed specifically for confined and hazardous post-fire environments.

Initial stages of the project, detailed in previous reports [1, 3, 4], focused on the operational context and defining the core system requirements. Stakeholders emphasized the need for a system that could enter damaged buildings through small openings, navigate through debris-filled environments, generate detailed interior maps, and detect human remains, specifically bones, through ultraviolet (UV) fluorescence imaging. The system must also comply with EASA regulations and remain affordable, reliable, and environmentally responsible. These functionalities will allow investigators to evaluate structural layouts, plan safe entry routes, and locate remains without compromising scene integrity or endangering personnel. Key constraints include minimizing disturbance to the scene, achieving high-resolution mapping, and ensuring compactness and maneuverability in cluttered indoor spaces.

Based on these requirements, five different unmanned aerial system configurations were proposed and explored in a previous design phase. These options ranged from simple quadcopters to more complex modular and tilted designs. The Modular Tilted Quadcopter emerged as the preferred concept after a structured trade-off analysis in the midterm report [4]. This was primarily due to its low downwash and promising performance in sustainability and safety metrics.

Building on the foundation laid out in earlier phases, this final report presents a more detailed design of the Fire-Eye system. It includes an in-depth look into subsystem design, performance analysis, requirement compliance and operational considerations. Ultimately, the aim is to demonstrate that the proposed system not only satisfies the original mission need statement, but does so in a way that is practical, sustainable and robust.

2 - Mission Definition

Before any technical specifications or subsystem design decisions can be made, the mission itself must be clearly defined. This includes understanding the end-user needs and outlining how the system will be deployed and operated in the field. A comprehensive mission definition ensures that the design is rooted in practical use cases and aligns with operational realities.

This chapter presents the operational and logistical framework within which the Fire-Eye system will function, detailing how it integrates into existing forensic and emergency response infrastructure. It also summarizes the functional analysis of the system, which systematically decomposed the mission into essential functions and information flows. Together, these components provided a structured foundation for the subsequent design, allowing clear traceability from high-level mission objectives down to specific subsystem requirements.

2.1. Operations and Logistics

An important consideration in the preliminary design of a system is its operational procedures and the logistics that support it. This helps to recognize which components can be integrated into existing infrastructure and where new capabilities must be developed to guarantee effective deployment. Figure 2.1 illustrates the operational and logistical concept for the Fire-Eye system. For clarity, the diagram includes only the names of the phases, which are defined as follows:

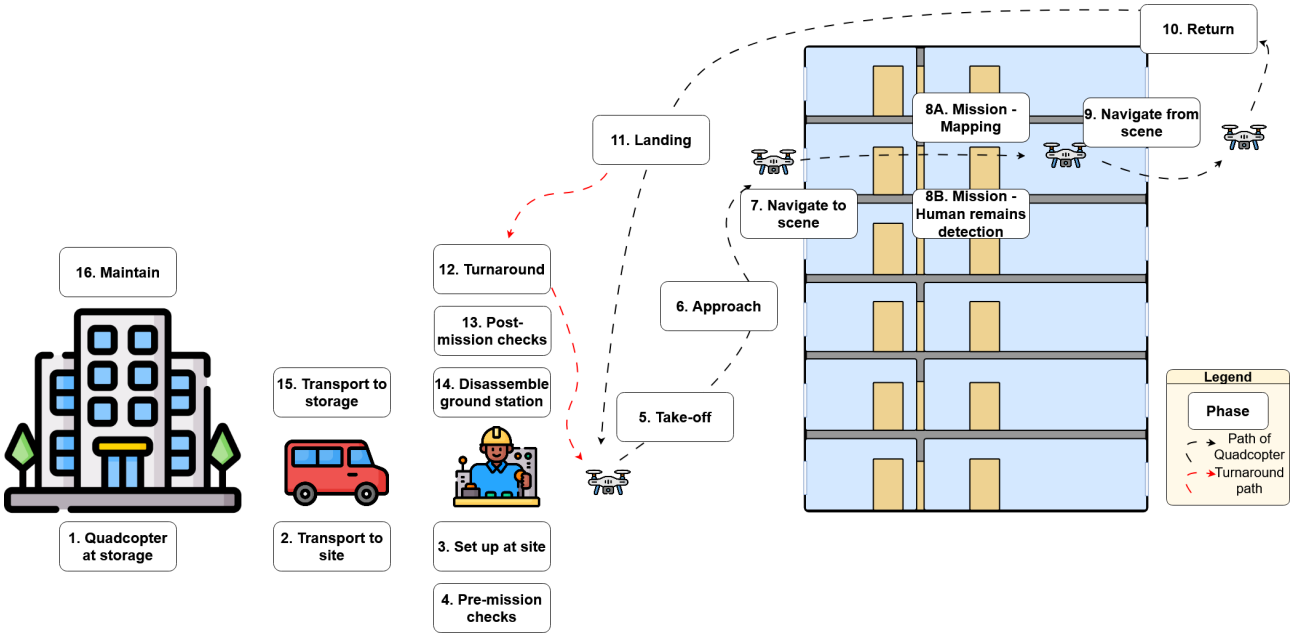

Figure 2.1: Operations and logistics concept diagram

1. Quadcopter at storage: During this phase, the quadcopter is kept in a mission-ready state. Certified technicians at the storage location perform regular checks on the system to ensure its functionality. The system integrates with existing forensic or emergency response storage facilities. Minimal new infrastructure is required, though secure and climate-controlled storage space with charging stations may need to be designated or upgraded.

2. Transport to site: The quadcopter, along with any operational equipment, is then transported to the mission site. No new logistics assets are required here, as the Fire-Eye system is designed to be lightweight and modular enough to be transported by existing forensic response vehicles.

3. Set up at site: A location near a tactical entry point is selected and checked for compliance with

airspace regulations. The ground crew then unpacks the quadcopter and sets up the ground station. The mission plan is finalized, and the operators are briefed. This setup process is designed to occur within existing operational zones such as mobile command posts or secured perimeters. However, a portable ground station is deployed on-site to support quadcopter operations.

4. Pre-mission checks: The operators perform the final system checks. All subsystems are confirmed to be operational before the operator makes the final Go/No-go call. This step fits into standard pre-deployment checklists followed by forensic or tactical teams. Checklists and software diagnostics tools will be new, but will not require infrastructure changes.

5. Take-off: If the mission is allowed to proceed, the operator instructs the quadcopter to take-off from the ground. The take-off zone will be within an existing secure area. No significant changes are needed, though teams may benefit from lightweight portable launch pads for optimal conditions.

6. Approach: The operator maneuvers the quadcopter to the target entry point of the building. The quadcopter flight path toward the entry point will be coordinated with current operational planning practices. No infrastructure modifications are necessary, beyond the inclusion of a system operator in the forensics team.

7. Navigate to scene: The operator maneuvers the quadcopter through the entry point and to the target scene. This phase makes use of current operational protocols used in building entry and scene analysis. No new infrastructure will be needed within the scene.

8A. Mission - Mapping: The operator activates the mapping payload and maneuvers the quadcopter through the scene. As this phase uses Fire-Eye's onboard payloads, existing infrastructure is not directly affected, though processing and visualization software will be required for integration into forensic analysis workflows. For both mission phases 8A and 8B, a fixed height has been set. In order to avoid downwash, the quadcopter should have a minimum height. This is determined to be 1.5m. If the quadcopter flies higher, it could come close to the ceiling, which could be as low as 2 meters in old buildings in the Netherlands [1]. This is expected to increase thrust and destabilize the system, likely to cause collision [5]. In buildings with higher ceilings, the quadcopter is allowed to go higher if the system is able to perform its mission as desired.

8B. Mission - Human remains detection: The operator activates the UV payload. The video feed from the quadcopter is watched closely by a member of the ground crew, and areas where there is fluorescence are flagged. This capability integrates with existing forensic procedures but requires new software to interpret UV fluorescence data and flag areas of interest.

9. Navigate from scene: The operator deactivates the mapping or UV payload. They then maneuver the quadcopter out through the target exit point of the building. If this proves impossible, the operator will attempt to land the drone in an area that is deemed non-critical. This step requires coordination with existing tactical teams but no additional physical infrastructure.

10. Return: The operator maneuvers the quadcopter towards the target landing zone. This occurs within the secure perimeter established by the operational team, and requires no additional infrastructure.

11. Landing: The operator lands the quadcopter in the target landing zone. As with take-off, optional portable landing pads may be used, but new infrastructure is not required.

12. Turnaround: The battery of the quadcopter is replaced and charged for future use by ground crew. The data collected during the mission is offloaded to the ground station. If the full mission has not been completed, ground crew prepares the quadcopter to continue and the modular payload is switched if the mission changes from mapping to human remains detection. This requires new mobile support tools, including portable charging units and data transfer stations, which can be integrated into the forensic team's current mobile equipment.

13. Post-mission checks: The ground crew inspects the quadcopter for any damage and offloads mission data to the ground station. If damage is found, this is noted for the maintenance team. These checks occur within existing logistical support routines, with only minor additions to inspection procedures and data handling protocols.

[1] URL: https://www.plameco.nl/blogs/welke-plafondhoogte-voor-welke-kamer, [Cited 02/06/2025]

14. Disassemble ground station: The ground crew packs up the quadcopter and disassembles the ground station. The mission is summarized and the ground crew is debriefed. Ground station disassembly and crew debriefing are a standard part of system teardown and require no new infrastructure.

15. Transport to storage: The quadcopter is taken back to the storage by the forensics team. As with deployment, existing forensic transport procedures are used.

16. Maintain: Certified technicians check the quadcopter for signs of damage and parts are repaired or replaced as needed. The quadcopter is taken back to the storage again, where it will be kept in a mission-ready state. The facilities where maintenance takes place may need additional diagnostic equipment and specialized repair tools tailored to Fire-Eye's design.

The modular architecture of the quadcopter allows the operator to mount specialized payloads for either mapping or forensic investigation. For each flight, the operator selects the appropriate payload based on the mission objectives. This selection determines whether step 8A (mapping) or 8B (human remains detection) is executed.

In summary, the Fire-Eye system is designed to integrate smoothly into current forensic and emergency response operations, minimizing the need for entirely new infrastructure. Most additions are limited to portable or modular components such as ground stations, payload-specific software, and minor upgrades to storage and maintenance facilities.

2.2. Functional Analysis

In support of the mission and system-level definition, a comprehensive functional analysis was carried out, as detailed in Appendix A. This analysis was described thoroughly in the Baseline Report [3], and it continues to serve as a foundational reference for understanding the Fire-Eye system's intended behavior throughout its full life cycle. The functional analysis began by identifying the key system segments—such as the Air Segment, Ground Segment, Communications, and Mission Operations—and mapping out how these components interact in the context of a forensic or emergency response mission. The mission architecture diagram (Figure A.1) illustrates these relationships, establishing the collaborative structure required to achieve mission objectives.

The system's functions were then sequenced using a Functional Flow Diagram (FFD), which represents the logical order and interdependence of operations from development and deployment to post-mission maintenance. This included all major phases such as pre-mission checks, mission execution, and post-mission procedures (see Figure A.2). The mission phase was broken into sub-phases such as take-off, operation, return, and landing, as seen in Figure A.3. This diagram helped define the system's required capabilities and informed the generation of system-level requirements. The corresponding Functional Breakdown Diagram (FBD), found in Figure A.4, provides a hierarchical decomposition of functions into intuitive packages, supporting traceability and hardware allocation across the system.

Together, the functional analysis diagrams ensure that the Fire-Eye design aligns with mission needs and stakeholder expectations. Although the detailed diagrams and logic remain largely unchanged from earlier phases of development, they continue to be relevant and are referenced here as the backbone of the mission concept.

3 - Market Analysis

Before developing any technology, it is crucial to ensure that it responds to real-world needs. Performing a Market Analysis surrounding Fire-Eye's mission allows the team to identify how the design can offer value to its stakeholders, giving reason for its development. The market analysis begins with a stakeholder analysis in Section 3.1, identifying key and non-key stakeholders involved. It then explores different segments of the target market to strengthen the value proposition in Section 3.2, followed by a competitive analysis in Section 3.3 to assess the current market landscape. The chapter concludes with a market identification summary in Section 3.4, and a strategic overview is presented through a SWOT analysis in Section 3.5.

3.1. Stakeholder Analysis

The first step in a market analysis is identifying all relevant stakeholders and understanding their importance. Stakeholders were classified into key and non-key groups, and evaluated based on when and how the product changes hands. Key stakeholders dictate major decisions of the design, whereas non-key stakeholders shape minor considerations. All relevant stakeholders are listed in the table below, with key stakeholders highlighted in bold.

Table 3.1: Overview of Stakeholders and their relevance

Stakeholder	Relevance
Clients	Define the user requirements and determine the desired features of the final product.
Operator	Responsible for operating the UAS; the system must therefore be user-friendly and intuitive.
Forensic Expert	Reviews visual data, potentially in real time, requiring high-resolution imaging and accurate mapping.
TU Delft	Leads the project and provides academic guidance and subject-matter expertise.
ILT & EASA	Set the legal and safety regulations for UAS operation at the national and European levels.
Manufacturers	Require detailed specifications to accurately produce the intended design.
Maintenance Crew	Depend on a modular and accessible design to ensure efficient repairs and system upkeep.
Fire Department	Deploys the system in hazardous environments to minimize risks to personnel.
Family of Victims	Expect the system to preserve dignity and assist in recovery to allow proper closure.
Law Enforcement	Oversees the crime scene and ensures legal compliance during operations.
Bystanders	Require that privacy and ethical considerations are upheld during UAS deployment.
Building Owner	May provide structural information aiding navigation and forensic analysis.

These stakeholders were then ranked based on their influence and interest in the project. Influence reflects how driving they are in constraining the final product, while interest reflects how leading they are when considering the design of the final product. These dimensions are visualized in the stakeholder analysis map in Figure 3.1.

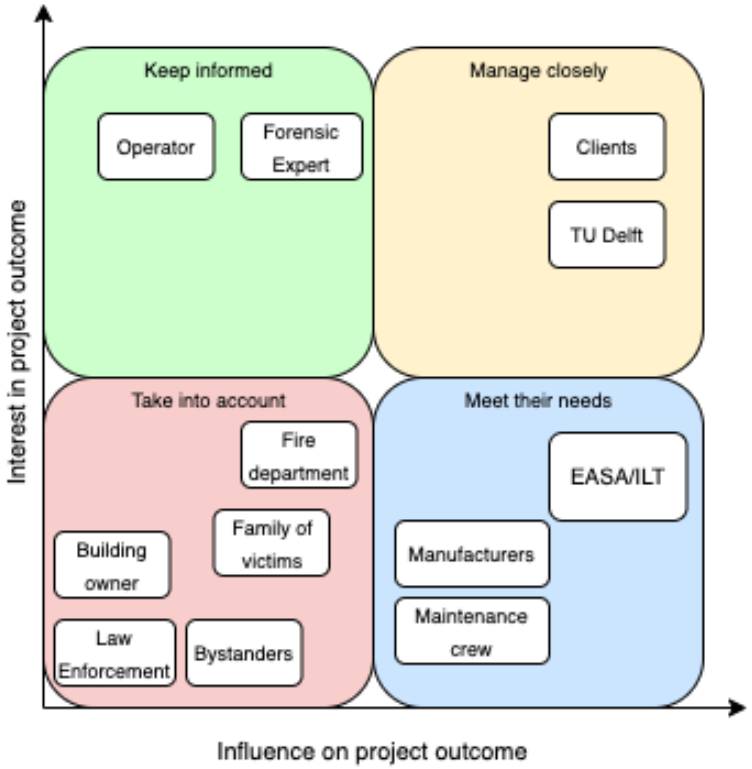

Figure 3.1: Stakeholder Analysis Map

3.2. Market Segmentation

Fire-Eye is primarily intended for organizations involved in post-fire investigations. Their interest may lie in forensic investigation, identifying casualties, and structural assessment of buildings. Within this target market, it is possible to identify different segments. Understanding these user groups supports requirement generation and strategic design choices.

This section outlines the principle market segments relevant to Fire-Eye, elaborating on their particular needs, constraints and the value Fire-Eye could offer to each. Relevant user groups were distinguished considering the following criteria:

- Mission profile
- Operational environment
- Geographic/regulatory context

Urban Fire Departments

Firefighter's responsibilities extend well beyond extinguishing flames. They are often required to recover human remains and assess scenes where fires have occurred to assess structural safety [6]. These activities commonly take place in hazardous sites where structural integrity has been compromised, implying serious risk to personnel.

Fire-Eye is well positioned to support these operations. Its compact design allows it to enter through small openings (70x70cm), making it ideal for entering collapsed buildings. Its visual mapping and UV fluorescence capabilities enable it to detect hazards and locate human remains, all with minimal disturbance to the scene. Designed to be intuitive, the UAS could be operated by firefighters with minimal training. Furthermore, its recyclable design and compliance with EASA safety standards align with the expectations and regulations that European departments usually must comply with.

Urban fire departments face increasing pressure to balance fast response with worker safety. Fire-Eye could offer a solution for worker safety by performing quick and reliable mapping of fire scenes, avoiding the need to enter the scene for assessment. However, the need for quick response implies

Fire-Eye should be designed for quick deployment. Another important consideration is the harsh environment following a fire. Dust and smoke may hinder visibility, making mapping less effective.

Fire-Eye's technologies offer clear value to fire departments by improving safety and efficiency in the tasks of casualty detection and scene mapping. In order to accomplish the function of assessing fire scenes, further development should consider increasing robustness in post-fire environment conditions and ensuring quick deployment. This would allow the UAS to be well adapted for emergency responses.

Forensic Institutes

Forensic institutes play an important role in post fire investigations, particularly involving fatalities. Their responsibilities may include locating and identifying human remains as well as determining the circumstances of death [7]. This process requires meticulous mapping and documentation while inflicting minimal disturbance upon the scene.

Fire-Eye directly responds to these needs. It enables the collection of accurate visual data (1cm accuracy) with minimal disturbance while navigating the scene. The need for human intervention is avoided, improving the preservation of the scene and providing the opportunity for the forensic search team to have a better plan about entering the building. Furthermore, its UV fluorescence feature facilitates the identification of human remains, as bones fluoresce under certain wavelengths [7].

However, participation in forensic investigations would require Fire-Eye to comply with strict legal regulations. In the Netherlands, as in many jurisdictions, forensic evidence must remain secure and unaltered throughout the forensic process. This includes "being able to demonstrate ownership at any given time" and "being able to demonstrate the integrity of the evidence" [8]. Hence, for this application, Fire-Eye should incorporate secure data transfer time-stamped data logging.

Overall, Fire-Eye represents a highly-specialized solution for the collection of data during forensic investigations. In order to comply with regulations in this segment, additional requirements surrounding data handling and security would have to be generated.

Disaster-Response Groups

Natural disasters such as wildfires or earthquakes can cause high numbers of casualties in a short time frame. In the aftermath of such an event, disaster-response systems in governments and NGOs can play a critical role by deploying resources to identify victims and assess damage. These operations typically span large areas with heavily damaged buildings.

Fire-Eye's compact design and flight capabilities make it a suitable technology for navigating burnt or partially collapsed buildings. It could access zones which are inaccessible for human responders, helping to identify victims and structural hazards. However, in events where buildings have collapsed into dense rubble, the UAS may face significant challenges gaining access.

A further constraint is operational scale. When responding to disasters, responders generally deal with large affected areas in urgent need (quick deployment). Fire-Eye's battery life limitations suggest it would need to recharge numerous times to scan large areas. Furthermore, the modular design option of the quadcopter might increase time needed if mapping the scene and conducting forensic research is needed.

Given the extreme urgency and scale of disaster operations, Fire-Eye's technical limitations may reduce its effectiveness as a main tool. However, it could still hold value in specific, high risk zones where precision and minimal disturbance are required.

Military

Military operations often take place in hazardous and structurally damaged buildings, particularly after explosions. These operations may include the assessment of structural damage and searching for casualties. In such hazardous environments, remote inspection technologies are needed to avoid putting personnel at risk.

With its compact design, flight abilities and high-resolution images, Fire-Eye offers value in such operations. Designed to withstand extreme post-fire environments, it should be capable of navigating

hot and dusty conditions after an explosion. Additionally, its low-disturbance design could be useful to avoid detection in missions which require stealth.

However, military operations present tough constraints. Missions may cover large areas, demanding high battery life and communication range. Quick deployment would be required to speed up operation. With increasing use of cyberattacks in conflicts, the UAS would require highly secure data handling and transmission. Furthermore, there is a risk of exposure to physical shocks and even hostile action.

Fire-Eye's current limitations surrounding battery life and communications could restrict its use in military operations. Nonetheless, having adapted the design to transmit data securely, the UAS could serve as a specialized tool to inspect post-blast environments.

Remarks

Market segmentation reveals a several promising applications for Fire-Eye, each with distinct operational needs and constraints. Fire departments, forensic institutes, disaster-response groups and military units all operate in high-risk environments where remote, minimally invasive investigation tools can provide significant value. However, each segment prioritizes different performance aspects. Forensic investigations are likely to prioritize scene preservation, whereas military operations demand secure communications.

There were requirements which emerged from the analysis that multiple segments would benefit from. Quick deployment of the UAS is essential for fire departments, disaster response and military use. Securing data is crucial in forensic and military domains. These requirements could be addressed with minor design adaptations such as foldable arms, hot-swappable batteries and data encryption software. Conversely, more ambitious improvements such as extended battery life or long-range communications emerged. These would greatly improve value for disaster-response and military use but may be limited by technical feasibility or cost. These findings are summarized below in Table 3.2 in the form of a qualitative cost-tradeoff.

Table 3.2: Cost Trade-off

Change	Impact	Cost	Affected Segments
Secure data encryption	Legal reliability; increased market trust, cyber-attack protection	Low (adapted software)	Forensic institutes, Military
Rapid deployment design	Easier setup; faster response time	Moderate (adapted hardware)	Fire departments, Disaster-response, Military
Extended battery life	Longer mission time, fewer interruptions	High (weight, size)	NGOs, Military units
Long-range communication (LTE/5G)	Increased operator-hazard distance, better control range	High (power, image quality)	Military units, Disaster-response

Market segmentation analysis identifies rapid UAS deployment and secure data handling as attainable design objectives that would significantly enhance Fire-Eye's value proposition in the market. To support rapid turnaround between missions, the adoption of swappable batteries provides a clear operational advantage. In parallel, the quadcopter's communication system, based on the Herelink platform, uses encrypted data links to ensure a basic level of security during real-time transmission. While these features are relatively modest from an engineering perspective, they offer substantial gains in operational relevance. Given the range and endurance limitations of the UAS, fire departments and forensic institutes emerge as the most promising target markets.

3.3. Competitive Analysis

The UAS sector is an emerging niche within the previously mentioned segments of the market. With current technological developments it poses a rapidly evolving industry, where precision, compliance, and operational efficiency are key differentiators. Understanding the landscape is essential to guarantee a long-term market position. This section provides a market analysis of current trends, existing solutions, and technological gaps, with their implied strategic entry points.

The application of quadcopters in forensic investigations is still in its infancy, with limited adoption and few operational systems currently in use. However, recent studies have begun to highlight the significant potential of UAS in transforming traditional forensic workflows. A comparison of UAS-based crime scene investigation (CSI) techniques to conventional methods, demonstrated that use of UASs could greatly enhance the effectiveness of crime scene investigation in terms of efficiency, evidence preservation, and scene documentation [9]. Furthermore, experimental studies have directly compared UAS performance to human teams in outdoor object detection scenarios [10]. Notably, in these investigations, UASs not only seemed to outperform humans in detection accuracy across various terrains, but also significantly reduced man-hours, making them especially valuable for large or complex scenes. These investigations show that UASs offer a cost-effective, scalable, and accurate alternative to conventional methods. Together, these findings establish a strong and growing market need for UAS-based forensic tools.

Mapping quadcopters are widely available and serve a broad range of industries. The increasing affordability, automation, and integration of advanced sensors have accelerated the adoption of these systems in both public and private sectors. These UAS's are able to generate precise 2D and 3D maps of environments in real time. Several drones have emerged to meet the demands of interior mapping and 3D modeling, despite the challenges of the complexity of the environment and the lack of GPS. For example, Flyability Elios 3 is a collision-tolerant drone built for inspections in confined and complex spaces such as tunnels [1]. Similarly, Skydio 3D Scan drones offer autonomous scanning capabilities for large, complex, indoor environments, like warehouses [11]. These drones present time and cost effective alternatives for 3D modelling of environments.

Despite this progress, the specific application of quadcopters for specifically post-fire interior mapping remains relatively underdeveloped. Human teams face a unique set of challenges when performing post-fire environment analysis of the interior of a building. Structural instability, poor visibility, heat damage, and the presence of debris all complicate this process. Although quadcopters are increasingly used in emergency response scenarios, their systematic use for the mapping of the interiors of fire-damaged buildings is still rare. However, recent research highlight the potential of the use of UAS in this niche. A technical report mentions the deployment of UAS to evaluate structural integrity after a major fire of an industrial hall with hazardous substances [12]. While the commercial application of quadcopters for post-fire interior mapping is still limited, this example illustrates the technical feasibility of the challenge. The emergence and improvement of indoor mapping technologies and a relatively untapped market domain, creates the opportunity for this innovative system to establish a new niche and take its position in a rapidly growing market.

The proposed quadcopter system offers a set of capabilities that position it competitively within a highly specialized and currently under-served market. One of the most significant differentiators is the inclusion of a UV fluorescence detection system. As previously mentioned drone-based forensics is a promising niche. However, few current commercial quadcopter drones offer direct solutions. The inclusion of the UV fluorescence detection system can aid the detection of human remains in post-fire forensic investigation. Therefore, the system addresses a specific need that is currently unmet by existing products.

Another competitive strength lies in the system's design emphasis on minimal scene disturbance. While there is a lot of development in noise reduction of conventional quadcopters, few focus on reducing the disturbance of the propulsion unit or, more specifically, preserving the integrity of a forensic scene. This makes the system most appropriate for sensitive applications.

One more competitive strength is the modular approach of the quadcopter's payload system. While integrating alternative payloads may require some modification and calibration, the system architecture is designed to accommodate such upgrades without fundamental redesign. For example, the current

[1] URL: https://www.flyability.com/elios-3-surveying-payload [Cited 2/05/2025]

forensic payload could be replaced with a photoionization detector (PID) for gas detection or a thermal imaging module for identifying residual heat sources. This expandability positions Fire-Eye as a flexible platform capable of evolving alongside emerging operational needs. In contrast to most commercial drones optimized for single-purpose use, Fire-Eye offers a future-proof design that can be adapted,with reasonable effort.

To enhance the product's competitiveness and operational flexibility, the final design implements a modular payload architecture in which the LiDAR mapping unit and the forensic UV fluorescence payload can be swapped depending on the mission. This approach offers several advantages. First, it allows for cost reduction in cases where only one of the two missions is required. Second, it lowers the total system weight during any single mission, enabling more compact configurations and supporting the requirement for minimal scene disturbance. Finally, it provides a clear upgrade path for users who may initially invest in only one payload type but require additional functionality in the future, thereby broadening the system's appeal across varied operational profiles and budgets.

3.4. Market Identification

The market analysis demonstrates a clear and growing demand for UASs with mapping and forensic capabilities. While several mapping drones are commercially available, Fire-Eye addresses a niche market with unique constraints such as confined access, scene preservation, and UV-based detection. Fire-Eye is particularly well-suited to serve urban fire departments and forensic institutes, offering competitive advantage such as UV fluorescence integration and the modularity of the system.

Although technical limitations like battery life and communication range may restrict large-scale applications such as military and disaster-wide deployment, Fire-Eye remains a valuable solution for high-risk operations that require highly sensitivity. The potential for modular payloads further increases its relevance and adaptability across multiple segments. Overall, Fire-Eye presents a compelling product concept in an untapped market that is starting to recognize the importance of the application of advanced UAS-based tools.

3.5. Mission SWOT Analysis

The SWOT provides a strategic overview for assessing a product's strengths, weaknesses, opportunities, and threats. This analysis helps to distinguish the product's position in the market and identify how competitive it will be. The strengths highlight key features that should be preserved or emphasized, while weaknesses identify areas that must be improved or re-designed. Weaknesses will likely lead to requirements as a minimum performance metric is needed. Opportunities point to external factors or trends that can be leveraged to enhance product value, which may translate into new features, demands or performance goals. Threats reveal external risks that the design must anticipate and mitigate. These are considerations that can have negative effects on the product's market position. The SWOT analysis for this project is presented below in Figure 3.2.

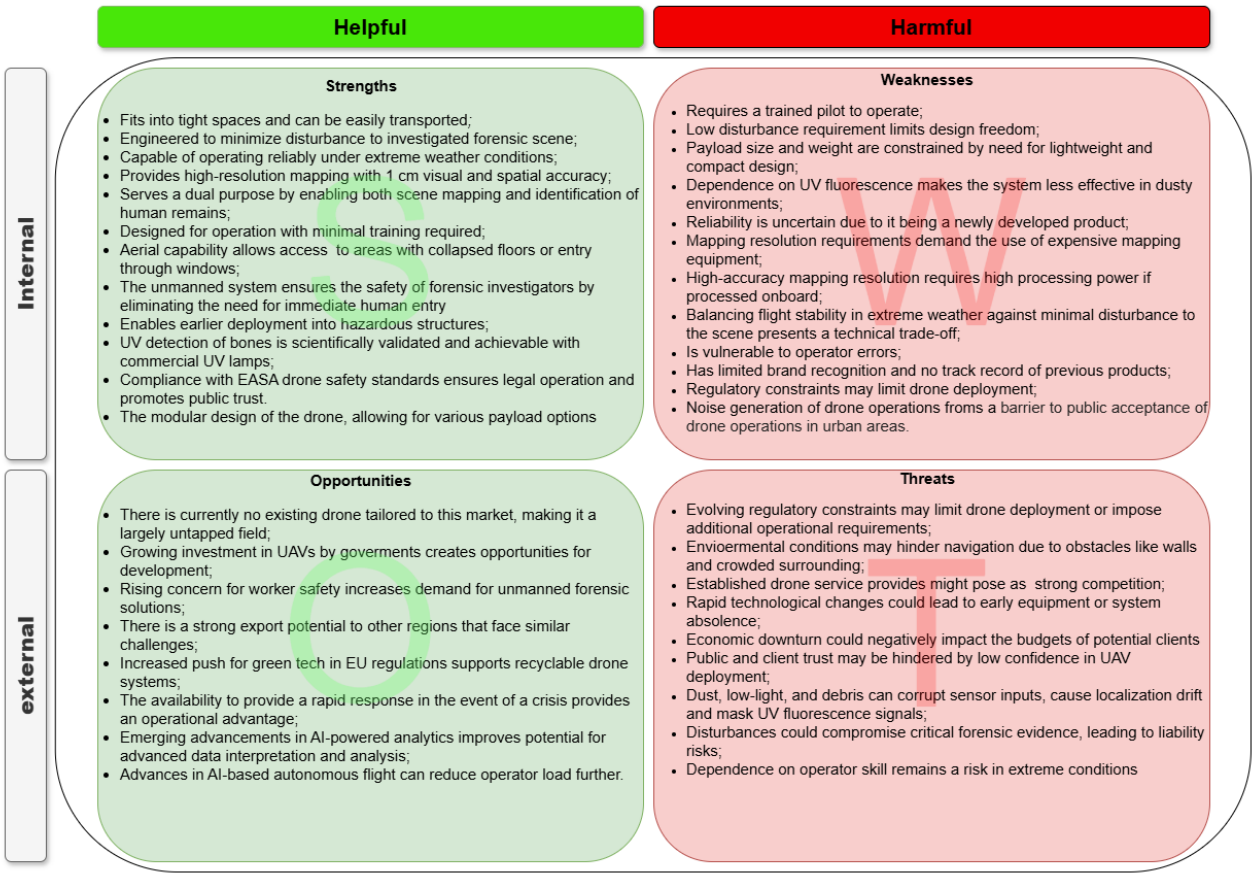

Figure 3.2: Technical SWOT analysis

4 - Payload Selection

Thus far, payload subsystems consisted of options. In the final design phase, specific components are selected as subsystems are refined. Selections are driven not only by individual performance requirements, but also by how each element integrates into the overall system.

First, Section 4.1 discusses the design of the mapping subsystem. Next, Section 4.2 explores payload options for forensic investigation. Section 4.3 describes the components needed for control navigation. The architecture used for communication is described in Section 4.4, and the power subsystem is described in Section 4.5. Section 4.6 presents an electrical block diagram which illustrated the interactions of subsystems. Finally, the weight and dimensions of payload components is summarized in Section 4.7.

4.1. Mapping

To select the technology used for the mapping system, a trade-off is performed. The design options are selected from the feasible options highlighted in the design option tree [4]. The selected options highlighted variations in the technologies that were deemed feasible.

Photogrammetry and LiDAR are two core technologies used for 3D scene reconstruction, each based on a different sensing principle, passive and active [13]. Photogrammetry is a passive sensing method, which means it depends on external light sources to capture images, like daylight or indoor lighting. It uses cameras to take multiple overlapping photos of a scene and reconstructs 3D geometry from them using certain algorithms and softwares. This can be done using a monocular camera, which captures images through a single lens [14], or using a stereo camera, which uses two lenses placed a fixed distance apart to calculate depth directly, similar to how human eyes perceive depth [15].

In contrast to photogrammetry, LiDAR (Light Detection and Ranging) is an active sensing technology, meaning it emits its own laser beams and measures how long they take to reflect off surfaces. This allows it to accurately measure distances independant of lighting conditions. One common type is mechanical LiDAR, which uses rotating mirrors to scan the environment, often with a 360° horizontal field of view. LiDAr has also more advanced types, such as FMCW (Frequency-Modulated Continuous Wave) LiDAR, which sends out a continuously varying laser signal and compares its frequency with the reflected signal. This approach allows it to measure both distance and the relative speed of objects, making it highly effective in dynamic or cluttered environments [16].

Five criteria were selected to evaluate the suitability of a selected technology in fulfilling the mission need. The criteria were selected based of factors which affect the success of the mission, such as the influence on downwash, as well as performance parameters of the system. The reasoning for the selection of each criteria, and the assigned weight is detailed below.

Depth precision: Depth precision describes how accurately the system can measure the distance to the surface being mapped. Higher depth precision produces more accurate 3D maps and better geolocation. As this criterion follows from **REQ-STK02**, it was most heavily weighted at 25%.

Mass: A heavier mapping system will result in an increase in the required thrust, likely resulting in an increase in the weight of the propulsion components. This result in a snowball effect, leading to a larger disturbance to the scene due to downwash. The minimization of mass being a design objective and the snowball effect result in a weight of 20%.

Resolution: The stakeholder requirement **REQ-STK02** details the required performance of the mapping system. Resolution for LiDAR refers to the spacing between mapping points when considering a 5x2 meter wall that is scanned in one second at 5m perpendicular distance. This wall is determined based on the minimum sports hall height in the Netherlands, which is 9m [1]. However, resolution for photogrammetry refers to the ground sampling distance at 5 meters. A higher resolution will result in a more accurate mapping, allows a decrease in movement through the scene, resulting in a smaller

[1] URL: https://nisav.nl/?page_id=1508, [Cited 04/06/2025]

disturbance. Moreover, the flying height could also increase, as long as the resolution complies with the requirement. As a result, the resolution criterion is weighed heavily at 25%.

Field Of View (FOV): The FOV of the mapping system dictates how much the system is able to see at once. A higher FOV is thus preferable as this result in the system being able to map more of the scene at once. However, for the same camera sensor a higher FOV results in a lower resolution, as resolution is preferred over FOV it was awarded a weight of 10%.

Light sensitivity: Light sensitivity refers to the systems ability to operate in low light conditions. As post fire environments often lack external power, it is likely that the level of light will be low. A mapping system that is able to operate in low light environments will decrease the need for on-board lighting systems, as well as a more versatile system thus giving it a weight of 20%.

In the trade-off, the design options are awarded scores ranging from 0% to 100%. Clear performance thresholds were established to award scores for each criterion, presented in Table 4.1. The Depth Precision performance thresholds were established by considering **REQ-STK02** and the performance of available technologies. The mapping subsystem's mass was estimated at 235g during preliminary design; to ensure that the design is converging to an improved performance, improvements upon this estimation translated into positive scores. Similarly, positive scores were awarded for technologies which provided superior resolution to **REQ-STK02**. A Field of View (FOV) exceeding 180° was considered excellent (100%) as it would enable the system to map environments without blind-spots while navigating. This reduces the need to rotate the sensor, streamlining operations. Finally, since manufacturers only describe photogrammetric light sensitivity qualitatively, qualitative performance thresholds were described. The scores here are correspondingly less extreme to reflect the more descriptive evaluation.

Table 4.1: Scoring criteria for sensor evaluation

Score [%]	Depth precision [cm]	Weight [g]	Resolution [cm]	FOV [deg]	Light sensitivity
0	$x > 10$	$x > 300$	$x > 1.75$	$x \leq 30$	~
25	$5 < x \leq 10$	$200 < x \leq 300$	$1.25 < x \leq 1.75$	$30 < x \leq 60$	Full daylight
50	$2.5 < x \leq 5$	$125 < x \leq 200$	$0.75 < x \leq 1.25$	$60 < x \leq 90$	Low light
75	$1 < x \leq 2.5$	$50 < x \leq 125$	$0.35 < x \leq 0.75$	$90 < x \leq 180$	Darkness
100	$x \leq 1$	$x \leq 50$	$x \leq 0.35$	$180 < x \leq 360$	~

Table 4.2: Completed mapping trade-off

Criteria / Option	Depth precision (25%)	Mass (20%)	Resolution (25%)	FOV (10%)	Light sensitivity (20%)	**Weighted Score**
Mechanical LiDAR	75	25	75	100	75	70
Solid State LiDAR	75	50	100	50	75	75
Stereo	25	75	75	75	25	50
Monocular	0	75	100	50	25	50

The trade-off results in Table 4.2 (weighted scores rounded to 5%) show that LiDAR based systems outperform the photogrammetry based system. The sensitivity analysis in which criteria weights are changed reinforced this finding as seen in Figure 4.1. There are two main criteria in which LiDAR outperforms the photogrammetry based systems, these are the depth precision and light sensitivity criteria. LiDAR systems are able to operate in complete darkness as they do not rely on external light, whereas the photogrammetry based systems do. The depth precision of LiDAR is consistently higher than photogrammetry systems as LiDAR directly measures the distance by computing the time of flight of the lasers whereas photogrammetry relies on image data.

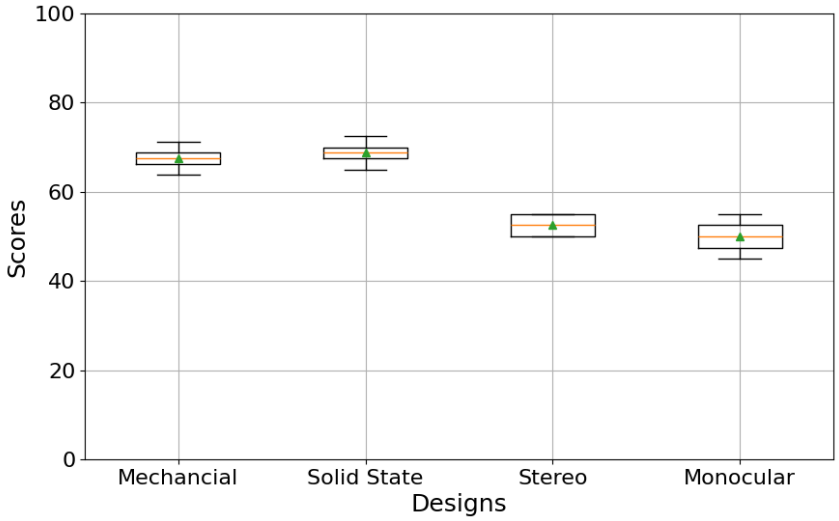

Figure 4.1: Sensitivity analysis of mapping trade-off in which the weight of each criterion was varied by ±5% and the sum of weights remained 100%.

Solid state LiDAR marginally outperforms mechanical LiDAR in the trade-off, and further reasoning reinforces it as the optimal technology. From a safety perspective, the solid-state lidar is preferred. Solid-state LiDAR does not have any moving parts, making it more reliable and less susceptible to failure [2]. Additionally, avoiding moving components benefits the flight stability of the system. Solid-state LiDAR also offers superior data rates, meaning it can map more quickly. Lastly the 360 degree FOV offers little benefit as the mounting position of the mapping system is front facing to ensure that the floor is also mapped. Due to the resolution of the LiDAR, the minimum height could be increased as opposed to 1.5m, preferably being at half the ceiling height to ensure resolution is similar everywhere.

This results in the solid state LiDAR technology being selected as the preferred system. The solid state system used in performing the trade-off in Table 4.2 is the Voyant Helium [3], which was found to deliver the best performance amongst compact solid-state LiDAR systems. Voyant shared the model's datasheet with the team. Some relevant characteristics are summarized in Table 4.3.

Table 4.3: Voyant Helium LiDAR Specifications [4]

Characteristic	**Value**
Dimensions (L×W×H)	42x28x44 mm
Weight	150 g
Field of View (H×V)	90° × 60°
Minimum / Maximum Range	0.1 m / 75 m
Range Precision	0.3-5cm
Points per Second	819 200 pts/s
Power Supply	M12 X-Code PoE
Power Consumption	27 W
Operating Temperature	0 to +50
Required Lighting	No light required.

[2]URL: https://globalgpssystems.com/lidar/explore-the-different-types-of-lidar-technology-from-mechanical-to-solid-state-lidar/ [Cited 04/06/2025]

[3]URL: https://voyantphotonics.com/products/ [Cited 04/062025]

4.2. Forensics

In this section, the trade-off for the forensics subsystem is presented. First, a literature study is carried out to investigate the optimal lighting to emit to cause fluorescence in burnt bones. Then, potential subsystem options are discussed. Finally, a trade-off is performed between several feasible options.

Literature Study

The identification of burnt human remains is a complicated and very niche research subject. The burn grade can differ significantly. Humans can often be recognized as a whole or in body parts, but in some cases even in ashes [5]. Two cases are hardest to recognize. These are fully carbonized remains and ashes. Differentiating carbonized remains from carbonized material such as wood is difficult. However, the analysis of ashes and highly burnt remains is a gap in the market. In recent years, alternate light sources (ALS) have been investigated because of their ability to cause fluorescence in biological evidence. Ultraviolet light, often emitted at 365nm, causes bones to fluoresce at 440nm [17], however, the elevated temperatures encountered in a fire scene significantly alter human remains. Fluorescence would likely still be apparent, although to a lesser extent [18]. It is completely indistinguishable when bones are carbonized, but it increases again if human remains were burnt with a higher temperature [19]. As described in the midterm report [4], there is no literature available from which a required irradiance is found. In other use cases[6], UV fluorescence begins to show significantly around $0.5W/m^2$. Thus, it was decided that a value of $5W/m^2$ was sufficient, as this is a large margin that should still be achievable for the drone. This allowed the trade-off to be performed. Furthermore, due to the limited literature available, a proper trade-off analysis could not be performed; therefore, various options were considered, and the best-performing one was selected.

Forensic Subsystem Requirements

From the literature review and requirements that were presented in the midterm report, the subsystem requirements for the forensic subsystem could be established. These are presented in the table below.

Table 4.4: Forensics subsystem requirements relevant to UV and camera selection.

ID	Requirement
REQ-STK06-MIS19-FOR01	The UV light shall provide an irradiance of $5W/m^2$ to the inspected area, at a height of 1.5m.
REQ-STK06-MIS19-FOR02	The UV light shall emit radiation with a wavelength between 300 and 400nm.
REQ-STK-MIS19-PAY01	The system shall be able to detect human remains within a square area equal to the quadcopter area plus a 5cm clearance to avoid collision.
REQ-STK04-FOR03	The camera shall be able to view the illuminated area.
REQ-STK04-FOR04	The camera shall have a resolution of $1cm^2$ per pixel.

UV Light Selection

Before selecting the UV light, various options must be investigated. It was decided that a wavelength between 300 and 400nm would be used [20].

With this in mind, the following LED options are considered:

- Nichia NVSU233C-D4 365nm[7]
- Nichia NVSU233C-D4 385nm[7]
- Seoul Viosys CUN6HB4A[8]

[5] Rob van Ekeren, police expert, interview on 12/06/2025

[6] URL: https://www.waveformlighting.com/tech/understanding-uv-irradiance-and-requirements-for-various-applications [Cited 04/06/2025]

[7] URL: https://led-ld.nichia.co.jp/en/product/led_product_data.html?type=NVSU233C-D4+%28365nm%29&kbn=1 [Cited 04/06/2025]

[8] URL: https://www.seoulviosys.com/en/product/detail/5 [Cited 04/06/2025]

- Seoul Viosys CUN66B1G[9]

Once LED options were identified, configurations could be designed. Assuming a height of 1.5m, taken from the requirement, the required number of LEDs to achieve the irradiance of 5W/m^2 on the ground was calculated. This was done based on the radiant flux and directivity of the options. Table 4.5 displays the result of this, along with relevant performance characteristics for each of the considered options.

The required angle for the drone to illuminate at least the area underneath itself, even in the corners of the drone to be able to cover corners, with a 5cm margin (so a radius of 56cm) was calculated to be $\approx 25°$. To ensure the minimum irradiance was reached at the edges, the efficiency at 25° of each of the LEDs was checked, and the irradiance at this distance was calculated. The required number of LEDs were updated if necessary.

Table 4.5: UV LED Performance Characteristics

LED Options	Nichia NVSU233C-D4 365nm	Nichia NVSU233C-D4 385nm	Seoul Viosys CUN6HB4A	Seoul Viosys CUN66B1G
Dimensions [mm]	3.5x3.5x2.73	3.5x3.5.2.73	6.8x6.8x3.75	3.5x3.5x2.83
Radiant flux [W]	1.450	1.730	5.300	2.000
Power usage [W]	5.39	5.18	15.6	3.7
Efficiency [%]	0.27	0.33	0.34	0.54
Directivity [°]	60	60	70	65
Radius of covered area [m]	0.75	0.75	1.1	0.91
Irradiance [W/m^2]	0.62	0.73	1.5	0.70
Irradiance at 25° [W/m^2]	0.52	0.62	1.4	0.55
Number of LEDs required [-]	10	9	4	9
Total power consumption [W]	53.9	46.6	62.4	33.3

Once the options meet the irradiance requirement, the most important factors to consider are power consumption and efficiency. Power use is critical, as an increase in power usage may lead to increased battery mass or reduced flight duration. Efficiency, defined as the radiant flux divided by the power consumed, is equally important as it is closely linked with the amount of heat the LEDs generate. Another factor to consider is mass, however, since most LEDs have a mass of less than 1g, their mass is negligible, especially when compared to the PCB the LEDs will be mounted on and the other components needed for the forensics subsystem.

Considering these two factors, it is clear that the Seoul Viosys CUN66B1G is the best option, offering both the lowest power consumption and the highest efficiency. Nine of these LEDs will be mounted near the center of the drone's body. As they will be placed close together, an effective thermal management strategy is needed. To limit the temperatures reached, as well as the power consumption, the UV LEDs will not be kept on continuously during the flight, but will instead flash periodically to illuminate the area. Furthermore, they will be mounted on metal core PCBs (MCPCBs), to provide efficient heat spreading and structural support [21].

Camera Selection

After deciding upon an LED system, a camera system is required to capture the fluorescence. As stated before, 365nm emitting lights result in fluorescence at 440nm. This is in the visible light spectrum, and since the chosen LED does not produce any visible light, no lens is required. Therefore, only a

[9]URL: https://www.seoulviosys.com/en/product/detail/2 [Cited 04/06/2025]

camera has to be decided on. This camera has a few requirements. It must have a resolution of 1 cm^2 and it should be able to capture at least the area requirement of the LEDs. Following from these, four cameras were considered. These are listed in Table 4.6

Table 4.6: Forensics Camera Performance Characteristics

	Raspberry Pi Camera module V3	**Arducam 12MP 477P**	**See3-CAM_CU135**	**Arducam IMX462 NoIR**
Power [W]	0.5	1	1	1
FOV [deg]	66H, 41V	75H, 60V	56H, 43V	141H, 82V
Frame Rate	2304x1296p56	2028x1080p50	1920x1080p60	1920x1080p60
Resolution [MP]	11.9	12	13	2
Low light functionality	Moderate, requires ISP	Moderate, requires ISP	Poor	0.001 Lux
Auto adjusting	PDAF	Manual	ISP on board	Manual

The task of this camera is to detect fluorescence, and both the setting and quadcopter attitude have an impact on the choice of camera. Since the height is constant, and the quadcopter flies in a building with varying lighting conditions, it is useful to choose a camera that could adjust for exposure, to discern fluorescence from debris in all conditions. Moreover, a camera that is more sensitive at low light will be better at discerning fluorescence, allowing for better results. That is why the Arducam IMX462 NoIR is chosen. It performs the best in low-light conditions of these four cameras, and with a built-in image sensor processor, it is able to adjust for the exposure.

4.3. Control and Navigation

Throughout the selection and development of all payload subsystems, a systems engineering approach was applied to ensure compatibility, simplicity, and integration readiness. A shared component selection framework was maintained in the form of a centralized spreadsheet, where proposed components were continuously documented and reviewed. This allowed for early identification of potential conflicts and ensured that all components would integrate smoothly within the overall system architecture. Such that decision was guided by both the performance of the component and the ease of integration within the system..

The navigation payload is designed to provide the pilot with sufficient sensory input for safe and stable manual control during flight. It consists of a downward-facing navigation camera, two Time-of-Flight (ToF) sensors, and the internal Inertial Measurement Units (IMUs) embedded in the Cube Orange+ flight controller. The camera enables real-time visual feedback to the operator, supporting manual maneuvering and situational awareness in complex indoor environments. As with the forensic camera, it must function reliably under variable lighting conditions, which justified the selection of the same low-light-capable model.

To support altitude awareness and obstacle proximity estimation, the system incorporates two ToF laser range sensors. These compact sensors provide continuous distance measurements and play a vital role in safe navigation through the expected confined spaces. Additionally, the IMUs within the Cube+ enable real-time attitude estimation, ensuring the quadcopter remains stable and responsive to control inputs. A more detailed discussion of these sensing components and their integration is discussed later in Section 8.1.

4.4. Communications

In the following section, the trade-off for the communications subsystem is introduced. It starts with the literature study to research various options for reliable connection. Afterwards, the options are discussed and the most feasible option is chosen.

Literature Study

Reliable and robust data links are essential in beyond visual line of sight (BVLOS) operations such as Fire-Eye. The performance of this subsystem largely depends on the effective isotropic radiated power

(EIRP), antenna configuration, and the frequency band in use. The command and control, telemetry, or payload data transfer ought to be broadcasted live to the ground operator with a maximum latency of 100 ms as stated by REQ-STK19-TEL02. Increasing this latency will result in poor controllability by the operator. EIRP directly influences the signal's strength and its ability to penetrate through obstacles such as concrete, rebar, and atmospheric interference.

EIRP is the amount of power that would have to be radiated by an antenna to produce the equivalent power density observed from the actual antenna. It allows comparisons between different transmitters regardless of type, size or form. From the EIRP and an antenna's gain, it is possible to calculate real power values. This is shown in Equation 4.1.

$$P_R = P_{EIRP} - \text{Path losses} + \text{Antenna Gain} \tag{4.1}$$

Where P_R is the received power and P_{EIRP} is the EIRP. In more mathematical form, the equation becomes.

$$P_R = \left(\frac{\lambda}{4\pi d}\right)^2 P_T G_T G_R \qquad \lambda = \frac{c}{f} \tag{4.2}$$

Where $c = 3 \cdot 10^{-8} m/s$ is the speed of propagation for electromagnetic waves, f is the transmission frequency in Hz, and λ is the wavelength in m. The product $P_T G_T$ is the EIRP and G_R is the antenna gain.

Furthermore, the path propagation loss L_P describes the loss associated with propagation of electromagnetic waves from the transmitter to the receiver which is given by Equation 4.3

$$L_P = (\frac{4\pi d}{\lambda})^2 \tag{4.3}$$

This loss dpeends on the carrier frequency and the distance between the transmitter and receiver. In conclusion, the most effective way to establish a robust data link capable of penetrating obstacles is to use a high transmitter power and a low transmission frequency.

Communication Subsystem Requirements

Table 4.7 presents the requirements followed from the literature study done on communications and telemetry.

Table 4.7: Communication subsystem requirements

ID	Requirement
REQ-STK19	The system shall be able to operate Beyond Visual Line Of Sight (BVLOS).
REQ-STK10-MIS18	The system shall be able to return to base in case of signal loss.
REQ-STK07-TEL01	The system shall use the AES encryption method.
REQ-STK19-TEL02	The system shall enable real-time viewing of the onboard sensors with a latency of 100 ms.
REQ-STK19-TEL03	The system shall enable real-time viewing of the data required for navigation with a minimum of 30 fps.
REQ-STK19-TEL04	The system shall remain in contact with the ground station within a range of at least 2000 meters.
REQ-STK19-TEL05	The system shall have multiple paths of communication to ensure redundancy of control inputs.

Comparison of data link technologies

After establishing the requirements, research was done on various data link technologies suitable for the mission of Fire-Eye. In Table 4.4 the best option is listed together with the other components in the communications flow diagram.

Cellular (4G/5G)

Cellular connectivity offers long-range capabilities making it suitable for BVLOS operations. It operates on licensed spectrum where cellular signals rely on the coverage of cell towers like the way mobile phones connect. The penetration efficiency depends on infrastructure availability and network load. The DJI Cellular Dongle Enhanced Transmission is a promising candidate capable of operating in long range. However, under optimal signal conditions, the minimum delay is approximately 200 ms which is not acceptable.

Wi-Fi (2.4GHz / 5.8 GHz)

Wifi-based quadcopters communication subsystems are common in consumer and small commercial drones. It operates typically at 100 mW for 2.4 GHz and 25 mW for 5.8 GHz in the EU due to strict regulations. Wi-Fi provides high data rates but suffer from limited range and poor penetration in BVLOS conditions. The 5.8 GHz band offers greater bandwidth but has even poorer obstacle penetration due to higher path loss. Regulatory limits on EIRP constrain the effectiveness in obstruces environments. However, in a meeting with expert from MAVLab and the Dutch Droneteam, exceptions can be made to get approval of utilizing EIRP values of 250 mW which is 150mW higher than the accepted standard.

Bluetooth

Bluetooth is rarely used for BVLOS quadcopter links since it offers EIRP values of <10 mW and results in short range and limited penetration. It is unsuitable for drone communication but may be useful for close distance data exchanges such as performing the pre flight checks.

RF Systems

Radio-Frequency systems like the sub-GHz bands are widely used in BVLOS operations and FPV drones. These frequencies offer strong penetration and lower path loss compared to 5.8 GHz bands. However, this results in bandwidth limitations and lower quality of video broadcasting. Also, constraints limit the EIRP to 10-25 mW depending on the region. The data link remains robust in BVLOS making them attractive for complex environments

Communications & Data Flow Block Diagram

The onboard system architecture of the quadcopter has been structured to support the two operational phases, i.e. the mapping phase and the forensic investigation phase. To efficiently represent both the communication structure and the associated data handling, a single combined block diagram in Figure 4.2 illustrates the communication of the system and its data handling. This diagram shows all hardware-level connections between components, while also illustrating the type and direction of data exchanged. The physical connections (e.g., UART, USB, HDMI, Ethernet) represent the communication flow, and the italic annotations indicate how data is transferred, processed, or stored throughout the system.

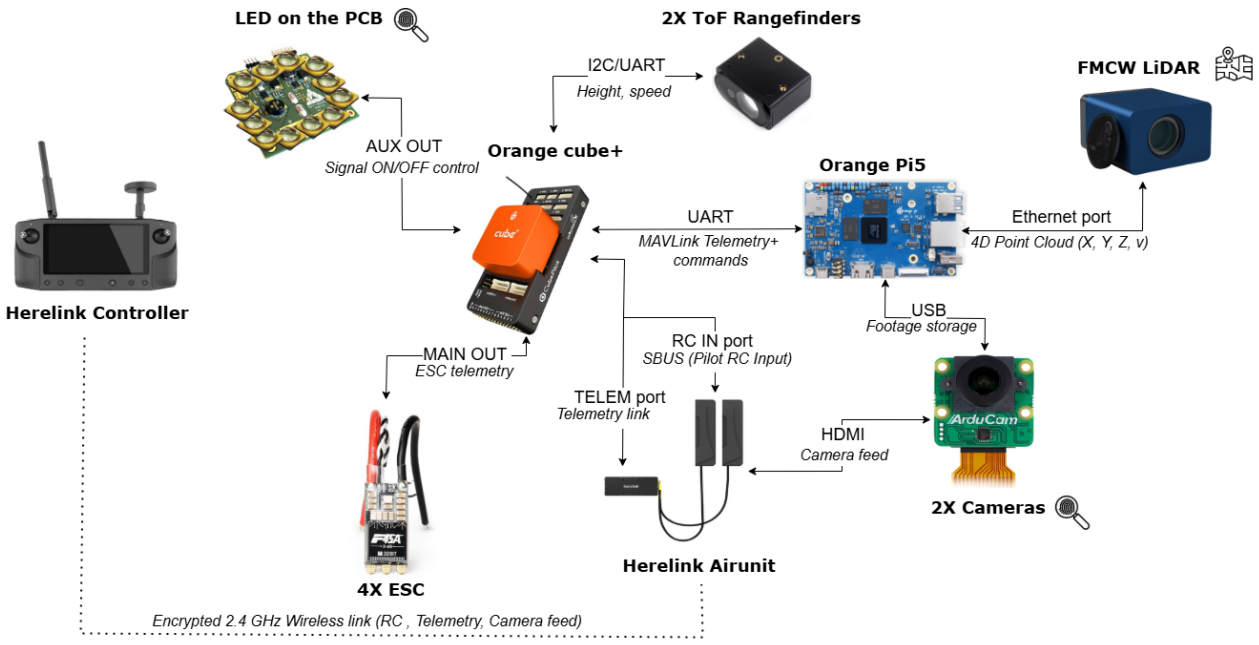

Figure 4.2: Communications flow diagram & data handling block diagram

At the core of the system is the Orange Cube+ flight controller [10], which serves as the real-time control unit for the quadcopter. The Cube+ is built on an STM32H7 dual-core processor and is responsible for sensor fusion, attitude estimation, control loop execution, and actuator control. It interfaces with onboard peripherals through UART, PWM, I2C, and GPIO protocols. Remote control commands from the pilot are received through the RC IN port using the SBUS protocol, transmitted by the Herelink Airunit. Motor control signals are sent to the four ESCs via the MAIN OUT ports using the DShot protocol, which also supports bidirectional telemetry. Telemetry data is further relayed to the Herelink system and the Orange Pi 5 companion computer through UART-based MAVLink interfaces. Additionally, the Cube+ issues digital ON/OFF signals to the LED system via its AUX OUT port. T flight controller jhas also a microSD card for onboard logging, and long-term data handling that is passed on to the Orange Pi 5 [11].

The Herelink system consists of a ground-based controller and an onboard Airunit, connected via an encrypted 2.4 GHz RF-system. This link simultaneously transmits remote control (RC) commands, telemetry data, and a live video stream, which is displayed on the ground controller interface. If regulations approve, the system is capable of operating with an Equivalent Isotropically Radiated Power (EIRP) of up to 250 mW, enabling reliable communication even in partially obstructed environments such as those expected in post-fire operational settings. Pilot inputs from the controller are transmitted wirelessly to the Airunit and then forwarded to the Cube+ via the SBUS protocol. SBUS is a digital RC protocol supported by Herelink that allows multiple control channels, such as throttle, pitch, and yaw to be transmitted over a single signal line. Simultaneously, the Cube+ transmits flight telemetry back to the ground controller through the Airunit and the Video from the onboard cameras is routed to the Herelink Airunit via HDMI and then wirelessly streamed to the controller, providing real-time situational awareness during flight operations.

The Orange Pi 5 serves as the onboard computational node and primary data storage platform. It is equipped with an RK3588S processor and high-speed data interfaces that enable efficient transfer of large data volumes to and from peripheral devices. In this configuration, it manages the storage of video data from the two USB-connected Arducam cameras and point cloud data from the Voyant Helium FMCW LiDAR sensor, received via Ethernet. Communication with the Cube+ is established through a dedicated UART link operating on the MAVLink protocol. Although the Orange Pi 5 is

[10] URL: https://ardupilot.org/copter/docs/common-thecubeorange-overview.html [Cited 16/06/25]

[11] URL: http://www.orangepi.org/html/hardWare/computerAndMicrocontrollers/details/Orange-Pi-5.html [Cited 16/06/25]

capable of real-time processing, the current system configuration is limited to data storage in order to optimize power efficiency. Real-time 3D reconstruction or onboard analytics are not implemented due to their high computational load and associated power demands. Nevertheless, the system architecture allows for future upgrades, including in-flight pre-processing or machine learning-based scene interpretation during forensic operations.

The Helium FMCW LiDAR sensor is employed exclusively during the mapping mission. It generates high-resolution 4D point cloud data consisting of spatial coordinates (X, Y, Z) and radial velocity for each measured point. The sensor outputs up to 819,200 points per second at 10 frames per second. The data is then transmitted to the Orange Pi 5 and stored locally for offline processing. The imaging subsystem comprises two Arducam 2MP IMX462 USB cameras. Both interface with the Orange Pi 5 via USB 3.0 for onboard storage. Additionally, the primary mapping camera connects via HDMI to the Herelink Air Unit to facilitate live video transmission to the ground controller.

The onboard LED array is integrated into a custom PCB and is employed only during forensic operations. It is powered via the power distribution unit and controlled by the Cube+ through a digital AUX OUT signal, which can be triggered manually by the pilot. Two Time-of-Flight (ToF) rangefinders are used to support situational awareness and flight stabilization. A vertically-mounted sensor provides continuous altitude measurements relative to the ground, while a horizontally-mounted sensor estimates forward velocity by measuring distance changes across the quadcopter's flight path. Both sensors connect to the Cube+ via either I2C or UART, and their data is used for height regulation and cruise speed estimation.

4.5. Power System

Power plays a central role in the architecture of the Fire-Eye quadcopter. With a large number of payload components—each with different voltage and current requirements—delivering stable and efficient power was essential. At the same time, the mission requires sufficient endurance, which introduced a key trade-off: increasing battery capacity improves flight time but adds significant weight, leading to greater thrust demand and overall power consumption. This created a design loop where payload mass, motor performance, and battery sizing had to be refined together through several iterations, as detailed in Chapter 6.

To better understand the demands on the power system, Table 4.8 below lists the voltage, current, and power consumption of the main components. This was then taken into account to determine the power budget needed per payload which then helped in choosing the battery and the propulsion system.

Table 4.8: Component power consumption

Component Name	Voltage [V]	Current [A]	Power [W]
Voyant Helium	24	1.12	27.00
Herelink 1.1	8	0.50	4.00
Seoul Viosys CUN66B1G (LEDs)	11.1	3.00	33.30
Ultra-compact ToF	4.3-5.2	0.02	0.10
Arducam Camera (1)	5	0.30	1.50
Arducam Camera (2)	5	0.30	1.50
Cube Orange+	4.1-5.7	1.00	5.00
Orange Pi 5	5	1.00	5.00
ToF for Cruise Speed	4.3 - 5.2	0.05	0.25

4.6. Electric Block Diagram

The electrical power architecture of the quadcopter is designed to support its modular dual-payload configuration while ensuring stable and efficient power delivery to all critical subsystems, particularly given the high power demands of the payload components. The electrical block diagram of the system is illustrated in Figure 4.3. Color-coded voltage lines (22.2V, 12V, 8V, and 5V) are used in the diagram to distinguish the regulated power rails and clarify the voltage routing throughout the system. The

modular structure of the layout highlights the separation between high-power, control-level, and mission-specific subsystems. Both payload configurations share the same power distribution board (PDB) and voltage regulation architecture, reducing redundancy.

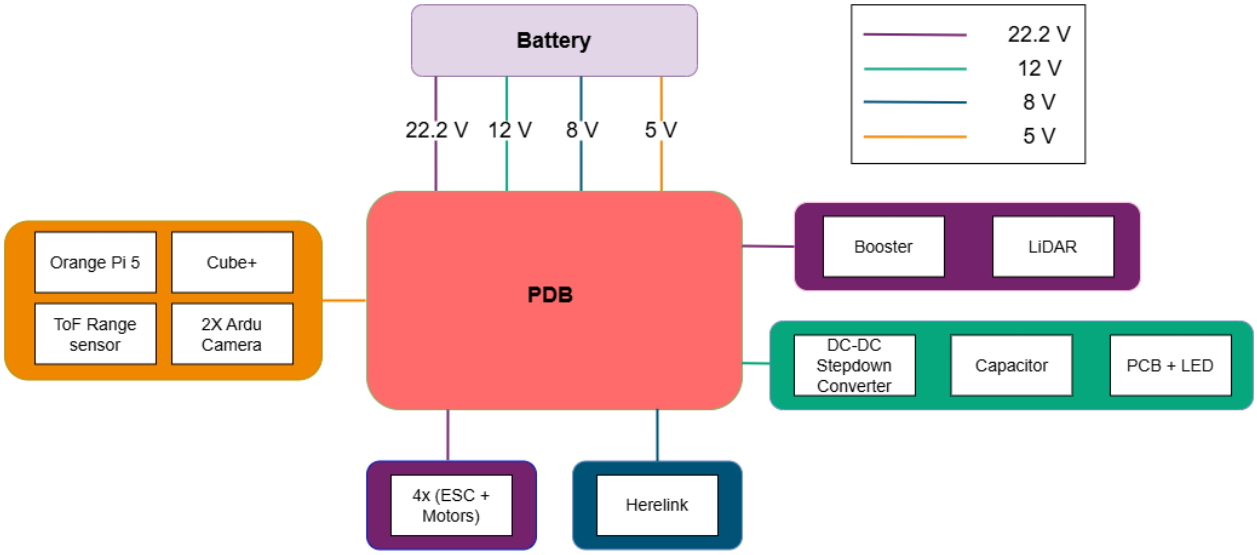

Figure 4.3: Electric block diagram of the quadcopter

The power system is built around a single lithium-polymer battery rated at 6S, 22.2V, 7600mAh, and 150C. A detailed justification for this selection is presented in Chapter 6. The battery connects directly to the Matek BEC12S-PRO PDB, which supplies both unregulated battery voltage and three regulated outputs via integrated Battery Eliminator Circuits (BECs). The onboard BECs provide 5V, 8V, and 12V, each rated for up to 5A continuous output, and are used to power subsystems with varying voltage requirements while maintaining electrical isolation.

Unregulated 22.2V from the battery is routed through the PDB to power high-current components, including the four T-Motor F45A ESCs, each driving a XING 2814-880KV brushless motor. These ESCs are rated for direct 6S input and therefore require no voltage regulation. The same unregulated line is also supplied to a DC-DC boost converter that steps the voltage up to 24V to meet the requirements of the Voyant Helium FMCW LiDAR, which consumes approximately 1.125A while active during the mapping phase.

The regulated BEC outputs serve mission and control electronics. The 8V output powers the Herelink Airunit, which handles wireless telemetry, video streaming, and remote control signals. The 5V BEC powers the Cube+ flight controller (approximately 1.0A), the Orange Pi 5 companion computer (1.0A), two Arducam IMX462 USB cameras [12] (0.32 A combined) and two Waveshare ToF laser range sensors (0.12A combined). This total load remains well within the 5A continuous current capacity of the 5V BEC.

To meet the power requirements of the Seoul Viosys CUN66B1G LED array, which operates only during the forensic mission, a dedicated voltage regulation path is employed. The 12V BEC output from the PDB is supplied to a DC-DC step-down converter, which reduces the voltage to 11.1V for the LED array. A capacitor is installed near the LED input to buffer inrush current and suppress voltage spikes during switching events, ensuring electrical stability across the system.

4.7. Hardware Weight and Dimension

In this section, an overview is given of the physical characteristics of the main onboard components that make up the quadcopter's hardware configuration. While system-level connections and functions

[12] URL: https://www.e-consystems.com/usb-cameras/sony-starvis-imx462-ultra-low-light-camera.asp [Cited 10/06/2025]

are already captured in Figure 4.2 and in Figure 4.3. Table 4.9 below presents the components in terms of their measured weight and dimensions and gives a more tangible sense of the hardware involved in the hub of the quadcopter.

The values were used to inform design decisions across multiple domains. In particular, they served as input for the iterative power sizing process described in Chapter 6, and helped guide the placement and integration of subsystems as discussed in Chapter 7 and served as input for the control and stability of the drone. The total weight of all listed components of the payload amounts to approximately 1893g, forming a substantial portion of the UAS takeoff weight.

Table 4.9: Filtered Component Weight Table

Component Name	**Dimensions [mm]**	**Measured Weight [g]**	**Quantity**	**Total Weight [g]**
Voyant Carbon	42x28x44	150.00	1	150.00
Herelink 1.1	78.5×30×15	68.00	1	68.00
LEDs	3.5x3.5x2.83	0.44	9	4.00
Ultra-compact ToF	19x12x10.3	1.00	1	1.00
SMC Racing HCL-HP 6S Battery	70x46x160	1065.00	1	1065.00
PCB	20.5x20.5x4	10.00	1	10.00
Camera (Low Light)	24x25x30	9.00	1	9.00
Orange Cube+	Carrier: 94.5x44.3x17.3 Cube: 38.4x38.4x22	73.00	1	73.00
Orange Pi 5	62x100	46.00	1	46.00
Motor XING 2814	36(d)*30	98.30	4	393.20
Blades	127	12.80	4	51.20
ToF for Cruise Speed	22.7x28x13.6	7.50	1	7.50
PDU BEC12S-PRO	35x24x5.5	5.00	1	5.00
T-Motor F45A ESC	30.5x30.5x3	10.00	1	10.00
Total				1892.90

5 - Propulsion Subsystem

The propulsion system is critical to the UAS's performance, directly impacting flight performance, endurance, and operational capabilities. This chapter details the selection and optimization process for the motors and propellers, beginning with a brief trade-off analysis between tilted and non-tilted configurations, followed by details the subsystem requirements in Section 5.1. The compilation of motor and propeller databases is detailed in Section 5.2. Key steps include airfoil selection using XFOIL analysis in Section 5.3, performance evaluation via XROTOR simulations, and the development of a scoring metric (NPPS) to rank configurations in Section 5.4. Section 5.5 delves into the specifications of the final design configuration for the propulsion subsystem.

Before delving into the design of the UAS subsystems, it is important to clarify that a non-tilted configuration was ultimately selected. While a tilted configuration was initially considered and discussed in the midterm report [4], results obtained in the preliminary analysis of the propulsion system's performance revealed that introducing tilt led to a decrease in efficiency, despite only a minor improvement in downwash characteristics. As shown in Table 5.1, the efficiency dropped from 0.10 to 0.08 when a 30° tilt was applied, while the downwash velocity at z=1.5 m decreased only slightly from 10.4 m/s to 9.0 m/s. Given that efficiency plays a more critical role in vehicle performance, it was determined that such marginal gain in downwash reduction did not justify the efficiency loss. Hence, the non-tilted configuration was opted for and carried forward throughout all subsequent design phases detailed in this report.

Table 5.1: Propulsion Preliminary Performance Results

Parameter	Non-Tilted	Tilted (30°)
Thrust per rotor [N]	9	8
Vertical Thrust Total [N]	37	32
Efficiency η	0.10	0.08
Thrust Coefficient C_T	0.55	0.48
Downwash Velocity at z = 1.5 m (v_z) [m/s]	10.4	9.00

Note that these values are based on the preliminary motor and propeller specifications defined in the midterm report [4], but the general performance trends are considered representative and valid for extrapolation in subsequent design evaluations.

5.1. Subsystem Requirements

This section specifies the propulsion subsystem requirements, which were derived from top-level mission and system requirements, ensuring compliance with the baseline design philosophy [3]. These requirements in Table 5.2 guide the propulsion configuration, motor and propeller selection, and performance verification, and ensure mission capability under normal and failure conditions.

Table 5.2: Propulsion subsystem requirements according to which the design was made.

ID	Requirement
REQ-STK01-MIS31-PROP07	The propulsion subsystem shall enable take-off and landing without external assistance.
REQ-STK01-MIS31-PROP04-EFF01	The propulsion subsystem shall provide a minimum thrust-to-weight ratio of 2.0.
REQ-STK01-MIS31-PROP05-EFF01	The propulsion subsystem shall maintain yaw torque balance during all phases of flight.
REQ-STK01-MIS31-PROP05-EFF02	The propulsion subsystem shall maintain an induced efficiency of at least 75% during cruise.
REQ-STK01-MIS31-PROP05-EFF03	The propulsion subsystem shall not exceed a tip Mach number of 0.3 during operation.
REQ-STK11-PROP01	The propulsion subsystem shall enable horizontal translation at 20 m/s outside of the scene.
REQ-STK02-PROP01	The propulsion subsystem shall enable horizontal translation at 1 m/s during mapping at the scene.
REQ-STK04-PROP01	The propulsion subsystem shall enable horizontal translation at 0.5 m/s during forensics at the scene.
REQ-STK10-PROP08	The system shall not produce more than 1.25 m/s downwash at the ground.
REQ-STK09-PROP07	The propulsion subsystem shall not displace debris more than 1.5 meters from its point of origin.

These requirements will guide testing and verification procedures to ensure that all propulsion related performance and safety criteria are met.

5.2. Motor and Propeller Database

The selection process for the propulsion system began with gathering a comprehensive motor database. Each motor included had to be able to provide a thrust of 2 times the quadcopter's weight. This thrust-to-weight ratio was chosen as an optimal compromise between maneuverability and flight endurance. A higher ratio would increase power consumption, reducing efficiency, while a lower ratio would limit the drone's ability to maintain stable flight in windy conditions[1], which would not have been in line with **REQ-STK11-MIS01**.

In parallel, a comprehensive database of commercially available propellers was compiled. This database included a wide range of propeller configurations, varying in diameter, pitch and number of blades. This database served as the foundation for evaluating multiple motor-propeller combinations during the propulsion design analysis.

5.3. Airfoil Selection and Processing

The first step in the design of the propellers was to research airfoils that could be used. The following airfoils were selected:

- NACA 0012[2]
- Eppler 216 (E216) low Reynolds number airfoil[3]
- Selig 1223 (S1223) high lift low Reynolds number airfoil[4]
- NACA 4412[5]

[1]URL: https://www.halfchrome.com/drone-thrust-testing/ [Cited 13/06/2025]
[2]URL: http://airfoiltools.com/airfoil/details?airfoil=n0012-il [Cited 13/06/2025]
[3]URL: http://airfoiltools.com/airfoil/details?airfoil=e216-il [Cited 13/06/2025]
[4] URL: http://airfoiltools.com/airfoil/details?airfoil=s1223-il [Cited 13/06/2025]
[5]URL: http://airfoiltools.com/airfoil/details?airfoil=naca4412-il [Cited 13/06/2025]

The NACA 0012 airfoil was selected due to its extensive historical use in rotor applications [22]. The E216 and S1223 airfoils were chosen for their favorable performance at low Reynolds numbers, making them well-suited for small-scale UAVs such as quadcopters[23]. The NACA 4412 airfoil was included because of its frequent use in UAV rotor designs and its demonstrated aerodynamic efficiency in propeller applications [24].

Once the airfoils were selected, their aerodynamic characteristics were evaluated using XFOIL[6]. Key properties such as lift and drag coefficients were computed across a range of angles of attack. From these results, the lift curve slope and drag polar were extracted and used in the subsequent performance analyses.

5.4. Propulsion iteration

To identify the optimal airfoil-propeller-motor configurations for the vertical lift system, an analysis pipeline was developed. An iteration over the different combinations was done using the tool XROTOR [7]. For each setup, both ducted and non-ducted configurations were evaluated.

In non-ducted configurations, propellers operate in open air and are typical in standard quadcopter designs due to their simplicity and lower weight. On the other hand, ducted configurations use a shroud around the propeller to reduce tip losses, improve thrust efficiency and enhance safety and noise reduction [25].

XROTOR was used to simulate both configurations across all motor–propeller–airfoil combinations, providing outputs such as thrust, torque, power consumption, and efficiency.

The objective was to select the top performing configurations that satisfy the vertical thrust requirement (Section 5.2) while minimizing power consumption and maximizing efficiency. The analysis also integrates geometric considerations such as spanwise distribution of blade elements and chord-to-radius ratios, ensuring physical viability.

From the performance parameters obtained in each simulation, a score was given to each combination named *Normalized Propeller Performance Score* (NPPS), computed as:

$$\text{NPPS} = 0.3 \cdot \frac{T_{\text{vert}}}{P} + 0.3 \cdot \eta + 0.2 \cdot C_T + 0.1 \cdot \overline{\eta_p} - 0.05 \cdot M_{\text{tip}} - 0.05 \cdot \frac{m_{\text{motor}}}{100} - \text{Penalties} \tag{5.1}$$

where T_{vert} is the vertical thrust, P is power consumption, η is the induced efficiency, C_T is the thrust coefficient, $\overline{\eta_p}$ is average spanwise propeller efficiency, M_{tip} is the tip Mach number and m_{motor} is motor mass (g).

Moreover, penalties are applied for insufficient blade elements (< 6), excessive inboard concentration of elements and low average chord ratio ($c/R < 0.02$).

The NPPS metric was constructed to quantitatively evaluate and rank propeller-motor-airfoil combinations by balancing aerodynamic efficiency, thrust performance, and practical design constraints. The term $\frac{T_{\text{vert}}}{P}$ is weighted heavily (30%) to favor configurations that generate the required vertical lift with minimal power, a very important criterion for endurance and battery sizing [26]. Induced efficiency η, also weighted at 30%, relates to the aerodynamic effectiveness of the rotor system and correlates with reduced energy losses due to inflow dynamics [27]. The thrust coefficient C_T is weighted at 20% to represent the rotor's loading characteristics, which influences induced power and rotor effectiveness [28]. The inclusion of spanwise propeller efficiency $\overline{\eta_p}$ (10%) captures how uniformly the blade elements contribute to thrust [26]. A negative weight is applied to tip Mach number to penalize compressibility losses and noise, and motor mass is also penalized to aim to minimize for mass.

The top configurations with the highest NPPS scores are retained and further assessed for power requirements compliance, further explanation on this process can be seen in Chapter 6.

[6]URL: https://web.mit.edu/drela/Public/web/xfoil/ [Cited 13/06/2025]
[7]URL: https://web.mit.edu/drela/Public/web/xrotor/ [Cited 16/06/2025]

5.5. Final Propulsion subsystem configuration

The final selected propulsion configuration consists of a custom designed 2 blade propeller, based on the commercially available MR Series - 10x4.5 Prop Set x2 Black [8]. While this commercial model served as a geometric baseline, modifications were introduced to the airfoil profile.

Note that the propeller set includes clockwise (CW) and counterclockwise (CCW) rotating units to ensure net-zero torque about the yaw axis, minimizing unwanted rotational effects during flight.

This propeller is coupled with a XING 2814 880 kV brushless motor [9]. The airfoil chosen for the blade design is the high-lift Selig S1223 [4]. The configuration remains non-ducted and non-tilted, based on earlier performance trade studies.

A summary of the final propulsion specifications is provided in Table 5.3.

Table 5.3: Final Propulsion Subsystem Configuration

Component	Specification	Value	Unit	Notes
Airfoil	Model	Selig S1223[4]	–	High-lift low-Re airfoil
Propeller	Model	MR Series 10x4.5[8]	–	
	Number of blades	2	–	
	Diameter	25.4	cm	(10 in)
	Pitch	4.5	in	
	Hub radius	3	cm	
Motor	Model	XING 2814[9]	–	
	KV Rating	880	RPM/V	
	Max Thrust	1924	g	Manufacturer rating
	No. of cells (LiPo)	3–6s	–	
	Max Voltage	16	V	
	Peak Current	50.9	A	
	Power	342	W	At 80% throttle
	Mass	88.3	g	

At 80% throttle, the propulsion system complies with the required thrust-to-weight ratio of 2, generating a total thrust of 11.7 N, compared to the 10.97 N minimum required. This corresponds to a power draw of 342,W and a rotational speed of 11867 RPM. The resulting thrust margin of approximately 6.6% accounts for payload modularity and introduces a beneficial performance buffer, ensuring system robustness across varying configurations.

In this operating condition, the overall system efficiency is 68.27%. The induced efficiency reaches 78.59%, indicating good aerodynamic performance, though some energy is lost to blade tip vortices and profile drag. The thrust coefficient is $C_t = 0.05848$; indicating a moderately loaded propeller, balancing thrust and efficiency. Whereas the power coefficient is $C_p = 0.03410$, indicating some energy is lost to drag at higher RPM. Both of which fall within expected ranges for efficient operation. The tip Mach number is 0.059, remaining below compressibility limits.

In contrast, for a thrust-to-weight ratio of 1, the system produces a total thrust of 5.30 N while drawing 140 W of power, with 7683 RPM. This yields an overall efficiency of 75.82%, an improvement over the higher thrust case, primarily due to reduced viscous losses. The thrust coefficient is $C_T = 0.06334$, slightly higher due to better aerodynamic efficiency at lower RPM, where induced drag is reduced. And the power coefficient is $C_P = 0.05137$, which seems high compared to the previous case due to RPM scaling, not true inefficiency, as validated with the induced efficiency of 85.83%. The tip Mach number remains at 0.059. These results indicate that operating at a lower thrust-to-weight ratio significantly improves energy efficiency.

[8] URL: https://www.masterairscrew.com/products/mr-10x4-5-propeller-set-x2-black [Cited 16/06/2025]
[9] URL: https://rcdrone.top/products/iflight-xing-x2814-fpv-motor [Cited 16/06/2025]

5.6. Verification and Validation

Verification and validation are essential parts of developing any engineering tool. Verification makes sure the tool is working as intended, while validation checks that its results actually make sense in the real world. By combining these steps, there is confidence that the propulsion design tool is reliable and useful for helping choose the right components for drone propulsion systems.

Verification

To ensure the accuracy and reliability of the propeller performance evaluation, unit testing was implemented for the processing script. These tests help verify the integrity of the parsing routines, the scoring logic, and the physical consistency of the data extracted from the simulation outputs.

Parsing Verification: Tests were developed to verify that the output parsing function correctly extracts key performance metrics from the text files generated by the propeller simulation tool. These include thrust, power, torque, efficiency, Mach number, and performance coefficients such as C_t and C_p. The parser was also tested for accurate extraction of blade element data across the span.

Filename Interpretation: Additional tests confirmed that filename-based metadata extraction was functioning correctly.

Scoring Function Validation: A dedicated test validated the accuracy of the scoring algorithm used to rank configurations. This included verifying how thrust-per-watt, efficiency, coefficient normalization, and tip Mach penalty were computed and combined to produce a single performance metric. The test used known input values with manually calculated expected scores to confirm correctness.

Physics-Based Expectations: Certain tests were included to validate physical relationships and that performance coefficients remain within expected bounds.

Required Thrust Accuracy: A test was added to validate the calculation of the required thrust per motor, based on total aircraft weight and thrust-to-weight ratio requirements.

Together, these unit tests build confidence in the robustness of the propeller post processing tool and ensure it can reliably support data-driven design decisions in the propulsion system selection process.

Running a coverage test using the python package `coverage.py` reveals a coverage of 89% of the file `post_processing.py`, Figure 5.1 shows the coverage percentage.

File	function	statements	missing	excluded	coverage
Aero_Prop/XROTOR_auto/post_processing.py	parse_output	28	3	0	89%
Aero_Prop/XROTOR_auto/post_processing.py	analyze_results	59	7	0	88%
Aero_Prop/XROTOR_auto/post_processing.py	*(no function)*	18	2	0	89%

Figure 5.1: Coverage percentage of verification tests for propeller propulsion analysis

Validation

The propulsion design tool primarily consisted of parsing, filtering, and selecting optimal combinations of components based on predefined performance criteria. The performance metrics utilized in this process were derived from XROTOR, a well-established aerodynamic and propulsion analysis tool that has undergone rigorous validation and benchmarking independently. This ensures that the theoretical performance predictions produced by the tool are reliable.

Furthermore, the inputs to the propulsion design tool were sourced from extensive databases of commercially available batteries and motors. This grounding in real world data ensures that the resulting component selections are not only theoretically sound but also practically feasible and accessible. The use of commercially available products reduces the risk of discrepancies between the modeled performance and what can be realistically achieved in practice.

To ensure that the thrust values predicted by the XROTOR tool are realistic, they are compared to those of a commercially available quadcopter with a similar size and mass. The Autel Robotics EVO II

was selected for this comparison, as it has a maximum takeoff weight (MTOW) of 2000g[10], which is close to our system's MTOW of 2237.9g.

Assuming a typical thrust-to-weight ratio (TWR) of 2—a common benchmark for stable flight and maneuverability[11]—the EVO II would require a total thrust output of approximately 4000g (or 39.2N), corresponding to about 9.8N per motor for a quadrotor configuration. In comparison, our system's per-motor thrust, as predicted by XROTOR, is 11.5N, which is reasonably close and well within the expected range for a similarly sized and configured drone. The increase is expected as Fire-Eyes mass is slightly larger than that of EVO II. This validates that the XROTOR output is consistent with real-world systems of comparable scale.

A proper comprehensive validation would involve physically assembling the drone with the selected components and conducting flight tests to assess actual performance metrics such as flight time, stability, and payload capacity. However, due to resource and scope constraints, this physical validation is deferred to future work. Some of these tests would include:

Static Thrust Test: Assemble the selected motor and propeller combination on a test stand equipped with a calibrated thrust gauge. Run the motor at various RPM settings and measure the static thrust produced. Compare these measurements with the predicted thrust values from the propulsion design tool to assess accuracy.

Battery Endurance Test: Fully charge the battery and power the motor-propeller setup at a constant throttle setting replicating typical flight conditions. Measure the actual runtime until the battery reaches its cutoff voltage. Compare this measured endurance against the tool's predicted flight time based on current draw and battery capacity.

Flight Test: Integrate the selected propulsion components onto a drone frame and conduct controlled flight tests. Monitor key performance indicators such as hover stability, maximum flight time, and payload capacity. Compare these results to the model predictions to evaluate real-world applicability.

[10]URL: https://shop.autelrobotics.com/collections/autel-evo-ii-series/products/evo-ii-pro-v3-rugged-bundle-1 [Cited 18/06/2025]

[11]URL: https://www.tytorobotics.com/blogs/articles/how-much-weight-can-a-drone-carry? [Cited 18/06/2025]

6 - Power Subsystem

With the propulsion and payload systems fully defined, the next step was to select an appropriate power subsystem. It was determined that Fire-Eye would operate using a battery-powered system to meet mission goals related to weight, endurance, and system simplicity. This chapter outlines the methodology used to identify and select the optimal battery configuration, balancing factors such as energy capacity, voltage compatibility and mass. The goal was to ensure reliable operation of all onboard systems, including propulsion and electronics, for the full mission duration.

Section 6.1 specifies the power subsystem requirements. Followed by Section 6.2, which describes the comprehensive battery database collected as the foundation for selection. Section 6.3 details the iterative process used to evaluate battery candidates against system power demands. Section 6.4 presents the final battery selection along with its key specifications.

6.1. Subsystem Requirements

This section specifies the power subsystem requirements, which were derived from top-level mission and system requirements, ensuring compliance with the baseline design philosophy [3]. These requirements, shown in Table 6.1, ensure mission capability under both nominal and off-nominal operating conditions.

Table 6.1: Power subsystem requirements according to which the design was made.

ID	Requirement
REQ-STK06-PWR01-CAP01	The power subsystem shall supply sufficient energy to sustain a 15 minute mission duration under full payload load.
REQ-STK06-PWR03-CUR01	The power subsystem shall be capable of delivering continuous current sufficient to support 80% throttle on all motors.
REQ-STK06-PWR03-MAS01	The total mass of the power subsystem shall not exceed 2000 g.
REQ-STK06-PWR01-THM01	The power subsystem shall maintain all components within their specified operating temperature limits during a standard mission.

6.2. Battery Database

To begin the power system selection process, a large database of batteries was gathered. This database included batteries suited for both high- and low-voltage applications, to allow for the possibility of using separate batteries to power the motors and the payload, optimizing each subsystem for performance and minimizing the power system mass.

6.3. Battery Iteration

Once the database had been gathered, an iterative process was used to find the optimal power solution. The energy, current and voltage requirements of both the propulsion system and the payloads were entered into the selection tool, which then evaluated each of the feasible battery combinations.

For the propulsion system, it was assumed that the quadcopter would operate at an average power draw of 50% over the mission. This assumption reflects a typical flight profile, where a mix of hovering, ascending, descending and maneuvering is expected to occur.

The payload energy requirements were made for a standard mission duration of 15 minutes, during which all payloads are assumed to be continuously active, for a conservative approach.

For each viable battery configuration, the power system mass was calculated. The five configurations

with the lowest mass were returned for further evaluation, balancing power delivery with the strict mass constraints critical to Fire-Eye's performance.

Once the mass of the selected power system was known, the thrust requirements could be recalculated for the new total mass. This, in turn, affected the power demands of the propulsion system, which could alter the optimal battery configuration. The updated requirements were re-entered into the selection tool and a new configuration was chosen. This process was repeated until the solution converged on the final battery.

6.4. Final Battery Selection

The final battery selected was a single SMC HCL-HP 22.2V 7600mAh 150C[1]. The specifications of this battery can be seen in Table 6.2.

Table 6.2: Final Battery Specifications

Specification	Value
Type	LiPo 6S
Capacity [mAh]	7600
Voltage [V]	22.2
Energy Capacity [Wh]	137.64
C-rating [-]	150
Mass [g]	1065

With this battery, FireEye can achieve a flight time of 15 minutes. The total system mass is 2237.9g when mapping, and 2087.9g when the forensic payload is all that is needed.

6.5. Verification and Validation

An important step in the battery selection process was to verify and validate all of the tools used. This guarantees that the best possible configuration out of those considered is selected.

Verification

To verify the correctness of the battery selection process, unit tests were carried out on each of the functions in the selection script. These tests were designed to check that the computations and selection logic function as intended. Key aspects of the verification included:

Battery Capability Verification: Tests were implemented to confirm that the maximum current output of each battery was correctly calculated from their capacity and C-rating, guaranteeing that the right combinations of motor and battery would be selected.

Accuracy of Energy Metrics: Further tests verified that energy capacity and density were present and accurate for each battery.

Battery-Motor Compatibility: The selection logic was tested to ensure it would not match batteries with motors they cannot power. This was based on performance criteria such as energy capacity and voltage. The tests also verified that both single and combined battery configurations were considered where possible.

Output Structure: Finally, the results that the tool outputs were verified to follow a consistent format, allowing for ease of selection of the highest performing battery.

Together, these tests provided confidence that the selection tool performs reliably under various input conditions and requirements.

Running a coverage test using the python package `coverage.py` reveals a coverage of 98% of the file `battery.py`, Figure 6.1 shows the coverage percentage.

[1]URL: https://www.smc-racing.com/index.php?route=product/product&product_id=679 [Cited 13/06/2025]

File	function	statements	missing	excluded	coverage
Aero_Prop/battery.py	process_batteries	3	0	0	100%
Aero_Prop/battery.py	preprocess_motors	3	1	0	67%
Aero_Prop/battery.py	get_max_current	4	0	0	100%
Aero_Prop/battery.py	get_batteries_motor	43	0	0	100%

Figure 6.1: Coverage percentage of verification tests for power subsystem analysis

Validation

To validate the choice of battery, the power system of a commercially available drone with a similar power consumption per flight is investigated. Fire-Eye's power system will be evaluated against that of the DJI Matrice 30 series[2]. Relevant battery characteristics are shown in Table 6.3 for both power systems.

Table 6.3: Battery Choice Validation

Specification	Fire-Eye Battery	DJI Matrice 30 Battery (TB30)[2]
Type	LiPo 6S	LiPo 6S
Capacity [mAh]	7600	5880
Energy Capacity [Wh]	137.6	131.6
Mass [g]	1065	685

As can be seen, both systems use a LiPo 6S battery. The DJI battery has a lower capacity. This is expected, as the Fire-Eye system hs an unusually high power draw thanks to its unique payload configuration. Moreover, the battery mass of the DJI system is significantly lower. This is due in part to the lower capacity, but also to DJI's advanced battery technology. When researching for the battery database described in Section 6.2, it was found that while the DJI batteries show excellent performance characteristics, they have strict compatibility requirements and work best with exclusively DJI components[3]. For this reason, they could not be considered. Aside from this, both power systems show similar characteristics, confirming that Fire-Eye's battery is a realistic decision.

However, due to the complexity of the power system and the large number of interdependent factors, it is not practical to validate the battery selection through theoretical modelling alone. The power system performance depends heavily on the combination of motors, propellers and payload power consumption, and no commercially available quadcopters align with the specifics of Fire-Eye's design. The system has a uniquely high power draw for its mass, and the propeller design has to factor in the size and downwash constraints of the system.

Instead, the most reliable method of validation will be empirical testing. Prototypes of the system will be fully assembled, and extensive ground and flight tests will be conducted to guarantee the actual performance of the quadcopter in realistic operating conditions. Tests will include:

Endurance testing: This will confirm that the power system can support the required mission duration of 15 minutes (**REQ-STK01-MIS37**).

Thrust and power measurements: This will assess the motor and propeller's performance when powered by the selected battery.

Thermal monitoring: This will ensure the battery remains within safe operating temperatures when supporting the full functionality of the payloads and propulsion system.

Redundancy and failure testing: This will evaluate the system's ability to perform in suboptimal conditions, and ensure that the appropriate measures can be taken in the event of failure.

[2]URL: https://shop.autelrobotics.com/collections/autel-evo-ii-series/products/evo-ii-pro-v3-rugged-bundle-1 [Cited 18/06/2025]

[3]URL:https://support.dji.com/help/content?customId=en-us03400006882&spaceId=34&re=US&lang=en [Cited 16/06/2025]

Payload operation tests: These will verify that the battery can provide consistent power to the payloads and other subsystems.

Rather than rely on theoretical predictions, this validation strategy accepts that the only way to know the system works is to build it, test it, and iterate. This approach ensures any unexpected behavior is caught early and addressed through design adjustments grounded in real-world performance. Time will be allocated in the post-DSE planning to account for the potential design iterations that will be required.

7 - Structures and Materials

This chapter describes the structural design and material choices for the Fire-Eye system. To maximize flight endurance and protect delicate subsystems of the quadcopter, the structures were designed to be lightweight yet robust. Furthermore, factors such as modularity and temperature resistance are also considered in the structural design.

Section 7.1 details the subsystem requirements that informed the structural design and material choice. Section 7.2 explores the frame configuration, which serves as the backbone of the system. Next, Section 7.3 analyses the propeller arms and Section 7.4 describes the landing gear design. Section 7.5, which discusses the central hub of the quadcopter, is subdivided into the design of the skin, modular payload mount and cooling system.

7.1. Subsystem Requirements

This section specifies the subsystem requirements specified for the structure subsystem as well as the configuration. The structure of the requirements follows the structure used in the baseline report [3], where each requirement is given a unique identifier which details the top down flow of requirements ensuring traceability. The structure subsystem was designed to comply with all requirements listed in Table 7.1.

Table 7.1: Structure subsystem requirements according to which the design was made.

ID	Requirement
REQ-STK07-STR03-ARM01	The propeller arms shall not deflect more than 2 mm, in any direction, when maximum thrust is applied.
REQ-STK07-STR03-ARM02	The propeller arms shall not have an slope deflection of more than 0.5 deg, in any direction, when maximum thrust is applied.
REQ-STK02-MIS30-MAP01-LDR01	The mapping system shall be placed on the UAS such that the FOV of the system shall not intersect with the swept area of the propellers
REQ-STK05-STR05-DIM01	The global dimensions of the system shall not exceed 68x68x38 cm (LxWxH).
REQ-STK18-MIS38-STR06-LND01	The system landing gear shall supply a ground clearance of 5 cm to the bottom of the central hub on flat ground
REQ-STK18-MIS38-STR06-LND02	The system landing gear shall absorb a 0.25 m vertical drop without permanent deformation to the structure.

7.2. Frame Configuration

It was established during preliminary design that a quad-copter configuration, with four rotor and a central bus, was optimal for the Fire-Eye application. Within the quad-copter category, there are many possible shapes for the frame connecting the rotors to the central hub. Most common are the 'X', 'I' and 'K' frames, each with different practical benefits.

In a comprehensive study, V. Kumar et al. explore the deformations and stresses of the mentioned frame configurations, as well as more exotic shapes [29]. The 'X' frame experienced the lowest peak deformations and stresses at constant material thickness for a range of materials. This is a positive result for weight reduction, as a thinner arm cross-section can be used without compromising strength. The 'X' frame is also beneficial for flight stability as it is double symmetric. This centers the c.g., which helps distribute thrust equally among the 4 propellers.

The 'X' frame layout was selected for further development with several aspects to be considered. First, requirement REQ-STK02-MIS30-MAP01-LDR01 specifies that states that the mapping subsystem's FOV should not intersect the propellers of the quadcopter. Section 4.7 lists all the hardware components

that are housed by the hub. The internal arrangement of all subsystems within the hub was optimized to achieve a compact package and a low center of gravity, both of which enhance flight stability. At the same time, the mission roles of each subsystem influenced their placement; for example, the communications module is mounted on the underside of the hub so that its antenna is always oriented toward operators on the ground. The resulting arrangement is illustrated in Figure 7.1. The propellers were placed in a square configuration to ensure even thrust and moment distribution, which is beneficial for stability and control. Due to placement of the LiDAR mapping system to comply with REQ-STK02-MIS30-MAP01-LDR01 the hub was moved forwards. This caused the propeller arms to be an uneven length as the hind propeller arms are longer.

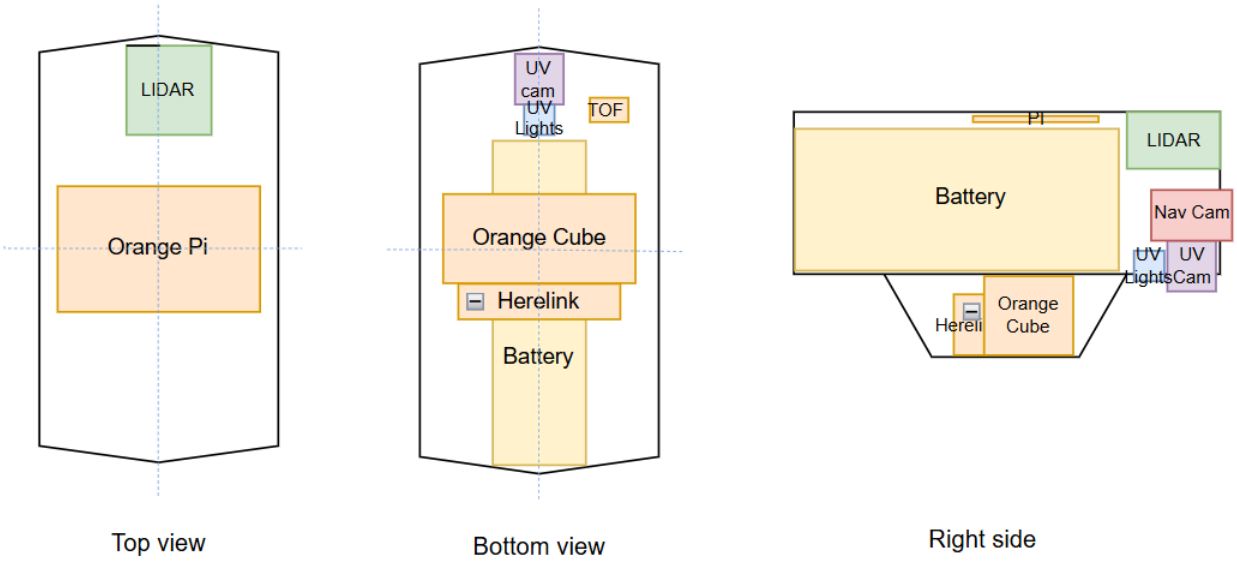

Figure 7.1: Packing arrangement of hardware within the hub

7.3. Propeller Arms

The arms to which the propulsion system is mounted is responsible for providing a load path for the thrust force. It is desired to keep the cross section of the arms as small as possible to avoid additional interference of the propeller downwash with the structure, however the arms need to withstand all operational loads experienced by the quadcopter. This section sizes the longest propeller arms of the quadcopter based on the operating condition where the propellers provide maximum thrust. Figure 7.2 shows the free body diagram of the arms which are rigidly connected to the body of the quadcopter.

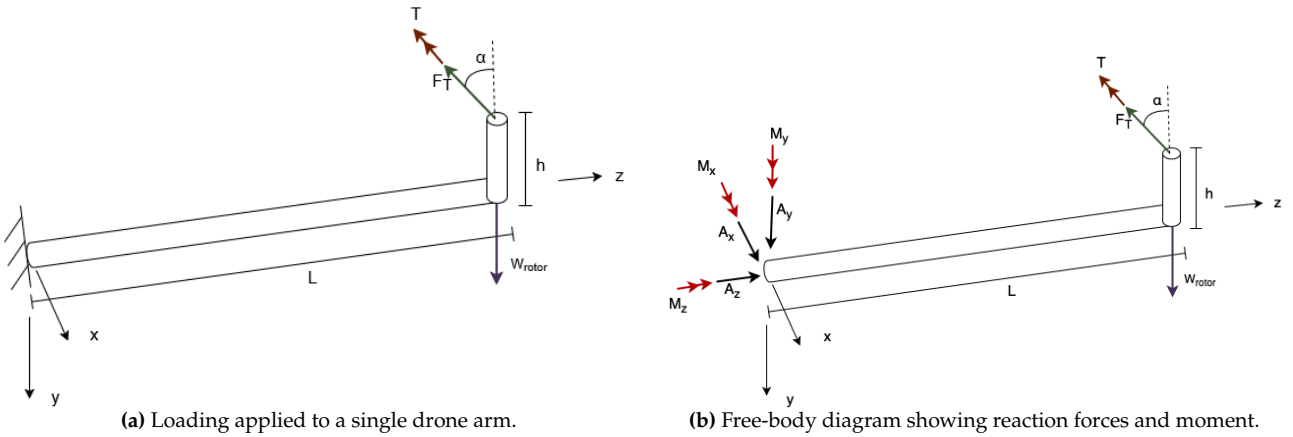

(a) Loading applied to a single drone arm.

(b) Free-body diagram showing reaction forces and moment.

Figure 7.2: Structural model and corresponding free-body diagram used for analyzing a drone arm as a cantilever under maximum thrust loads.

For the selected configuration and motor the limiting design case occurs when the motors on the longest propeller arms deliver maximum thrust. This corresponds to an arm length $L = 178$ mm and a height $h = 5$ mm with a maximum thrust force of 18.9 N and a torque of $T = 0.232$ Nm for the selected XING 2814 880kv motor [1]. To refrain form inducing a yawing moment a set of clockwise and counter clockwise spinning propellers are used, a counter clockwise rotation propeller induces a torque in the same direction as the thrust, whereas a clockwise rotating propeller induces a torque in the opposite direction of the thrust. As the applied torque is small in magnitude when compared to the thrust force this has a negligible influence on the result of the structural analysis.

The origin of the arm where it is rigidly connected to the quadcopter body experiences the largest stresses due to the increased moment arm, however to identify the point of maximum and minimum stress within the cross section, and therefore the design condition, the loading was divided into axial and shear stresses. The tool created during the design of the propeller arms allowed the tilt angle α to be a variable input however as explained Chapter 5 the use of a tilt angle was disregarded and as such $\alpha = 0$.

The stress experienced by the arm is calculated for a hollow circular cross section with an outer diameter d_0 of 20 mm and a wall thickness t of 1.5 mm. As the circular cross section is double symmetric the moments of inertia $I_{xy} = 0$ and $I = I_{xx} = I_{yy}$. Contributions to the axial stress include the moments M_x and M_y as well as the compressive force A_z. The stress due to bending was calculated using the formula for asymmetric bending for a double symmetric cross section or Equation 7.1 [30]. It should be noted that a positive moment M_y is defined as a moment that causes compression in the positive x-axis. The compressive force was calculated using Equation 7.2.

$$\sigma_z = \frac{M_x y - M_y x}{I} \tag{7.1}$$

$$\sigma = \frac{F}{A} \tag{7.2}$$

The shear stress experienced by the arm is caused by the force A_y and the torsional moment M_z. To calculate the shear stress due to a transverse shear force V Equation 7.3 is used, where the τ_{max} occurs along the x-axis as the first moment of area Q being greatest at this location. The shear stress due to a torsional moment T can be calculated using Equation 7.4 where R is the radius at which the shear stress is evaluated and J is the polar moment of inertia. The maximum stress due to torsion occurs where the radius R is the largest.

$$\tau = \frac{VQ}{It} \tag{7.3}$$

$$\tau = \frac{TR}{J} \tag{7.4}$$

After the stress due to each loading case is calculated the final stress state can be evaluated using superposition of the stress states [30]. To find the point where the stress due to bending is maximum the neutral axis of cross section was found, this was done by setting Equation 7.1 equal to zero where subsequently the angle to the positive x-axis, β was found to be 176°. The distances furthest away

[1] URL: https://rcdrone.top/products/iflight-xing-x2814-fpv-motor [Cited 16/06/2025]

from the neutral axis correspond to the maximum and minimum bending stresses. To account of uncertainties in the results of the structural analysis and maintain a margin for the design a safety factor of 1.5 was applied. The subsequent stresses and deformations were calculated using the safety factor. The location of the minimum and maximum axial and shear stresses are shown in Figure 7.3, whereas the magnitudes of the maximum and minimum stresses are reported in Table 7.2. The symmetry of the shear stress minima and maxima is expected as the only contribution to the shear stress for a tilt angle of $\alpha = 0$ is the shear force due to the thrust of the propulsion system. As this shear force is applied along the y-axis the shear stress is maximal along the x-axis and zero along the y-axis.

Table 7.2: Minimum and maximum stresses experienced by propeller arms at locations specified in Figure 7.3 for a safety factor of 1.5.

Stress	Value [MPa]
σ_{max}	12.7
σ_{min}	-12.7
τ_{max}	1.22
τ_{min}	0

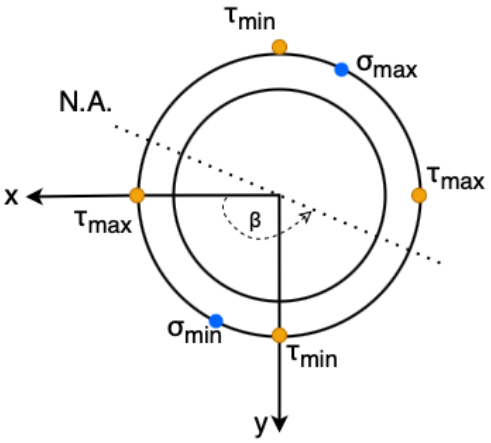

Figure 7.3: Hollow circular cross section of propeller arms and the location of maximum and minimum stresses.

Lastly the bending of the propeller arms is evaluated using the superposition of displacements. The displacements in each axis is calculated through the use of standard solutions [31] for a cantilever beam. Each bending mode was assumed to be independent and therefore linearly separable such that the deflections could be superimposed. This assumption is largely valid except for large torque loads which can cause create coupling in deflection modes, however as the bending moment is an order of magnitude larger than the torque it was deemed a valid assumption. The final calculated displacements are shown in Table 7.4. To comply with **REQ-STK07-STR03-ARM01** and **REQ-STK07-STR03-ARM02** the displacement and slope must be less than 2 mm and 1 deg respectively. For this the material PEEK reinforced with 30% carbon fiber was chosen. Initially unfilled PEEK and aerospace grade materials were considered however it was determined that unfilled PEEK provided insufficient stiffness and caused deformation in excess of 2 mm whereas aerospace grade materials did not fit the use case due to the light loading and high material costs. PEEK CF30 offers higher stiffness than unfilled PEEK while remaining a cheap, and widely available material with proven technology and manufacturing techniques, the material properties of PEEK CF30 are summarized in Table 7.3.

Table 7.3: Material properties summarized for PEEK CF30 [2] [3]

E [GPa]	G [GPa]	ρ [g/cm^3]	σ_{yield} [MPa]	σ_{ult} [MPa]
6.8	2.3	1.38	122	131

Table 7.4: Displacements of propeller arms under maximal operational loads with a safety factor of 1.5

	x-axis	y-axis	z-axis
Displacement [mm]	-0.22	-1.97	0
Rotation [deg]	-0.14	-0.96	0

7.4. Landing Gear

The functions of the landing gear include providing sufficient ground clearance for the rest of the system and absorbing impacts during landing. A well-designed landing gear is essential for the

protection of delicate components in the system.

The possibility of including retractable landing gear was discarded, as this feature would offer no significant benefits and the retracting mechanism would add weight. Skids, used in helicopters to avoid tipping when landing causes sudden deceleration, were considered unnecessary as the Fire-Eye UAS is not expected to maintain a horizontal velocity component during landing. It was therefore established that the landing gear would consist of four struts. The placement of the struts was explored; in commercial UAS, it is common to position the struts either below the propellers or directly beneath the central bus. See Figure 7.4.

Figure 7.4: Landing gear placement options (front view)

Configuration **A** offers better protection for the propulsion system. If the UAS was to experience tipping angles during landing, due to a gust of wind for example, the landing gear makes contact before the delicate propellers. While the propellers are relatively easy to replace, the specialized payload sensors are expensive, niche and critical to Fire-Eye's mission. Configuration **B** offer better protection these sensors when landing on uneven terrain. In this configuration the bus, the bulkiest part of the structure, absorbs the impact. This is preferable to landing on struts beneath the rotor, which would introduce critical bending loads into the arms. Reinforcing the arms' cross would add undesired weight to the UAS. For weight reduction and the protection of specialized payload, configuration **A** was selected.

It was established that the UAS should have a minimal ground clearance of 5cm, allowing would allow for landings on irregular surfaces. With the arms deflecting less than a millimeter at maximum thrust loading, the propellers are kept well above the ground. It was decided that placing the struts at an outward tilt angle would be highly beneficial for the design. By implementing a tilt angle, the distance between the struts is increased, reducing the UAS' tendency to tilt on the ground. Furthermore, it was necessary to prevent the struts from interfering with the payload's field of view. Exceeding the FOV of the payload, an outward tilt of $\theta = 45$ was established. To maintain ground clearance with the implemented tilt angle, a strut length of $L_{strut} = 0.13m$ was required, as illustrated in Figure 7.5.

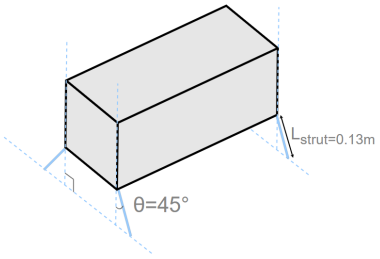

Figure 7.5: Simplified schematic showing strut geometry (not to scale)

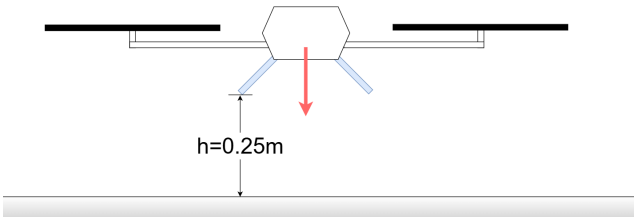

Figure 7.6: Hard landing scenario description

To design the landing gear structure, a hard landing was considered as the critical scenario. Such a scenario could occur if, for example, a less experienced operator attempts to land. This scenario was modeled by a fall of h=0.25m, as illustrated in Figure 7.6. During impact, the landing gear "is effectively rigid in compression" and the gear load is a function of bending [4]. It is assumed that the potential energy from the drop is translated to elastic potential energy, distributed over the four struts in bending:

[4]URL: https://ntrs.nasa.gov/api/citations/19670023065/downloads/19670023065.pdf [Cited 11/06/25]

$$E_{pot} = \frac{m_{MTOW}}{4} g h \rightarrow U_{bend} = \frac{1}{2} k_b \delta^2 \tag{7.5}$$

The bending stiffness of a beam clamped at one end is given as:

$$k_b = \frac{3 E_{mat} I}{L^3}, \tag{7.6}$$

where E_{mat} is the elastic modulus of the selected material and I is the moment of inertia of the cross section. From Equation 7.5 and Equation 7.6, the bending deflection δ as the leg hits the ground is can be deduced. The peak force experienced by a single leg during the impact, and thus the critical scenario that must be designed for, is shown in Equation 7.7.

$$F_{max} = k_b \delta = k_b \sqrt{\frac{mgh}{2k_b}} = \sqrt{\frac{mgh}{2} \left(\frac{3 E_{mat} I}{L^3} \right)} \tag{7.7}$$

From Equation 7.7 it becomes apparent that a lower peak force is transferred when a material with a lower elastic modulus is selected. By reducing stiffness, the loads transferred to the bus (where delicate sensors are stored) can be reduced. However, reducing stiffness also increases deflection, which can compromise structural integrity. The maximum stress due to bending within the strut's cross section takes place at the outermost radius. Applying Equation 7.1, the stress can be calculated as:

$$\sigma_{max} = \frac{F_{max} L (d_{out}/2)}{I} \tag{7.8}$$

Taking a safety factor of 1.5 into account, the criterion to avoid the struts' failure due to yielding is $1.5\sigma_{max} < \sigma_{yield}$. Different materials and cross sections that could meet this criterion were explored in an iterative process. A tubular cross section was selected due to its superior performance in bending. Initally, PEEK CF30 was considered as a potentially suitable material due to its consistency with the arms. However, meeting the failure criterion with this material required a relatively thick cross section, resulting in heavier struts. The analysis eventually converged to carbon fiber struts with an outer diameter of 15mm, offering high performance and minimal weight. Table 7.5 summarizes the material properties of carbon fiber.

Table 7.5: Material properties summarized for carbon fiber [5]

E [GPa]	ρ [kg/m^3]	σ_{yield} [MPa]
3.5	1600	230

For a tubular carbon fiber strut with an outer diameter of 15mm, the minmim required thickness to meet $1.5\,\sigma_{\max} = \sigma_{yield}$ under a 0.25 m drop was calculated as t_{req}=0.87mm. This was conservatively rounded up to 1mm due to manufacturing considerations. The final landing gear design is lightweight, each strut weighing approximately 4 grams. It was calculated that the maximal deflection during hard landing remains below 1cm, suggesting there is no issue with ground clearance. The final landing gear specifications are presented in Table 7.6

[5]URL: https://optlasers.com/everything-about-carbon-fiber-tubes [Cited 17/06/2025]

Table 7.6: Final landing gear specifications

Parameter	Value
Number of struts	4
Strut material	Carbon fiber
Outer diameter D_{out}	15mm
Wall thickness t_{req}	1mm
Strut length L	0.13m
Tilt angle θ	45
Ground clearance	50mm
Maximum deflection δ	8.9mm
Total gear mass	16g

It must be noted that the methodology used to size the landing gear makes many simplifications. It was assumed that the UAS falls perfectly perpendicular a flat surface and that the impact is absorbed purely in bending. Real-world scenarios will differ from this idealized situation. It is therefore recommended for the post-DSE phases that physical hard landing tests are performed on Fire-Eye prototypes.

7.5. Hub

The 'hub' is the central part of the quadcopter's frame. It connects the arms and houses vital subsystems of the UAS. As such, it must provide structural rigidity, power and a safe operating environment for subsystems

Different approaches can be taken when designing the hub. Racing drones typically feature a skeletal hub, consisting of exposed spars and electronics to reduce weight. Consumer drones are trending towards integrated frames, where the arms seemingly blend into the hub. This design offers better protection for electronics, but complicates repairs and modifications. Fire-Eye's hub must house delicate subsystems operating in harsh post-fire environments. Its design must also support repairability and modularity. An enclosed modular hub was identified as the optimal solution. In this design, the hub includes a protective skin (casing) for the electronics and sockets to securely hold the arms.

Skin

The design choice to encase the hub with a skin followed from the need to protect delicate subsystems from the environment. The addition of a skin comes at a cost, as it weight is added to the hub. Modern UAS designs counter this problem by ensuring that the skin acts as a load-carrying structure, reducing or eliminating the need for spars within the casing.

Section 7.3 describes load transfer in the arms. The hub must provide reactions to the loads at the root of the arms illustrated in Figure 7.2a. The largest reaction force and moment that must be provided are A_y and M_x respectively. An efficient to provide these reactions would be a socket as illustrated in Figure 7.7a. A second layer of skin in parallel gives the socket a depth 's'. This socket is filled with a light foam to prevent skin buckling. By providing reaction forces A_{y1} and A_{y2} in opposing directions, the socket provides a reaction moment.

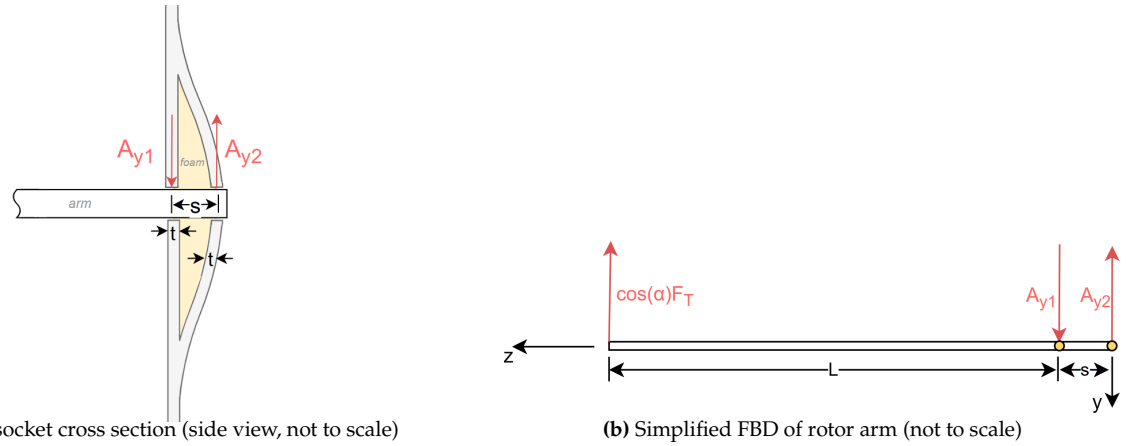

(a) Arm socket cross section (side view, not to scale)

(b) Simplified FBD of rotor arm (not to scale)

Figure 7.7: (a) Arm socket cross section and (b) simplified free-body diagram of the rotor arm.

An FBD showing the interaction between the rotor arm and the socket is presented in Figure 7.7b. This analysis focuses on the rear arms, which exert greater bending stresses as they are longer. For $L = 0.19m$, $s = 0.01$ and a maximum rotor force of $F_T = 0.9 * 9.81$, it can be solved that $A_{y1} = 158.9N$ and $A_{y2} = 167.8N$. The skin must be designed to endure internal stresses as these loads are transferred. For this architecture, bearing failure and shear tear-out failure are important to consider. These failure modes are illustrated in Figure 7.8, inspired by the Aerospace Structures & Materials course content [6].

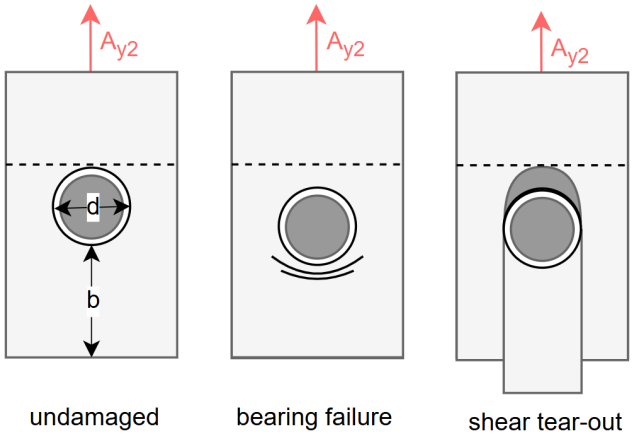

Figure 7.8: Failure modes

Bearing failure occurs when an object presses against the walls of the hole in which it is installed, plastically deforming it. In shear tear-out, the section between the hole and the free edge of the skin fails in shear. Equation 7.9 and Equation 7.10 describe the critical stress for each failure mode. These equations make use of the section's geometry. In this analysis, **d=0.02m** and **b=0.086m**.

$$\sigma_{\text{bearing}} = \frac{F}{d \cdot t} \tag{7.9}$$

$$\tau_{\text{shear}} = \frac{F}{2\,b \cdot t} \tag{7.10}$$

Taking a safety factor of 1.5, the allowed stress is defined as $\sigma_{allow} = \sigma_{yield}/1.5$. Polycarbonate and PEEK were considered as the hub's complex shape will be produced with 3D printing. Considering the allowed stress, the minimal skin thickness required to prevent bearing failure and shear tear-out respectively are presented in Table 7.7 for both materials.

[6] URL: https://ocw.tudelft.nl/course-readings/7-2-6-main-takeaways-on-failure-of-mechanically-fastened-joints/ [Cited 12/06/2025]

Table 7.7: Minimum wall thickness requirements for bearing and shear failure modes, for polycarbonate and PEEK

Material	σ_{yield} (MPa)	ρ (kg/m^3)	t_{bearing} (mm)	t_{shear} (mm)
Polycarbonate [7]	60	1200	0.210	0.024
PEEK [8]	100	1300	0.126	0.014

For both materials, the minimal thickness to meet either failure mode is far below 1mm. In practice, such thin sheets cannot be manufactured. Therefore, a realistic thickness of 1mm is established. For the thickness of 1mm, the resistance of the sheet to buckling must be analyzed. Equation 7.11 describes the critical buckling stress. **C** accounts for the boundary conditions - a C value of 1 is assumed here as the skin only has some support from the foam. This is a conservative estimate. The Poisson ratio, Equation 7.12, relates the elastic modulus of a particular material to its shear modulus.

$$\sigma_{\text{cr}} = C\frac{\pi^2 E}{12\,(1-\nu^2)} \cdot \left(\tfrac{t}{d}\right)^2 \qquad (7.11)$$

$$\nu = \frac{E}{2\,G} - 1 \qquad (7.12)$$

The stress applied to the section was calculated by considering the applied load A_{y2} and the section's geometry. Table 7.8 compares, for both materials, the stress applied to the skin with the critical buckling stress, for a thickness of 1mm.

Table 7.8: Comparison of applied and critical buckling stresses for t = 1mm skin

Material	t (mm)	σ_{appl} (MPa)	σ_{cr} (MPa)
Polycarbonate	1	1.15	5.50
PEEK	1	1.15	8.50

For both materials, the stress carried than the skin is several times lower than the critical buckling stress. Hence, the structural analysis confirms that either material can provide sufficient strength for the skin. Additionally, in practice the foam at the socket provides additional support against buckling. Polycarbonate was selected as its lower density results in a lighter skin at a fixed thickness. Moreover it is an easily processable material, which is beneficial when producing complex geometries such as the hub.

The same analysis was performed for the landing struts in the critical 'hard landing' scenario. The situation was practically identical, but the skin had to carry a greater load. The analysis resulted in a 2mm thickness requirement for the bottom plate.

Although it makes use of simplifications, this method achieves a robust and lightweight design that remains well within the defined stress limits, even when safety factors are applied. The required skin thickness was determined by the structural analysis at the arm root (see Section 7.3), which showed zero force (A_z) and torsion (M_z) around the arm's z-axis. Consequently, the skin sizing focused on resisting the bending moment M_x and vertical reaction forces. Finally, to restrain the remaining unaddressed degrees of freedom (especially during maneuvers or manual handling), a simple, lightweight brace [9] will be added at the arm tip.

Modular payload mount

The hub houses the mission payload, providing both power and structural support. A important feature of Fire-Eye's payload design is modularity. The hub must therefore include mounting interfaces so that payload can easily be swapped to tailor the UAS for each specific mission.

[7] URL: https://asia.arrk.com/wp-content/uploads/2024/08/CNC-PC_Updated-.pdf.pdf [Cited 17/06/2025]
[8] URL: https://designerdata.nl/materials/plastics/thermo-plastics/polyetheretherketone [Cited 17/06/2025]
[9] URL: https://www.jmrdrone.com/drone-cnc-machining-parts/57407449.html [Cited 13/06/2025]

Commercially available mounts generally involve mechanically securing the payload to the UAS by means of a screw[10]. This design allows the user to manually adjust the orientation of the payload with respect to the hub. This was considered unsuitable for the LiDAR, which requires consistent alignment with respect to the IMU's in the hub in order to produce accurate 3D maps.

A click-mount was identified as a suitable solution, providing structural support and a consistent orientation every time the LiDAR is mounted. These simple mechanisms, used in many applications, allow for rapid payload swaps[11]. The synthetic materials used to produce click-mounts are compatible with 3D printing, so a mount could be produced to match the dimensions and weight of the LiDAR system. Figure 7.9 visually describes the mounting configuration. The mount includes a dock for the Voyant Helium LiDAR power supply.

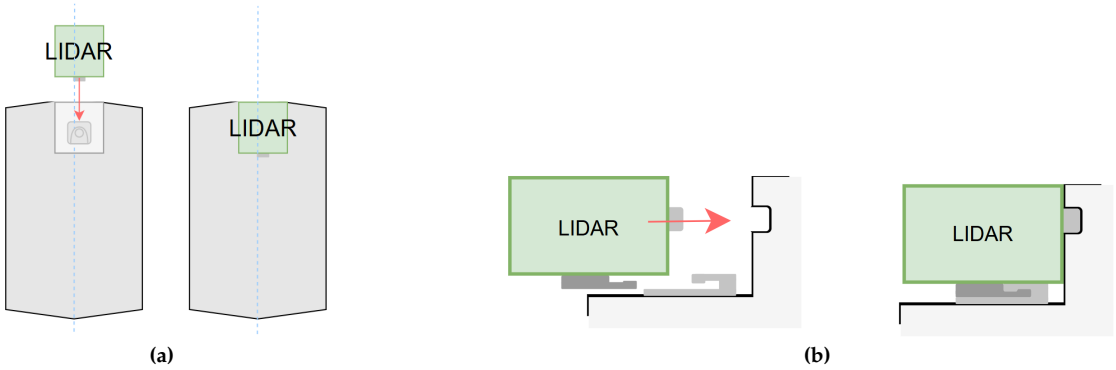

Figure 7.9: LiDAR click-mount configuration: (a) top view and (b) side view (cross section).

It was decided that the forensic detection system would not have a modular payload mount as the total weight of the forensic system is 23 g. It is likely that a modular mount for the forensic system would have a very similar weight, therefore negating the effects of a reduction in weight when not in use.

Cooling

The hub of the quadcopter contains many subsystems which produce excess heat which needs to be regulated to avoid overheating of vital components. Active cooling systems are often heavy and require a large amount of power, further increasing the weight and power required of the drone. Passive cooling systems lack feasibility due to the confined space the of the hub and the lack of a path by which the heat can escape. Therefore it was decided that the downwash created by the propeller can be repurposed for cooling. As the propeller arms are place under the propellers they experience a force due to the downwash interacting with the propeller arms, this air that interacts with the arms can be funneled though a cutout in the arms into the hub of the drone through which it can cool vital components and eventually be expelled out the bottom of the drone.

Two variations of cutouts were considered, a singular larger elliptical cutout along the length of arm and many smaller circular cutouts. An elliptical cutout was decided upon as many circular cutouts could cause similar stress concentration factors, while likely offering less performance due to the viscous effects of flow thought small openings. The stress concentration factor experienced by the propeller arms depends on the configuration of the circular holes as well as the dimensions of the elliptical cutout. The location of the cutout affects the performance of the cooling as the mass flow experienced by the cutout depends on the radial distance from the propeller hub. The radial distance from the propeller hub that experiences the highest downwash is in the range of 0.4-0.6 times the radius of the propeller [32]. For the selected propellers of 12.7 cm radius this corresponds to a a position of 5.0-7.5 cm from the center of the hub. The cutout was placed at the location with the highest downwash velocity as this would cause the highest mass flow through the cutout.

shows an illustrative representation of the proposed cutout, the proposed dimensions are b = 1 cm

[10]URL: https://www.dronekenner.nl/en/video-and-fotography/mounts-and-adapters/50cal-sports-cam-holder-bracket-mount-for-air-3-gopro-12/ [Cited 13/06/2025]

[11]URL: https://www.recon-company.com/en/peter-jones-klick-fast-system-dock-guertelclip/893155 [Cited 13/06/2025]

and $a = 2.5$ cm centered at a distance $d = 6.25$ cm away from the hub of the propeller. This allows the region in which the downwash is the highest to be redirected for cooling while preserving a load path for the stresses to be redistributed across. As the dimensions of the cutout are small and the arm is lightly loaded, the effects are localized around the hole and only require local reinforcement [30], it should be noted that a larger cutout would result in a larger stress concentration factor. It is proposed that the additional required reinforcement is supplied through the use of a donut doubler. The detailed analysis of the required local reinforcement is to be done in a the detailed design stage as the cutout is expected to have the largest impact on the bending displacement and fatigue properties of the propeller arm. The expected behavior of the propeller arm can be modeled though FEA analysis or experimental tests which can determine the required reinforcement.

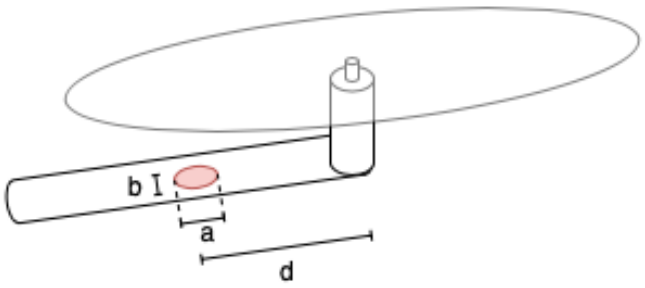

Figure 7.10: Illustrative drawing of proposed cutout to facilitate cooling of hub components

To find a first order estimation of the mass flow through the cutout, the induced velocity of the chosen propeller and motor combination was used. It was found that the average induced axial velocity of the propeller in the range of 5.0-7.6 cm from the hub of the propeller is 19.35 m/s, with a cutout area of 1.9635 cm^2 this corresponds to a mass flow of 0.47 kg/s. The environment in which the Fire-Eye quadcopter operates is likely to be covered in ash and debris, to filter this ash and debris a non-load carrying mesh is be placed in the cutout. Lastly a second cutout is placed on the hub skin such that the air can be expelled from the body, the preferred placement of the cutout is in the top or the rear of the hub as these locations are expected to carry smaller loads and contribute less to the scene disturbance.

7.6. Verification and Validation

This section covers the verification and validation of the design tools used throughout the development of the Fire-Eye quadcopter structure. During the analysis fo the propeller arms performed in Section 7.3 a design tool was created that was able to analyze the structure for any tilt angle α, this tool was used to calculate the reaction forces at the origin of the propeller arms, analyze stresses at the origin and calculate the expected deformations under the provided load scenario. Design tools were created for the landing gear and hub skin sizing. These tools made use of several equations with results feeding into each other. Individual equations were verified by printing intermediate results and comparing them to manual calculations.

Verification

The verification of the propeller arm design tool was implemented thought a series of unit and system tests as well as a sensitivity analysis of input parameters using the unittest python package. A testing `class` is created in which mock data is created and the expected result of a test is compared to the implementation in the design tool. Unit tests are performed on a smaller scale as they test individually defined `functions`, this includes a test to calculate the neutral axis of the cross section as well as the bending deformation. When calculating the neutral axis for a moment $\vec{M} = \vec{0}$ it was found that the function returned a value of $\pi/2$ rather than raising an error which is the intended behavior, this was fixed by raising a `ValueError`. In the calculation for the deformation due to bending it was found that the implementation cause a positive y moment, as defined in the coordinate frame in Figure 7.2, resulted in a negative deflection in the x direction, when the expected result is a positive x deflection. This was caused by an error in how the deflection calculation function was called, a fix was applied and the documentation of the function updated to reflect this. All other performed unit tests passed, these included unit tests to calculate the reaction forces at an arbitrary point, calculation of the axial

and shear stresses experienced by the cross section, the crippling buckling load as well as the torsional deformation. System tests aim to ensure correct flow of information from unit to unit, assessing the integrity of the code as a whole. As such it combines multiple unit test together and subsequently compares the expected result to the obtained result, system level tests that were performed are the flow from calculated reaction forces to the neutral axis calculation as well as the calling of the wrapper function `calculate_stresses` which calls functions that calculate the individual stress components, all system tests were passed and no abnormalities were recorded indicating correct flow of information from function to function.

The result of the structural analysis is sensitive to the input parameters used, a difference in the input parameter will have a large effect on the experienced deflections. It is expected that the outer diameter d_0, the wall thickness t and the Young's modulus E have a large influence on the deflection in the y direction. A sensitivity analysis was performed where each of the above mentioned parameters was varied and their influence on the deflections in the y direction quantified. Figure 7.11-7.13 shows the result of the sensitivity analysis, all three parameters have an influence on the experienced deflection showing the expected behavior, where an increase in the parameter leads to a decrease in the deflection.

The deflection experienced by the arm is very sensitive to the outer diameter of the cross section d_0. This is as a smaller outer diameter has a large influence on the moment of inertia of the cross section, leading to a higher deflection. As such the outer diameter should be verified during assembly of the product, however since the design outer diameter is $d_0 = 25$ mm the impact is not as severe as at lower outer diameters.

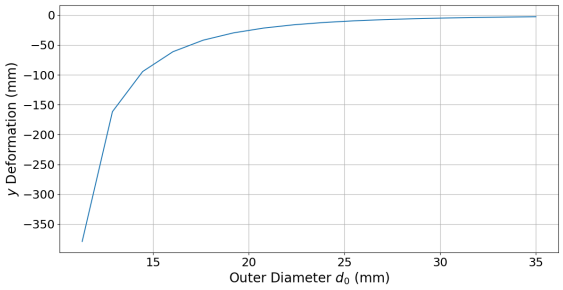

Figure 7.11: Sensitivity analysis of outer diameter of propeller arm.

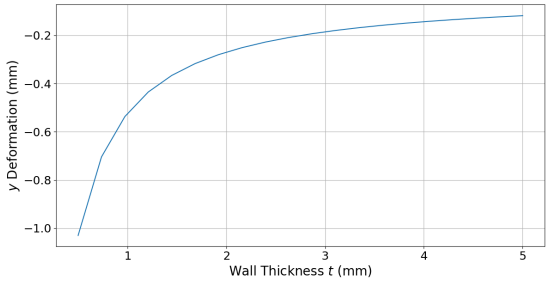

Figure 7.12: Sensitivity analysis of wall thickness of propeller arm.

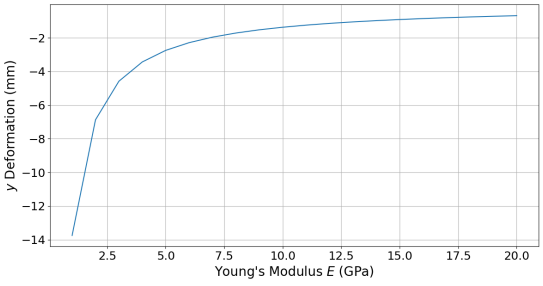

Figure 7.13: Sensitivity analysis of Young's modulus of propeller arm.

Running a coverage test using the python package `coverage.py` reveals a coverage of 96% of the file `Structures_arm.py` with only 2 lines of code not being run as they are related to conditional if statements, Figure 7.14 shows the coverage percentage.

File ▲	function	statements	missing	excluded	coverage
Detailed_design/Structures_arm.py	calculate_arm_forces	5	0	0	100%
Detailed_design/Structures_arm.py	calculate_section	4	0	0	100%
Detailed_design/Structures_arm.py	calculate_shear_stress	9	2	0	78%
Detailed_design/Structures_arm.py	calculate_neutral_axis	3	0	0	100%
Detailed_design/Structures_arm.py	calculate_axial_stress	4	0	0	100%
Detailed_design/Structures_arm.py	calculate_stresses	5	0	0	100%
Detailed_design/Structures_arm.py	calculate_buckling	2	0	0	100%
Detailed_design/Structures_arm.py	calculate_deformation	9	0	0	100%
Detailed_design/Structures_arm.py	calculate_torsion_deflection	2	0	0	100%
Detailed_design/Structures_arm.py	calculate_mass	3	0	0	100%
Detailed_design/Structures_arm.py	*(no function)*	11	0	0	100%

Figure 7.14: Coverage percentage of verification tests for propeller arm structural analysis.

Validation

A conservative safety factor of 1.5 was incorporated in all structural checks, to cover uncertainties in materials properties or manufacturing imperfections. Nonetheless, to gain full confidence that the structural sizing and stress predictions are reliable, they must ultimately be validated against real-world test data. FEA analysis is not a method by which the structure can be validated as this requires the validation of the FEA software itself. No sources were found describing experiments validating the specific combinations of geometries and materials used in the Fire-Eye structures, or the technical details on existing structures found within commercial drones. This presents a lack of validation opportunities as real-world data is lacking to which the Fire-Eye structure can be compared to. An alternative method of validation is performing experimental tests on representative or simplified strcutures. This can be done at a component level as well as a system level to validate both individual design tools as well as the Fire-Eye structure as a whole, as such it is recommended for the post-DSE phase that experiments such as cantilever bending and drop-tests are performed, ensuring that the structures offer sufficient strength and stiffness in practice.

8 - Navigation & Control

This chapter details the navigation and control systems of the Fire-Eye quadcopter, ensuring stable and responsive operation in confined post-fire environments. Section 8.1 outlines the human piloted navigation approach, supported by onboard sensors for precise maneuvering. Section 8.2 presents the cascaded PID control architecture, including system modeling and stability analysis. Section 8.3 highlights performance validation and the verification of the model and methods used. In Section 8.4 the limitations of the model are discussed and finally, in Section 8.5 a sensitivity analyses is performed to evaluate robustness to mass and thrust variations.

8.1. Navigation

Throughout the mission the Fire-Eye quadcopter will be navigated under the control of a human pilot. This is done to comply with governmental regulations on UAS operators and remote pilots [1]. In addition, during its mission the Fire-Eye system will look for human remains among the remnants and debris of a burned building. There is no guarantee that these remains are directly in line with the flight path, so the navigation of the Fire-Eye should allow for unplanned flight path deviations. Although autonomous systems can be programmed to accommodate such changes, remotely piloted systems offer greater flexibility in adapting to these unpredictable conditions. Table 4.4 discussed the data- and telemetry link between the onboard systems and the remote controller. In following sections of the chapter it will be discussed how the pilot can navigate the quadcopter through control inputs.

To support precise and stable piloting, the Fire-Eye drone integrates several onboard sensing systems. The Cube Orange+ flight controller contains multiple redundant Inertial Measurement Units (IMUs), which measure angular velocity and linear acceleration to determine the drone's attitude and support flight stabilization even in the event of a single sensor failure[2]. IMUs operate by combining data from gyroscopes and accelerometers to track motion and orientation changes in real-time. The data captured by the IMU's is send to the flight controller, where the software transforms the angular velocities and linear accelerations into a required thrust for each of the motors.

In addition to the IMU's, the quadcopter is equipped with two Time-of-Flight (ToF) laser sensors that can detect obstacles up to 50 meters away[3]. ToF sensors function by emitting a laser pulse and calculating the time it takes for the reflection to return, offering reliable measurements even in larger interior volumes. The downward-facing ToF sensor provides continuous altitude estimation relative to the ground, and the second forward-facing ToF sensor, assists in obstacle detection by measuring the distance to walls or objects directly ahead, allowing the pilot to make informed decisions when navigating confined spaces. Additionally, onboard cameras provide a real-time visual feed to the remote operator, offering critical visual cues for navigation and enabling manual adaptation to complex or dynamic environments.

Software Block Diagram

Figure 8.1 illustrates the software block diagram of the Fire-Eye quadcopter. It outlines the main software programs and firmware components implemented in the system. Programs (shown in red) represent the high-level software running on devices such as the Herelink controller, Herelink Airunit, flight controller (Cube+), and the companion computer (Orange Pi 5). Firmware components (shown in blue) include the embedded software used within subsystems such as the ESCs, ToF sensors, LiDAR sensor, UV LED trigger, and both onboard cameras.

[1] URL:https://eur-lex.europa.eu/eli/reg/2019/947/oj [Cited 17/06/2025]

[2] URL: https://docs.px4.io/main/en/flight_controller/cubepilot_cube_orangeplus.html [Cited 10/06/2025]

[3] URL: https://www.waveshare.com/tof-laser-range-sensor-c.htm?sku=28760 [Cited 10/06/2025]

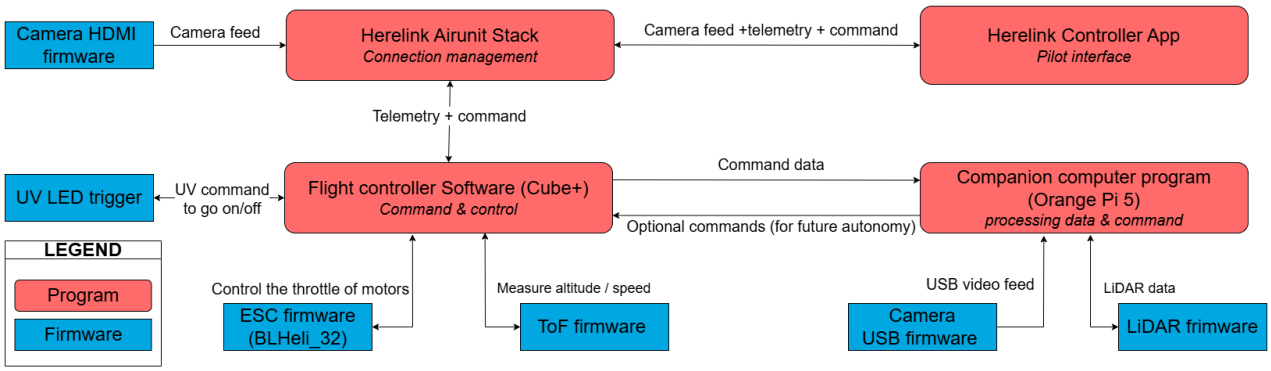

Figure 8.1: Software block diagram showing interaction between programs and firmware modules

The diagram shows how each software element is deployed across the system. The Herelink Controller App runs on the ground station by the pilot and communicates with the Herelink Airunit Stack on the quadcopter, which manages the connection link. The Cube+ runs flight controller software that handles command execution and system control. The Orange Pi 5 runs a lightweight companion program used mainly for storing data from connected sensors.

Similarly, the firmware modules correspond to specific components in the system. The ESC firmware (`BLHeli_32`) controls the motors, the ToF sensor firmware provides altitude and velocity measurements, the LiDAR firmware handles point cloud generation, the USB and HDMI camera firmware manage image capture and the UV LED firmware enables on-off switching via digital input.

8.2. Control

As previously stated, the flight controller plays an important role in maintaining stable flight, but it is also essential for achieving safe, reliable, and responsive flight. The flight controller is the hardware component onboard of the quadcopter, which has an associated software; the flight controller software, or firmware. The firmware is essentially the brain of the system, receiving data from sensors and the operator, executing algorithms and calculations and then relaying signals to orient, and move the quadcopter by controlling the ECS as shown in Figure 8.1. Since the Fire-Eye quadcopter will operate in confined spaces, reliable and precise flight control is crucial. Consequently, design selections and considerations are made with a strong emphasis on system stability and responsiveness.

Flight controller firmware

The flight control firmware of the Fire-eye quadcopter considered for this report is a custom controller build in Matlab Simulink [4]. Open-source flight controller software such as Ardupilot [5]and PX4 [6] proved trusted, powerful and versatile platforms for the control of UAS, like quadcopters. However, their complexity makes them less suitable for direct implementation at the current development phase of the Fire-Eye system. As a result, a custom flight controller was developed, specifically tailored to the establishment of the stability and control characteristics of the Fire-Eye system at the current design and development phase. However, going into later stages of development, the implementation of such open-source software should be considered, as they are already well-established and complete, and could therefore significantly reduce the development phase of the control and stability subsystem. The architecture of the custom controller will be partially inspired by these open-source tools, to emulate their control logic and to allow for a fluent adaptation.

Control architecture

At its core, the controller developed for this report will follow the same control logic as Ardupilot and PX4's control firmware, as it will control the quadcopter via control loops consisting of the variables position, attitude and angular rate in a cascaded PID loop architecture. These variables will be

[4]URL: https://nl.mathworks.com/products/simulink/performance-improvements.html [Cited 17/06/2025]
[5]URL: https://ardupilot.org/copter/docs/common-thecubeorange-overview.html [Cited 17/06/2025]
[6]URL:https://docs.px4.io/main/en/flight_controller/cubepilot_cube_orange.html [Cited 17/06/2025]

independently regulated using PID controllers that will output signals that are eventually converted to torque and thrust inputs commands for the motors. Note that other control logic exists, but PID control was chosen because of its wide range of applications, easy implementation and it being the control logic of the ArduPilot copter controller.

PID controllers are instruments that are commonly used in the control systems. They receive data from sensors, the actual value, and compare that to a reference signal. Based on the difference between the actual value and the desired setpoint, called the error, it adjusts output to the control variables. The PID controller consists of a Proportional (P), Integral (I), and Direct (D) control block through which the error is adjusted into the output.

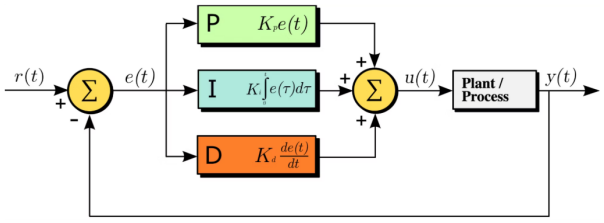

Figure 8.2: PID control block [7]

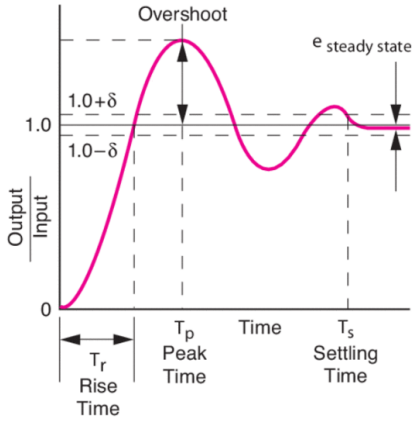

Figure 8.3: Control Theory Terminology[8]

The proportional component of the PID depends only on the error term that it is fed. The proportional gain (K_c) is the ratio between the output response and the input error term. Increasing the proportional gain typically reduces the rise time and steady-state error, but it also leads to higher overshoot and can degrade overall system stability, potentially causing the system to oscillate out of control. Figure 8.3 shows how these terms are defined in control theory. The integral component integrates the error term over time. The integral component therefore needs an error term to affect the system. Small error terms will sum and cause the integral component to increase slowly unless the error goes to zero. The integral component should in turn drive the steady-state error to zero. The integral gain (K_i) therefore reduces the steady-state error and rise time, but tends to increase overshoot and settling time, which negatively impacts stability. Finally, the derivative component is proportional to the rate of change of the error. Large time steps in the control system will cause the system to respond more strongly, decreasing the settling time. However, for large time steps the response is more sensitive to noise, so generally smaller derivative times are chosen [9]. Increasing the derivative gain (K_d) can improve stability, while also decreasing overshoot and settling time, with minimal effect on rise time. Furthermore, under ideal conditions, increasing the derivative gain does not influence the steady-state error. The effects of changing the PID gains are summarized in Table 8.1

[7] URL: https://dewesoft.com/blog/what-is-pid-controller [Cited 12/06/2025]
[8] URL: https://www.newport.com/n/control-theory-terminology [Cited 18/06/2025]
[9] URL: https://www.ni.com/en/shop/labview/pid-theory-explained.html [Cited 18/06/20205]

Table 8.1: Summary of PID Component Effects on Control System Performance

Component	Function	Rise Time	Overshoot	Settling Time	Steady-State Error
Proportional (K_p)	Proportional to error	Decreases	Increases	Small change	Decreases
Integral (K_i)	Integrates error over time	Decreases	Increases	Increases	Eliminates steady-state error
Derivative (K_d)	Proportional to rate of error change	Minor effect	Decreases	Decreases	No effect (theoretically)

Based on the effects of the individual proportional, integral, and derivative gains described, the gains of each component of the PID controller can be tuned to change the system's behavior and obtain a desired response..The main objective in designing the control system of the Fire-Eye is to achieve minimal overshoot and reduce the response time. To avoid collisions and reliably navigate within the confined spaces of its operation environment, minimal overshoot and rapid response is crucial. Having a reasonably high settling speed is preferred, but less essential, as careful and precise maneuvering is prioritized. Minimal overshoot ensures responsive behavior without excessive oscillations or instability that could pose risks.

There are several methods to tune the gains of the cascaded PID loops used in this system. One common and intuitive approach is manual tuning. Here the P, I, and D gains are adjusted iteratively while the system's response is observed. It is the most fundamental and straightforward method and has therefore been broadly explored. Common approaches are widely available. For example, PX4 provides a general description of the tuning of various PID control loops [10]. Although this method is time consuming, it provides direct insight into the system behavior and is useful during early development phases. Another approach available is the autotune tool in MATLAB Simulink, which provides an automated way to estimate appropriate PID gains based on the system model. This method can significantly reduce tuning time and provides a good initial set of gains, especially useful for linearized models or during simulation-based development. Since quadcopters are non-linear systems, the use of this tool should be carefully considered.

Besides manual tuning and autotuning, various advanced tuning methods can be considered, such as Ziegler-Nichols, Cohen-Coon, optimization-based tuning, or model predictive tuning strategies. These methods often offer improved performance or robustness, especially in systems with nonlinearities or time-varying dynamics. However, such techniques may require more detailed modeling and computational resources. For this reason, they may be considered for later stages of development.

Configuration

This subsection marks the beginning of the analysis of the Fire-Eye quadcopter's stability and control characteristics. It addresses the system's static behaviour and presents the configuration and coordinate conventions that will be used throughout the remainder of the analysis.

Figure 8.4 below illustrates the coordinate system and the motor numbering convention. This numbering convention does not follow conventional numbering schemes such as those used by ArduPilot [11] or PX4 [12]. However, this configuration was defined early in the design process and has been maintained for consistency ever since. The Fire-Eye quadcopter is modeled using a right-handed, body-fixed reference frame. This is a reference frame attached to a moving body in which the X-axis aligns with the direction of flight, the Y-axis points to the right with respect to the flight path, and the Z-axis points downward perpendicular to the propeller plane. Within this configuration, motors one and three produce positive yaw torque with respect to the Z-axis, while motors two and four produce negative yaw torque. The orientation of the vehicle is described using the conventional aerospace angles: roll (ϕ) about the X-axis, pitch (θ) about the Y-axis, and yaw (ψ) about the Z-axis.

[10] URL: https://docs.px4.io/main/en/flight_stack/controller_diagrams.html [Cited 18/06/20205]
[11] URL: https://ardupilot.org/copter/docs/connect-escs-and-motors.html [Cited 17/06/2025]
[12] URL: https://docs.px4.io/main/en/airframes/airframe_reference.html [Cited 17/06/2025]

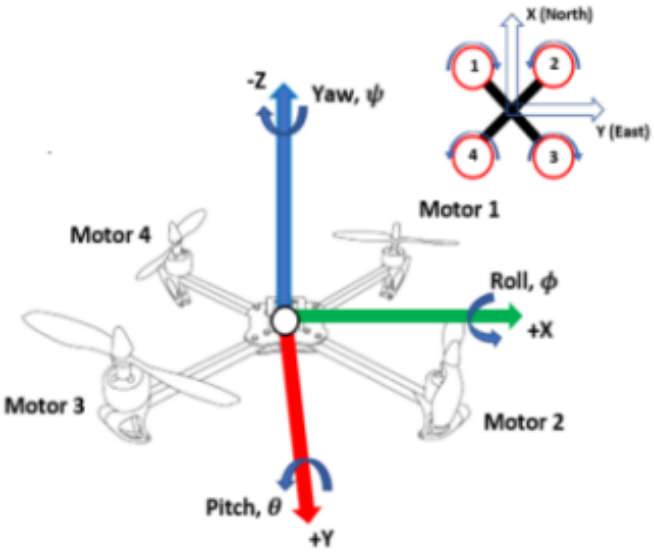

Figure 8.4: Quadcopter 'x' orientation configuration [33]

Mass Moments of Inertia

After the completion of the structural design the mass moments of inertia (MMOI) can be calculating for the Fire-Eye system. The MMOI is dependent on the distribution of the masses throughout the system as well as the masses of individual components.

Multiple assumptions were made in the calculation of the mass moment of inertia to simplify the calculations while limiting the impact on the accuracy of the results. It was assumed that all components have a uniform density, resulting in the center of gravity of each component being located at the centroid. Furthermore not all hub components were used in the determination of the center of gravity, as the contribution was deemed small and therefore had a minimal impact. Components such as the navigation and forensic camera, UV lights, and TOF sensors are neglected as their weight is below 10 grams, whereas the battery is the heaviest component within the hub at over 1 kg. Furthermore it is likely that the distance of these components to the center of gravity of the system is small, further decreasing the contribution to the center of gravity and mass moment of inertia.

To calculate the center of gravity of the Fire-Eye system a datum must be chosen from which all distances are defined, as well as a coordinate system. The coordinate system used is the body reference frame as shown in Figure 8.4, the z axis datum was chosen to be the top of the hub with the downwards direction being positive as dictated by the coordinate system. The x and y datum are defined as the centroid of the hub in the $x - y$ plane, a visual representation is shown in Figure 8.5. This results in all distances of components and the distance of the center of gravity are measured form the datum. To calculate the center of gravity Equation 8.1 is used. The distance x_i denotes the distance from the center of gravity of component i to the datum. The resulting location of the center of gravity is $(\bar{x}, \bar{y}, \bar{z},) = (-0.014, 0.002, 0.039)$ m. A sanity check confirms that the location of the center of gravity is reasonable as the center of gravity is slightly shifted aft towards the battery as well as the longer propeller arms. Furthermore, as intended, the y location is almost inline with the datum however the slight shift of the LiDAR sensor and the TOF sensor cause a rightwards shift. Lastly the z location is approximately in the center of the main hub component, which is the same height at which the propeller arms and motors are mounted.

$$\bar{x} = \frac{\sum x_i m_i}{\sum m_i} \tag{8.1}$$

After the determination of the center of gravity the mass moment of inertia can be calculated about the center of gravity of the quadcopter, the assumptions made for the determination of the center of gravity are again applied to the determination of the MMOI. Furthermore all components are considered cuboid in shape, this is true for all components that are taken into account for the MMOI

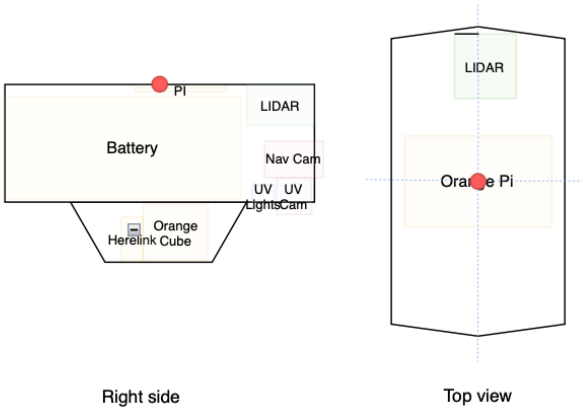

Figure 8.5: Visual representation of the datum, the red dot denotes the location of the datum

calculation. To calculate the MMOI of an object, with uniform density, about its own center of gravity Equation 8.2 is used, where l is the length and h is the height of the object. The parallel axis theorem can be computed using Equation 8.3, where x is the distance about which the parallel axis theorem is computed. The contributions are summed to find the total mass moment of inertia about an arbitrary point $I_{xx} = I_w + I'_{xx}$.

$$I_w = \frac{1}{12} m(l^2 + h^2) \tag{8.2}$$

$$I'_{xx} = mx^2 \tag{8.3}$$

The calculated mass moments of inertia are summarized in Table 8.2. It can be seen that the asymmetric MMOIs are two orders of magnitude smaller than the symmetric MMOIs, this indicates that the mass throughout the quadcopter is approximately symmetrically distributed throughout all three planes with respect to the center of gravity. This is an advantage of the 'X' configuration as the equal length arms make a double symmetric drone more likely when compared to a 'K' configuration. Having product moments of inertia close to zero has advantages for stability and control, the equations of motions are simplified and motions become decoupled [34].

Table 8.2: Total Mass Moment of Inertia about the Center of Gravity

Component	Value [kgm^2]
I_{xx}	0.022074
I_{yy}	0.017970
I_{zz}	0.033616
I_{xy}	0.000126
I_{xz}	-0.000296
I_{yz}	0.000199

Stability

The analysis of the system's stability starts with the evaluation of its stability in hover. This analysis is based on a free body diagram (FBD) of a simplified representation of the system as shown in Figure A.4. In Figure A.4 the body-fixed reference frame xyz is defined. This reference frame is useful for describing the motion of the object itself, because it simplifies the calculations related to the object's rotation.

The mass and the control forces of the propellers are presented as point loads, W, F_1, F_2,F_3 and F_4 respectively. The resulting moments of the propeller torque are presented by M_1, M_2,M_3 and M_4. l_r is the length of each arm, and l_h is the height of the propeller with respect to the center of gravity (CG).

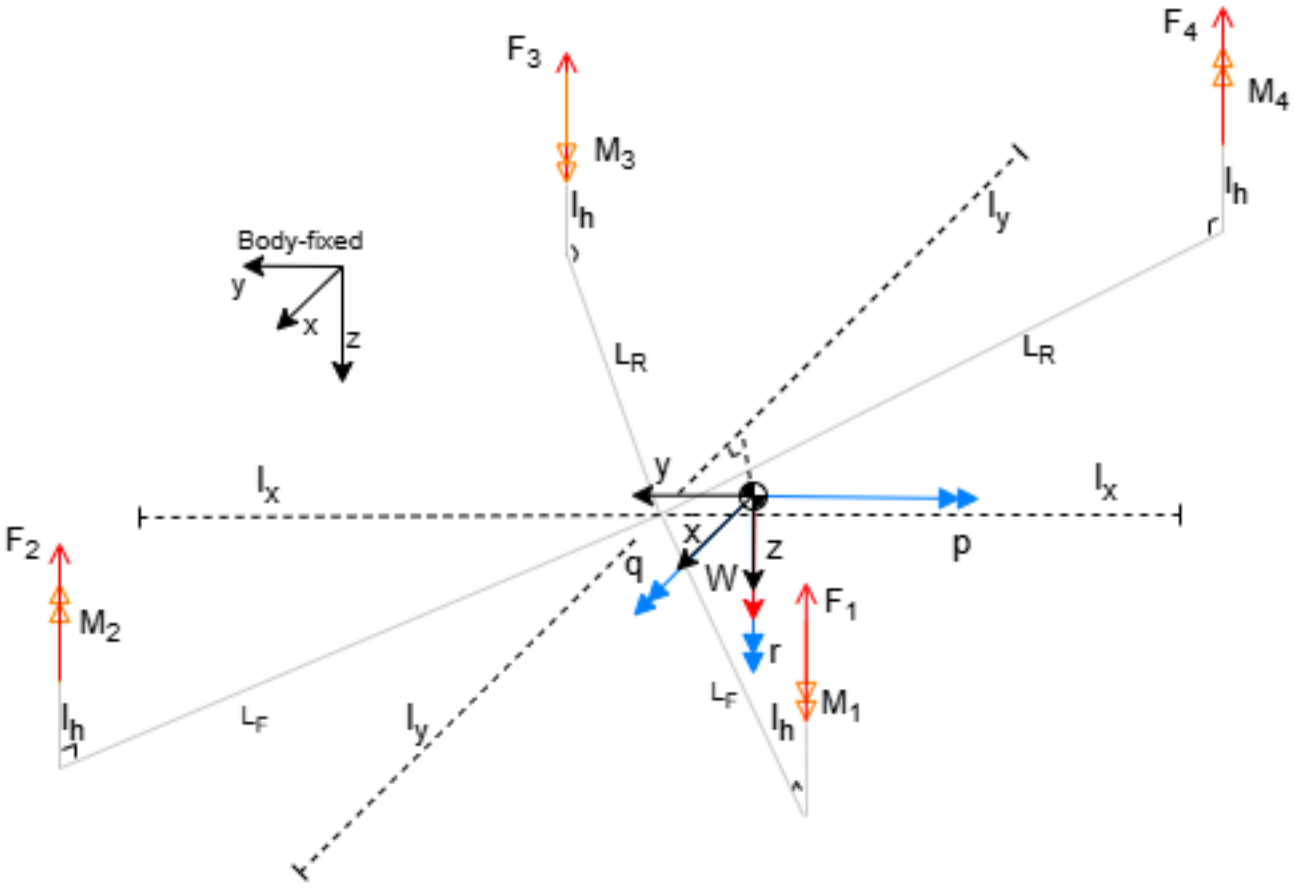

Figure 8.6: FBD of the Fire-Eye modular quadcopter in hover

The stability of the quadcopter in hover depends on the precise balance of force and moment, where a sum of forces and moments equal to zero in each direction is required to maintain both position and attitude. This balance requires accurate control of the thrust provided by each of the motors, as minor disturbances can disrupt this balance, potentially causing uncontrolled behavior. The thrust of each propeller can be managed by controlling the revolutions per minute (RPM), which will be controlled by the flight controller software as will be explained in the next section.

Model Description

As previously stated, control system for the Fire-Eye quadcopter is designed as a cascaded PID controller. It is structured into three hierarchical levels to achieve smooth tracking with fast disturbance rejection. This architecture allows for effective and stable control in confined environments. The control architecture is shown in Figure 8.7. It should be noted that the inputs and outputs in the blocks shown are of less relevance, as this figure serves purely to illustrate the overall architecture of the controller. The inputs and outputs of each block are discussed in the remainder of this section.

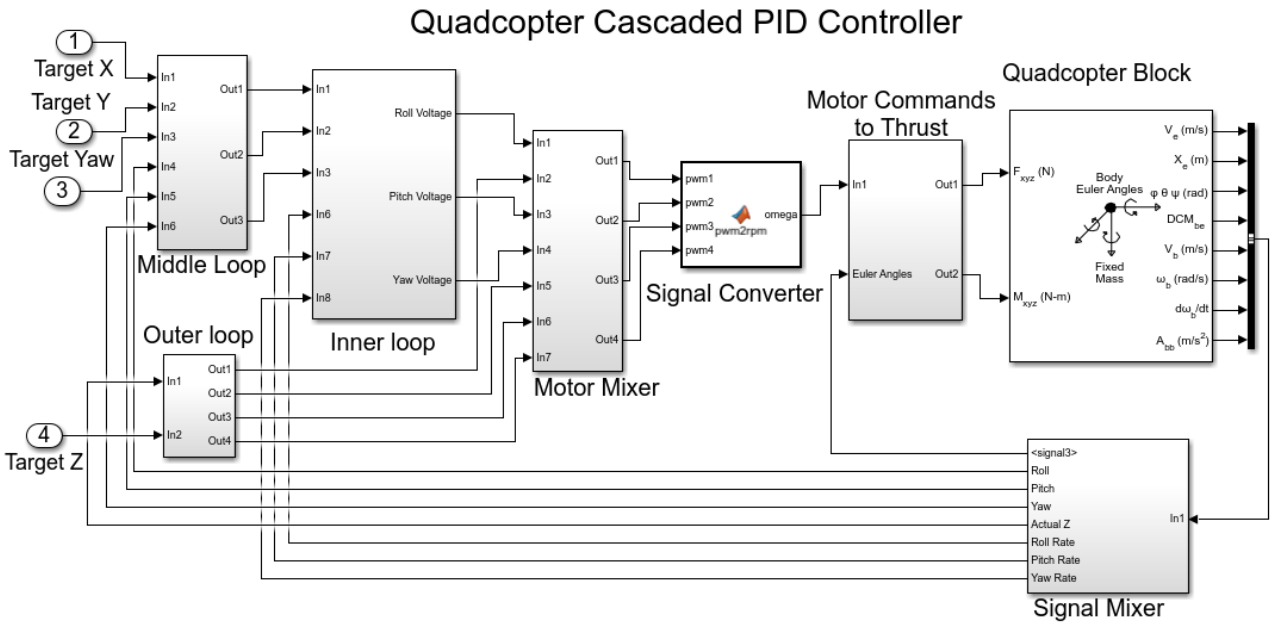

Figure 8.7: Fire-Eye control block

The inner loop handles the angular rates roll rate ($\dot{\phi}$), pitch rate ($\dot{\theta}$), and yaw rate($\dot{\psi}$). These states respond quickly to the control inputs due to the low moments of inertia of the quadcopter as explained in Figure 8.2. This loop is responsible for stabilizing and damping the system and ensuring that desired angular velocities are tracked accurately. The inner most loop works at he highest control frequency and is therefore typically faster than the outer loops. Because of this it can quickly correct for disturbances and maintain attitude stability before disturbances propagate to the outer loops.

The middle loop regulates the attitude angles roll (ϕ), pitch (θ), and yaw (ψ). This loop is required to ensure that the quadcopter can orient itself and maintain a certain attitude. It operates at a lower time scale than the inner most loop, but can command the inner loop via the error between the desired angles and the actual orientation.

Finally, the outermost loop consists of the altitude controller, which governs vertical position. This operates on the slowest time scale, as vertical translational motion is limited by the vehicle's total thrust capacity and inertia. The altitude controller produces a thrust baseline (PWM offset), which is then modulated by the roll, pitch, and yaw controllers to complete the control.

The cascaded PID loop structure shown in Figure 8.8 directly reflects the hierarchical control strategy of the system. At the outermost level, the altitude controller computes a thrust setpoint, which is then combined with a constant bias before being passed through a saturation block. This saturation block limits the output of the altitude controller, ensuring that the resulting signal stays within the voltage limits of the motors.

The constant bias plays an important role in the control architecture. It establishes a baseline voltage level that corresponds to a steady hovering state, which is therefore defined as the system's default behavior in the absence of other control inputs. This bias ensures that the quadcopter can maintain lift without requiring continuous corrective input from the altitude controller, thereby enabling more stable and predictable control. In addition, the bias helps the integral component of the PID controller to function effectively from the start. Because the integral term accumulates error over time, providing an initial offset allows it to begin correcting any deviation immediately. Without this, the controller would need to wait for error accumulation before producing a meaningful response, potentially resulting in unnecessary delay in altitude response.

Finally, the use of a voltage budget across all control loops ensures that no single PID controller dominates the motor outputs. This is especially important during multi-axis maneuvers, where simultaneous control actions must be blended through the motor mixer. The voltage budget, enforced

by the saturation blocks and baseline offset, ensures that all PID control blocks are recognised by the system's motor systems and can correct error terms timely. Ignoring these voltage budgets could otherwise destabilize the system.

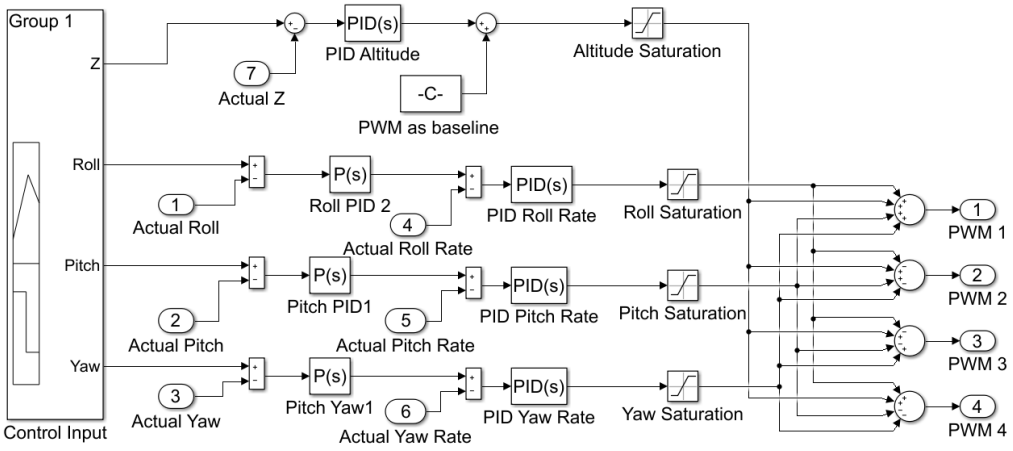

Figure 8.8: Cascaded PID control architecture

The outputs of these PID controllers are control voltages. They result from errors in the attitude, positioning or accelerations of the quadcopter. These signals are sent to the motor mixer, which combines them into PWM signals for each of the four motors. These PWM signals are the outputs of the flight controller that are used to command the ESCs of the motors, which will output a certain torque of the motors. The mixer uses a predefined allocation matrix to distribute the thrust and torque demands across the motors. The mixer ensures that the correct motors increase their thrust to achieve a certain maneuver. For example, the front two motors (1 & 2 as per convention) should be spinning at a higher RPM. The PWM signals pass a saturation filter to ensure that the voltages do not exceed the maximum voltage the motors can deliver. Following this, the signal converter block maps these voltages to individual rotational speeds (RPM) using a calibrated motor model. This model accounts for characteristics such as motor constants and calculates the required motor specific RPM outputs using the following equation;

$$\text{RPM} = K_v \cdot U \tag{8.4}$$

K_v is the motors' KV rating. It is a constant that states the RPM of the motor per volt provide. U is the voltage (V) provide to the motor. The resulting motor speeds are then used by the motor command function to calculate the individual thrusts and torques generated by each propeller. These are determined using relationships defined in Equation 8.5. Where ρ is the air density in kg/m^3, D is the diameter of the propeller and C_t and C_q are the aerodynamic coefficients of the propeller for thrust and torque respectively. Based on the combination of these individual motor outputs the resulting forces in the body-fixed reference system are computed. The computations are performed using the FBD shown in Figure A.4.

$$\begin{aligned} T &= \rho D^4 C_t \frac{\text{RPM}^2}{3600} \\ Q &= \rho D^5 C_q \frac{\text{RPM}^2}{3600} \end{aligned} \tag{8.5}$$

The force and moment vectors are then fed into the Aerospace 6DOF quadcopter block from MATLAB's Aerospace Blockset[13], which simulates the rigid-body dynamics of the quadcopter. This block transforms the input forces and torques in the body-fixed frame into changes in attitude, angular velocity, linear velocity and position in the earth-fixed (inertial) frame. It integrates the equations of motion to update the system's physical state over time. The outputs of the Aerospace block represent the actual states of the quadcopter. These values are then compared to the reference commands

[13]URL: https://nl.mathworks.com/help/aeroblks/6dofeulerangles.html [Cited 18/06/2025]

provided to the system, and the differences (errors) are used as input to the PID controllers. This feedback mechanism closes the control loop, allowing the quadcopter to continuously correct its behavior and follow desired trajectories when the PID controllers are tuned accordingly.

For the Fire-Eye quadcopter, tuning is performed in a structured order that aligns with the control loop hierarchy. First, the PID controller for altitude control is tuned to achieve stable vertical motion and hovering state. At the current stage of development only the altitude controller has been tuned. In future development of the Fire-Eye control system the inner loop controlling the angular rates will be tuned. In future development of the Fire-Eye control system the inner loop controlling the angular rates will be tuned along with the middle loop controlling the angles or attitudes. This will ensure that in the future the quadcopter can quickly and accurately respond to changes in desired attitude and that the desired orientations are followed smoothly and precisely. During the tuning of individual PID control blocks, the gains of other blocks are set to zero or ignored to prevent the outputs interfering. This sequential approach ensures stability and proper interaction between nested control loops.

Controller specifications

The PID gains that were used to tune the flight controller of the Fire-Eye quadcopter were obtained using a combination of the auto-tune function of MATLAB Simulink and manual tuning. The gains for each PID component and the filter coefficient are displayed in Table 8.3 below; Control Gains

Table 8.3: PID Controller Gains and Derivative Filter Coefficients

Controller	P	I	D	N
Altitude (Z)	-3.049	-0.725	-3.009	450
Roll Rate	0.700	0.500	0.080	17.20
Pitch Rate	0.700	0.600	0.020	36.47
Yaw Rate	3.164	6.052	-0.067	17.20
Roll Angle	8.000	—	—	—
Pitch Angle	6.919	—	—	—
Yaw Angle	5.340	—	—	—

The altitude controller (Z) utilizes a full PID structure with relatively large negative gains. The negative gains reflect the body-fixed reference frame where a positive Z indicates a downwards orientation with respect to its flight path. A desired decrease in altitude results in a positive error (target - current altitude), but the motors have to decrease their thrust and therefore require a negative control output. The gains are moderate to high, indicating an aggressive but damped response to vertical deviations.

The rate controllers for roll, pitch, and yaw are tuned with relatively low gain values, ensuring stability and smooth response. The angle controllers (roll, pitch, yaw) are purely proportional. This was chosen following PX4's standard cascaded control architecture [14]. The proportional term proved to be enough to obtain a desirable response of the system and therefore the integral and derivative terms were left out. For these proportional terms high gains were used to ensure a fast response to attitude changes.

The Fire-Eye system uses motors that have a voltage limit of 16V. Because of this a voltage budget had to be defined to ensure that the system would be able to perform maneuvers simultaneously and that the motor outputs would not be completely dominated by the output of a single PID control block. The budgets for each control loop are summarized in Table 8.4 below;

8.3. Verification & Validation

To ensure the correctness of the CG and inertia calculations, a series of sanity checks were performed. The Python code used was verified by comparing its outputs with results from calculations performed by hand. This process confirmed that the code performed as expected under controlled, test-case conditions. Full validation of the CG and inertia values is not yet possible, as this requires either the availability of detailed 3D CAD models or the initiation of the production phase, during which physical measurements can be performed.

[14] URL:https://docs.px4.io/main/en/flight_stack/controller_diagrams.html [Cited 24/06/2025]

Component	Voltage Allowance (V)
Max Allowed Voltage	16.0
Z PID (Hover Voltage)	±10.0
Roll Allowance	±2.5
Pitch Allowance	±2.5
Yaw Allowance	±1.0

Table 8.4: Voltage Budget Allocation for Quadcopter Controller

The flight controller was implemented using the 6DOF Aerospace Blockset provided by MATLAB. Given that this blockset is developed and maintained by MathWorks, it is reasonable to assume the underlying logic is already verified and validated by MathWorks.

The remaining control logic was verified by starting with a single block added to the 6DOF Aerospace Blockset and then constructing up the model to the complete hierarchical control system. For each step the verification was performed by introducing dummy input variables and plotting the block outputs and responses of the system. These plots were visually inspected to assess whether the behavior matched expectations. Where applicable, the system's behavior was also compared against results derived from hand calculations.

In addition to this block-wise functional verification, the controller's robustness was further evaluated under motor failure scenarios. Specifically, two diagonally opposite motors were disabled to simulate a two-motor failure. The system's response confirmed that the hierarchical control architecture was capable of isolating and tolerating partial thrust loss, while maintaining basic stabilization in the remaining axes.

The validation process focused on the system's dynamic response to changes in the reference input. For instance, the system was tuned using a step response in the Z-direction (altitude). However, for validation a constant was used as a reference input. The resulting response was stable and converged to the desired reference value, demonstrating that the controller is capable of achieving and maintaining a stable hover for inputs it has not been tuned for, validating the altitude control loop.

Broader validation of the control system was conducted through simulation using two input scenarios: sequential axis excitation and simultaneous roll-pitch-yaw commands, as shown in Figure 8.9 and Figure 8.10, respectively. These tests aimed to assess the individual behavior and decoupling performance of the controllers under isolated conditions.

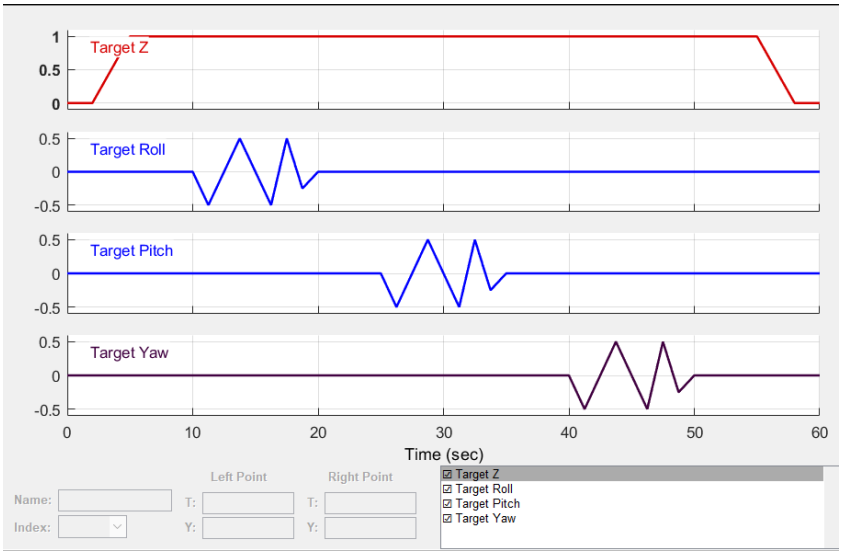

Figure 8.9: Sequential Axis Excitation Reference Input

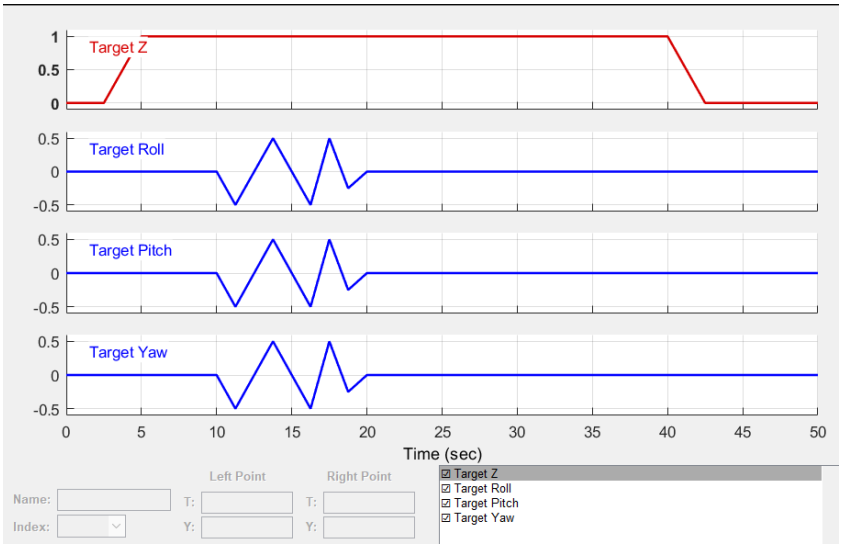

Figure 8.10: Simultaneous Roll-Yaw-Pitch Reference Input

During sequential excitation, the controller tracked each reference input effectively, maintaining altitude and showing minimal overshoot and steady-state error (see Figure 8.11). Under simultaneous excitation, the roll, pitch, and yaw responses remained stable but revealed increased interaction effects. The pitch and roll axes showed slightly more overshoot compared to the isolated-input tests, suggesting that cross-coupling dynamics became more pronounced. The yaw response remained relatively well-behaved, although with minor deviations from the reference signal during periods of high activity in the pitch and roll axes. Altitude control was indirectly affected due to aerodynamic coupling, leading to subtle drifts in altitude even though no new reference changes were applied in the vertical direction (see Figure 8.12).

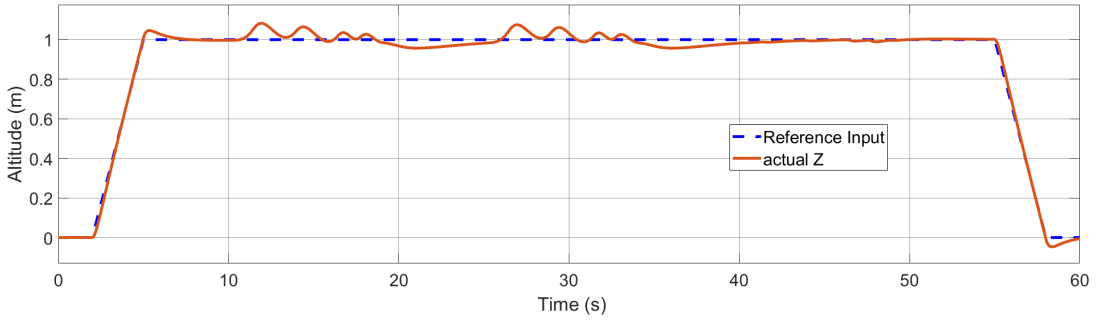

(a) Z axis response

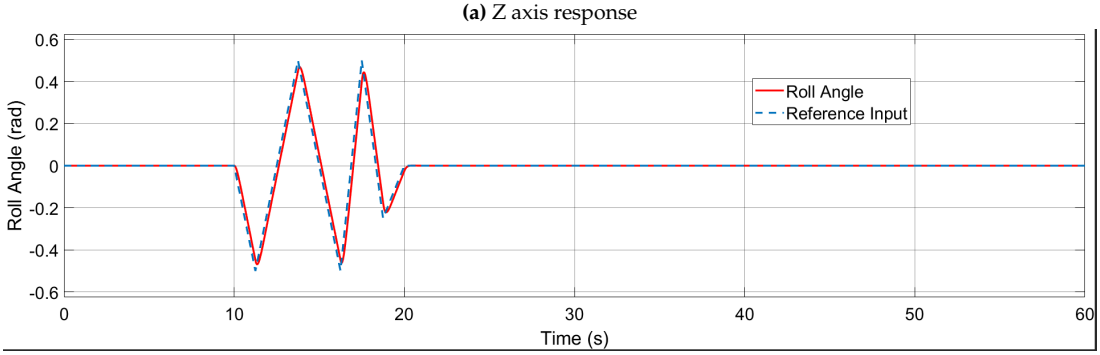

(b) Roll response

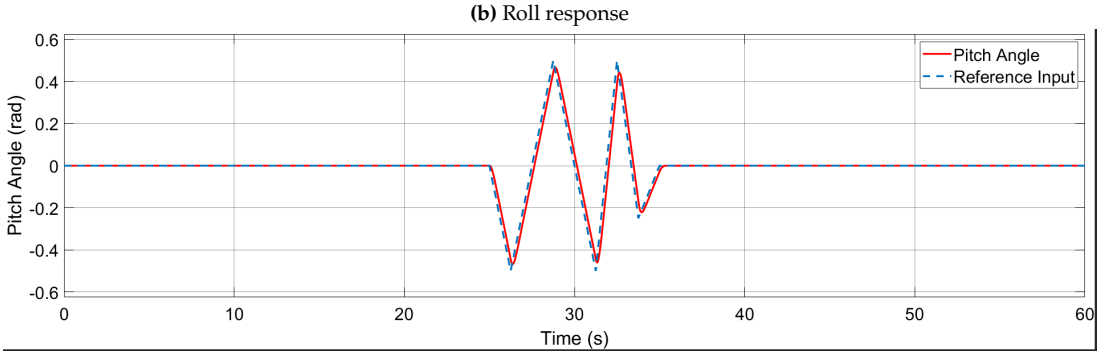

(c) Pitch response

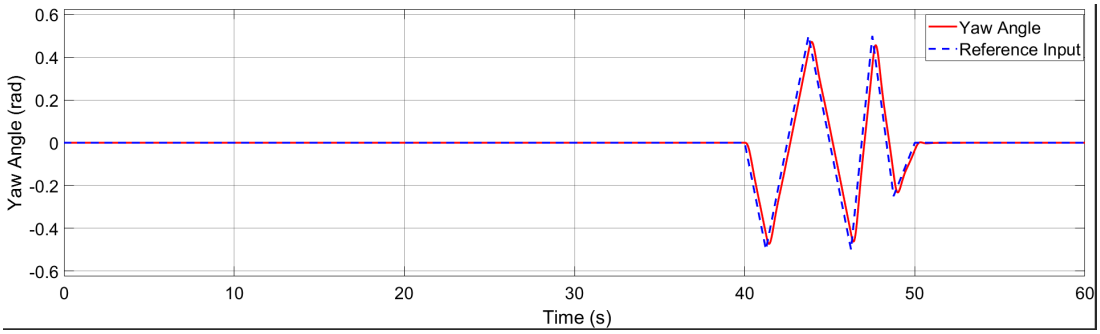

(d) Yaw response

Figure 8.11: Sequential Axis Excitation Results

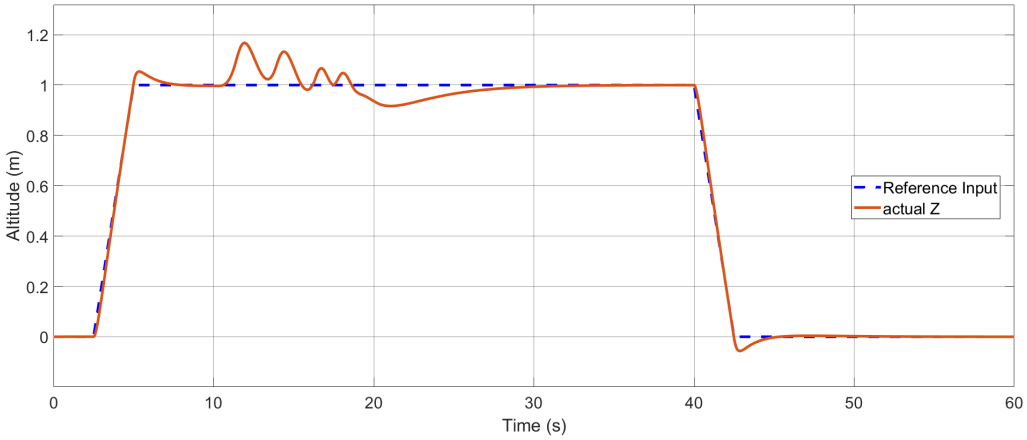

(a) Z axis response

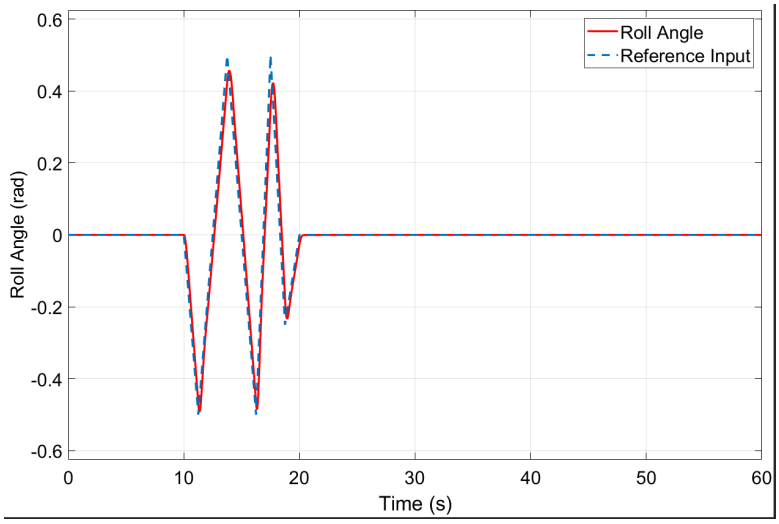

(b) Roll response

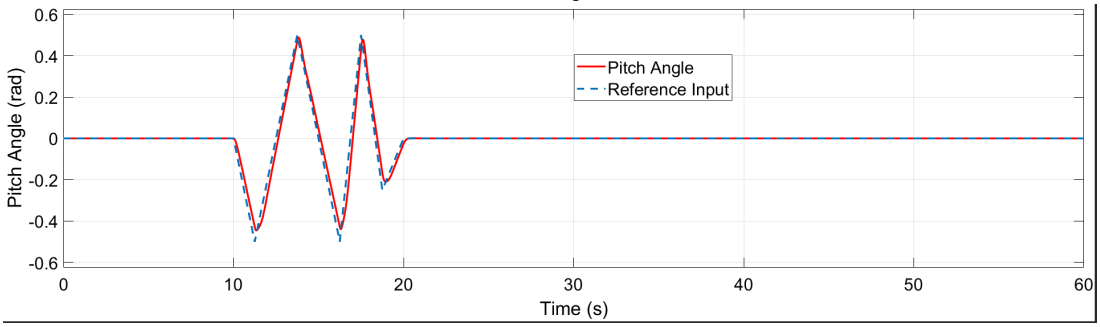

(c) Pitch response

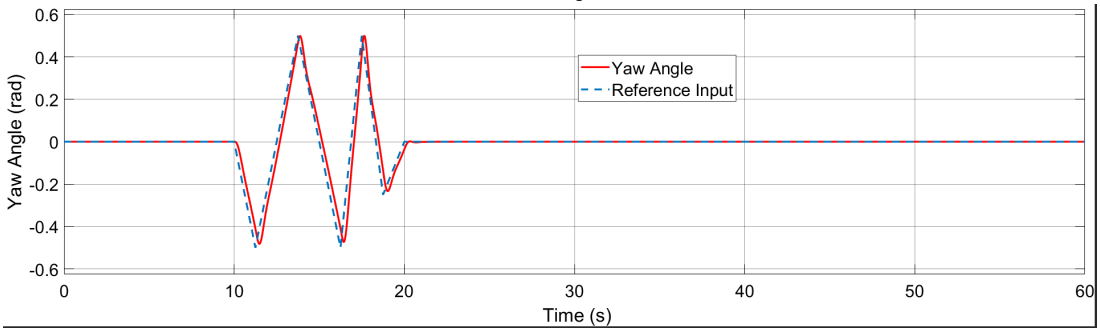

(d) Yaw response

Figure 8.12: Simultaneous Roll-Yaw-Pitch Results

Despite these issues, the system completed multi-axis maneuvers without catastrophic instability, validating the hierarchical cascaded PID structure in simulation. The system demonstrated adequate stability, responsiveness and robustness across a range of realistic flight scenarios.

8.4. Discussion

First and foremost, when the control axes were excited on their own, the PID loops shows sufficient capability to follow the references with acceptable overshoot and steady-state performance. However, when multiple axes were excited at the same time, some issues do arise.

The most obvious limitation of the system is that of the axis decoupling. In reality, especially for agile maneuvers, the interaction between the axes cannot be neglected. As of now, the PID controller lacks cross-axis compensation, which leads to poor performance when multiple axes are disturbed simultaneously.

In addition, the controller does not take external disturbances of modeling inaccuracies, such as unmodeled dynamics, delay or actuator limitations, into account. This further enforces the point that while the controller performs well under controlled simulation conditions, it will likely require further enhancements such as dynamic decoupling, feedforward compensation or a multivariable control approach, in order to be implemented into real world scenarios.

Furthermore, even though the controller exhibits solid angular tracking performance, there is no translational control in the X and Y axes. This causes the system to drift in the lateral or longitudinal direction, given any roll or pitch input. This is caused by the lack of a restoring force or velocity-damping solution in the horizontal plane. As a consequence, once the system has been displaced by a maneuver, it will continue to accelerate in given direction.

The solution to this would be to have dedicated, tuned, X and Y position control loops. This venture is believed to be promising, as the current controller demonstrates a smooth response to angular commands. This would suggest that the system is equally equipped to manage X and Y motion with precision, if properly implemented.

However, due to the limitations mentioned, it cannot be said that the controller can guarantee safe operation in constrained environments. Most importantly, the residual oscillations caused by yaw or pitch suggests that the system might struggle to pass trough narrow openings of 70 cm x 70 cm, considering there is only 2 cm of leeway. Additionally, the overshoot and altitude deviations seem during more aggressive maneuvers could compromise clearance margins. In order to ensure safe and efficient operation, further tuning of the controller is necessary.

8.5. Sensitivity Analysis

A sensitivity analysis was carried out to evaluate the robustness of the flight control system to variations in key physical parameters. The thrust and torque coefficients, and the quadcopter's total mass were adjusted by ±10% to assess the effect on closed-loop stability and tracking performance.

When the thrust and torque coefficients were reduced by 10%, the controller remained capable of maintaining hover, however, significant altitude oscillations were observed when performing roll and pitch maneuvers. This behavior is likely due to the limited voltage margin imposed by the motor characteristics and the saturation limits within the control logic. With a lower thrust coefficient, maintaining vertical stability requires increased control effort, which can cause the PID output to be limited by voltage budget constraints. This leads to a limit cycle or an underdamped response in the vertical axis. These results suggest that under such conditions, roll and pitch maneuvers must be executed separately to maintain vertical control authority, or that motors or controller gains must be re-tuned to accommodate reduced thrust authority.

In contrast, a 10% increase in thrust and torque coefficients improved the response of the system. The quadcopter maintained both attitude and altitude more effectively, and no issues related to instability or saturation were observed during maneuvers.

When the quadcopter's total mass was adjusted by ±10%, the controller maintained reliable altitude and attitude tracking. The gains showed sufficient robustness to handle moderate changes in inertial and gravitational loading, without significant performance degradation. These results show that the

system is generally robust to modest parameter variations, though it becomes more sensitive when thrust and torque coefficients are reduced.

9 - Downwash

The most important limitation affecting the design is the minimal scene disturbance. When conducting forensic investigations, it is crucial that the scene should remain as complete as possible in order to not taint evidence. The aspect of the system that is most likely to disturb the scene is the downwash created by the propulsion system. Downwash refers to the air that is pushed through the propeller to generate thrust. This creates a cone of airflow that has the potential to move evidence, including dust and other particles that might interfere with the mission or the investigation. It is therefore necessary to find ways to calculate this effect, and to find ways to minimize it. In this analysis, downwash shall be quantified as the axial induced velocity at the ground when flying at a certain altitude. The relevant requirements for downwash are shown in Table 9.1. As can be seen, **REQ-STK09-PROP06** and **REQ-STK09-PROP07** do not have relevant values as of right now. This is because the calculations necessary to find realistic values are not yet conducted. More on this can be read in Section 9.3.

Table 9.1: Relevant requirements for downwash

ID	Requirement
REQ-STK10	The system shall not damage forensic evidence.
REQ-STK09-PROP06	The system shall not displace objects or debris heavier than <TBD>grams from their point of origin.
REQ-STK09-PROP07	The system shall not displace objects or debris more than <TBD>meters from its point of origin.
REQ-STK10-PROP08	The system shall not produce more than 1.5m/s downwash at the ground

This chapter will start describing different methods that can be used to find the downwash in Section 9.1. Then, the results of the methods will be shown in Section 9.2. After, the limitations of the model used will be discussed and recommendations will be given as to how to improve the model, and what calculations should be conducted after, to quantify the downwash in a more relevant way. This will be done in Section 9.3. Following this, the verification process for the method used will be illustrated in Section 9.4. Then, the results generated can be fully discussed in Section 9.5. Following the discussion, recommendations will be given as to how to proceed with downwash minimization in Section 9.6. Finally, the whole chapter will be briefly summarized in Section 9.7.

9.1. Methods of Determining Downwash

The downwash of any given system can be determined using different methods. Often, experimental data is used, since modeling airflow can be very complex and computationally intensive. Alternatively, models can be made to approximate the downwash, which was used in this project.

Downwash Calculation Based on Weight and Thrust

The simplest way to calculate the downwash speed is to relate the weight that needs to be pushed up to the amount of air that needs to be pushed down. The formula for this can be seen in Equation 9.1.

$$V_1 = \sqrt{\frac{\frac{1}{4}mg}{2\rho A}} \tag{9.1}$$

In this formula, m is the mass in kilograms, g the gravitational constant in m/s^2, ρ the density in kg/m^3 and A the area covered by the propeller in m^2. The $\frac{1}{4}$ factor is added to account for the fact that each propeller needs to carry one fourth of the total weight of the system. Similarly, the downwash

can be calculated based on the thrust of the system. Where the formula used to find the thrust can be seen in Equation 9.2.

$$T = C_T \rho n^2 D_p^4 \tag{9.2}$$

Where C_T is the thrust coefficient. This can then be plugged into Equation 9.1 instead of the total mass. In addition to these formulas, this method makes the assumption that the highest speed is not reached at the propeller. Rather, it is approximated to occur at a distance of three propeller diameters from the propeller. A tube of airflow is assumed, that becomes more narrow at this location, therefore increasing the speed. The speed at this location is approximated to be twice the speed at the propeller. Furthermore, the method assumes the air is not effected by the propeller at a distance of about ten diameters from the propeller. An illustration can be seen in Figure 9.1.

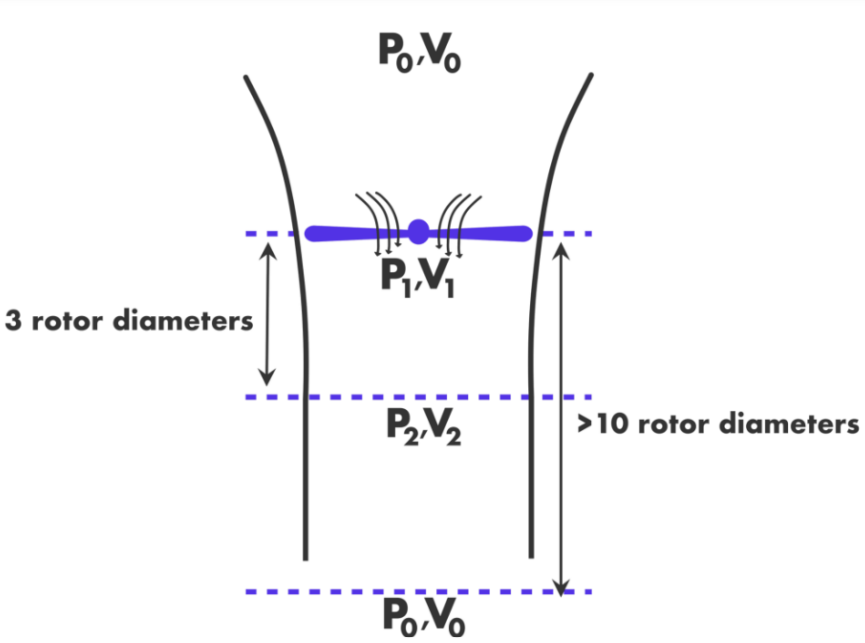

Figure 9.1: Downwash tube created by a propeller.
1

There are some substantial limitations to this method. Firstly, this method is used to calculate downwash for a helicopter with one propeller. The resulting downwash created is much higher than what would be created by the Fire-Eye, which could result in discrepancies. Secondly, this method only gives the airspeed at three locations. It is therefore not possible to determine at any given location, as the relations between the points is unknown. This means that the speed at the ground cannot be determined, unless the system flies at a distance three or over ten diameters from the ground. Thirdly, there is no variance in the velocity along the radius of the propeller. The radial location of the maximum velocity can therefore not be determined. Finally, the size of the cone is unknown. This method is thus unable to determine the effected area of the downwash.

Computational Fluid Dynamics

On the other end of the spectrum there are Computational Fluid Dynamics (CFD) models. These are capable of computing highly complex flows and are generally considered to be the best way to approximate actual airflows. CFD however, is very computationally intensive and notoriously difficult to use. It was determined to not be feasible in this design project, given the limited time available and the lack of expertise within the team.

Semi-Empirical Methods

For a simpler and less accurate method one can make use of semi-empirical methods to roughly determine the speed of the air once it gets displaced by the propeller. These are very common and

extensively researched within the field of marine propellers [35][36].For propellers in air this is not yet the case. However, the same method that is used to determine the formula's for the marine cases can be used for air propellers as well using coefficients that take into account the difference in viscocities and densities of water and air.

First, it is important to touch on the different flow regiments that are used to determine these formulas in the case of underwater propellers. Marine theory defines two zones of importance. Namely, the Zone of Flow Establishment (ZFE) and the Zone of Established Flow (ZEF). As the name suggests, the ZFE deals with the airflow before it has been fully established. This zone is characterized by having two peaks of maximal induced velocity, when considering both sides of the propeller. Throughout the zone, the two peaks will slowly move towards each other until they eventually merge. This marks the end of the ZFE, and the start of the ZEF. Within the ZFE, two zones are identified to account for the change in flow deceleration. This results in three different semi-empirical formula's. An illustration of the flow profile for one side of the propeller is shown in Figure 9.2.

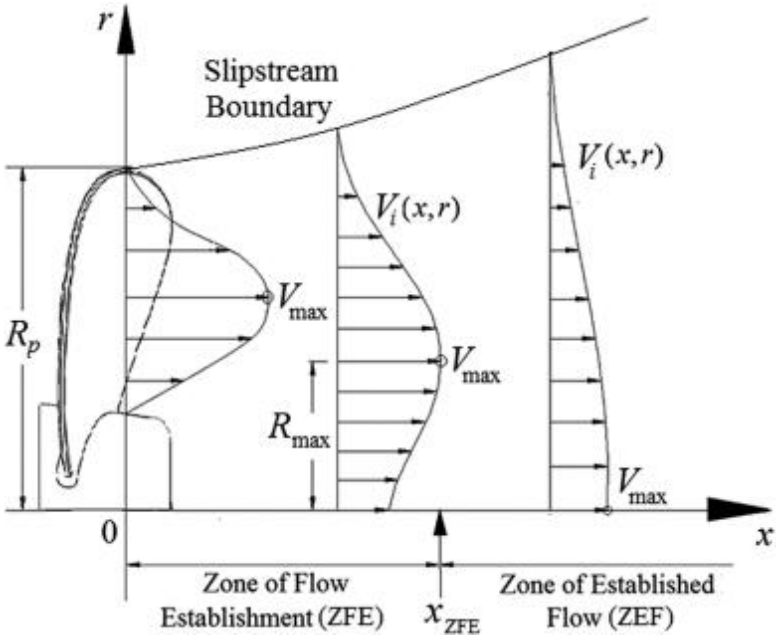

Figure 9.2: Diagram of the flow profile for a marine propeller [2]

Air however, differs substantially from water, and so do marine and aircraft propellers. Firstly, another flow regiment is identified. Before the flow reaches the ZFE, it is in what is referred to as the near-field region. This region is not present for marine propellers, due to the lower rpm and induced velocity. In this zone, the flow contracts and the speed increases accordingly. This is due to the fact that the dominant effect in the near-field region is acceleration. Due to the propeller accelerating the flow, the flow will contract due to Bernoulli's principle. At some point the flow will reach a maximum velocity and contraction at a axial distance from the propeller known as the efflux plane. After this, the far-field region starts, which consists of the previously mentioned ZFE and ZEF. In this region, the flow velocity will not increase any further [2]. An illustration including these new parts of the flow can be seen in Figure 9.3

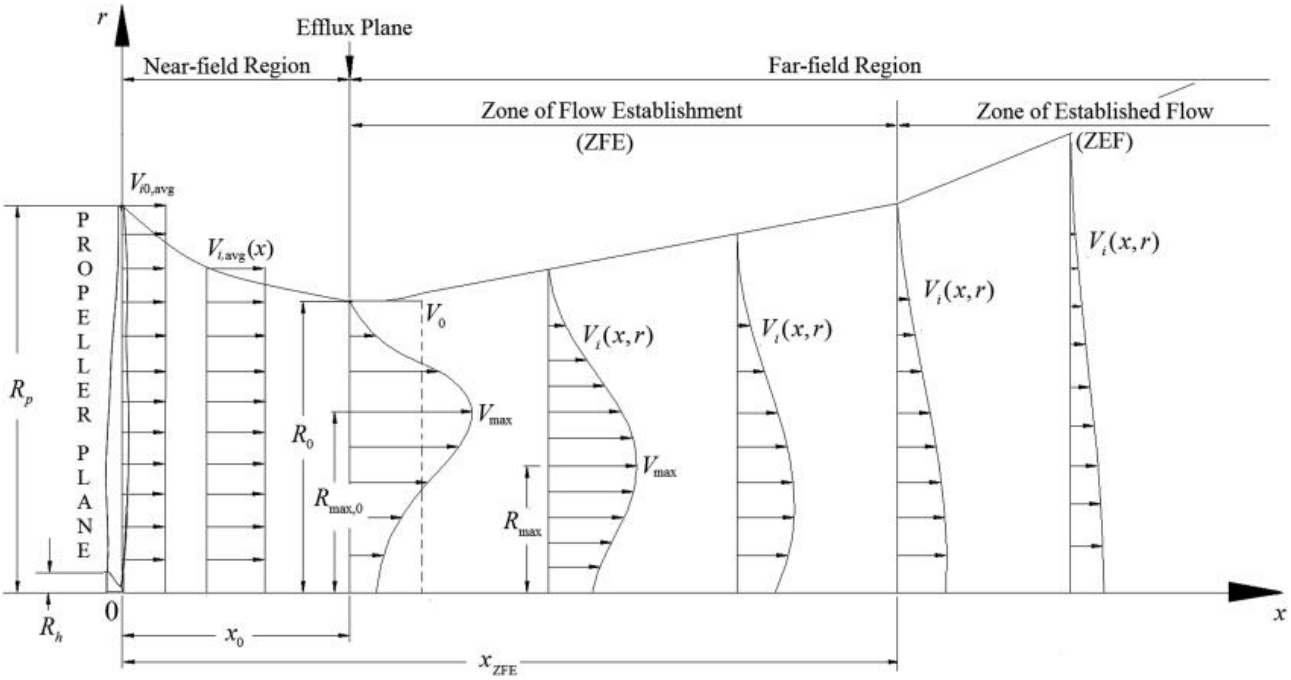

Figure 9.3: Diagram of the flow profile for an aircraft propeller [2]

To find the maximum velocity, use is made of momentum theory. This approximation is made since the effect of diffusion can be neglected in the near-field region, and therefore momentum theory generally holds. This results in Equation 9.3

$$V_0 = 1.59 n D_p \sqrt{C_T} \tag{9.3}$$

Where V_0 is the efflux velocity in m/s, n the rotor speed in rev/s, D_p the diameter of the rotor in m and C_T the thrust coefficient of the propeller. Then, we can use momentum theory to find the radius of the tube and axial distance from the propeller plane at the efflux plane can be found. It should be noted however, that in research conducted for marine propellers it was found that this maximum velocity is lower than predicted because of the influence of diffusion. It is therefore generally accepted that the coefficient of 1.59 is lower in reality and can be found through experimentation.

In order to find the semi-empirical formulas for the far field region, a general method has been devised by marine researchers. They first find formulas to find the maximum induced velocity and its radial position with axial distance, using the efflux velocity, and propeller diameter. Then, the induced velocity profile is approximated using a Gaussian function, using both the axial and radial distance. For the aircraft propeller the same method is used, due to the difference in flow characteristics the coefficients will be different but the same theory should still hold. It is important to note that the formula for maximum velocity for aircraft propellers assumes that the propeller diameter used in the formulas is not the actual propeller diameter. Rather, it is the diameter of the flow at the efflux plane. Similarly, the axial distance is measured starting from the efflux plane, not at the actual propeller plane. This correction should be made because in the case of marine propellers, the efflux plane coincides with the propeller plane. Examples of V_{max} formulas for marine and aircraft propellers can be seen in Equation 9.4 and Equation 9.5 respectively.

$$V_{max}(x) = V_0 \left(a_1 - b_1 \frac{x}{D_p} \right) \tag{9.4}$$

$$V_{max}(x) = V_0 \left(a_1 - b_1 \frac{x - x_0}{D_0} \right) \tag{9.5}$$

, where V_0 is the average velocity at the efflux in m/s, x the axial distance from the propeller plane in m, x_0 the distance from the propeller plane to the efflux plane in m, D_p the propeller diameter in m and D_0 the diameter of the efflux plane in m. The coefficients a_1 and b_1 are determined through experimentation. Similarly, the radial location of the maximum velocity can be found using Equation 9.6.

$$R_{max}(x) = R_{max,0}\left(a_2 - b_2\frac{x - x_0}{D_0}\right) \tag{9.6}$$

Where $R_{max,0} = 0.67(R_0\text{-}R_h)$, which is found through the use of the momentum theory. R_0 is half of D_p and R_h is the hub radius of the propeller in m. These formulas have to be found for all three regions within the far-field region. After that has been achieved, the gaussian formula for the induced velocity as a function of both axial and radial distance can be found. An example of such a formula can be seen in Equation 9.7.

$$V_i(x,r) = V_{max}exp\left[-\left(\frac{r - R_{max}}{a_3R_{max,0} + b_3(x - x_0 - R_0}\right)^2\right] \tag{9.7}$$

Now that the formulas have been established, the coefficients must be determined. Ideally, this would be done through extensive experimentation. Due to time and resource limitations however, the coefficients will be taken from [2]. In addition, this paper outlines the locations of the transitions from one region of flow to another. An extensive summary of all the formulas used including the coefficients can be found in Table 9.2.

Table 9.2: Summary of semi-empirical formulas used

Zone	**Formulas**
ZFE	$V_{max}(x) = V_0\left(1.24 - 0.00765\frac{x - x_0}{D_0}\right)$
$x_0 < x < (x_0 + 1.7D_0)$	$R_{max}(x) = R_{max,0}\left(1 - 0.1294\frac{x - x_0}{D_0}\right)$
	$V_i(x,r) = V_{max}exp\left[-\left(\frac{r - R_{max}}{0.8839R_{max,0} + 0.1326(x - x_0 - R_0)}\right)^2\right]$
ZFE	$V_{max}(x) = V_0\left(1.37 - 0.1529\frac{x - x_0}{D_0}\right)$
$(x_0 + 1.7D_0) < x < (x_0 + 4.25D_0)$	$R_{max}(x) = R_{max,0}\left(1.3 - 0.3059\frac{x - x_0}{D_0}\right)$
	$V_i(x,r) = V_{max}exp\left[-\left(\frac{r - R_{max}}{0.5176R_{max,0} + 0.2295(x - x_0 - R_0)}\right)^2\right]$
ZEF	$V_{max}(x) = V_0\left(0.89 - 0.04\frac{x - x_0}{D_0}\right)$
$x > (x_0 + 4.25D_0)$	$R_{max}(x) = 0$
	$V_i(x,r) = V_{max}exp\left[-\left(\frac{r}{0.2411(x - x_0)}\right)^2\right]$

9.2. Results

For this analysis, two cases were considered. Firstly, the induced velocity that will occur during hover, where the thrust was evaluated. Then the induced velocity at maximum thrust, which is equal to two times the weight of the system, was calculated as well. This was done using all three of the aforementioned methods, which include the simple formula using both the weight and total thrust as input and the outlined semi-empirical method. The input values for both cases can be seen in Table 9.3.

Table 9.3: Input parameters for both conditions considered

	Hover	Maximum Thrust
Thrust [N]	5.3	11.7
Thrust Coefficient [-]	0.063	0.058
RPM [-]	7700	12000
Diameter propeller [m]	0.254	0.254
Total system mass [kg]	2.08	4.16

The mass used for this analysis is from the heaviest configuration, to find the most critical values. The weight however, should not impact the results too much, as it is only relevant for the calculation of the induced velocity using the weight. Both the calculation based on thrust and the semi-empirical methods do not take into account the weight of the system at all. Furthermore, for the calculation based on weight for maximum thrust, it is assumed that the system needs to lift two times the weight, as per **REQ-STK01-MIS31-PROP04-EFF01**. The results for the velocity calculation based on weight and thrust using the most simple method presented will be shown at the end of the chapter in Table 9.4. First, the plots generated using the semi-empirical methods will be demonstrated.

Using the semi-empirical methods, velocity heat maps can be generated. These plots are plotted horizontally to mimic the paper being used [2]. In reality, the propeller shall be displacing air vertically downwards, meaning the plot shall be turned 90 degrees clockwise.

The flow starts at the left side of the plot, at the efflux plane. As mentioned in Section 9.1, the velocity profile between the propeller plane and the efflux plane is not shown. A black dotted line is plotted at a distance of 1.5 from the propeller plane, this represents the ground at the nominal altitude. The plots for the hover and maximum thrust conditions are shown in Figure 9.4 and Figure 9.5 respectively.

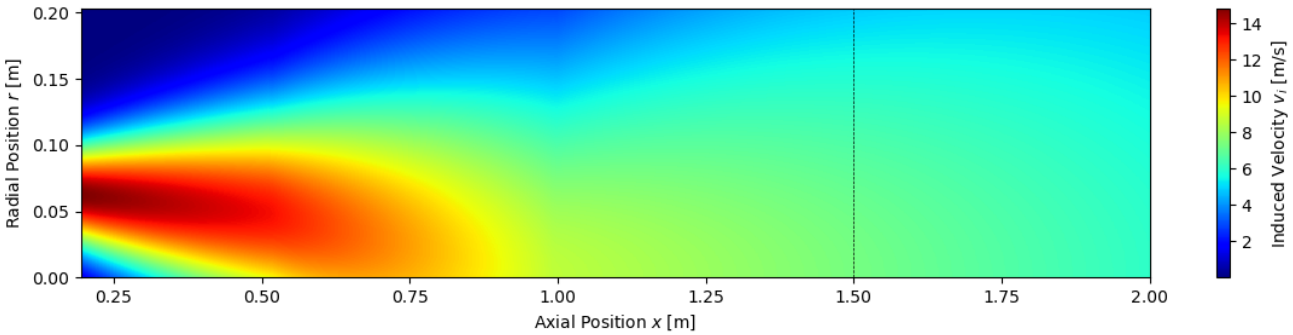

Figure 9.4: Induced velocity plot for hover

From Figure 9.4 it can be concluded that in the case of the hover, the maximum induced velocity starts of at a speed of about 15 m/s and slows down to about 6 m/s after 2 meters. The boundary start of being slightly smaller then the propeller diameter, which is in line with expectations. The flow first compresses as speed increases, and as maximum speed is reached it will expand and decelerate. The boundary continuously expands until the ZEF is reached at a distance of about one meter. Here, a kink in the flow occurs. After this kink, the flows continuous to expand.

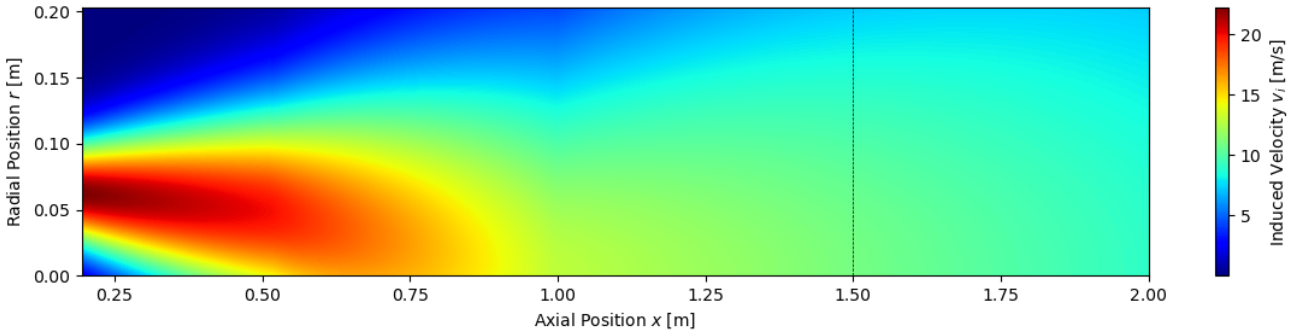

Figure 9.5: Induced velocity plot for maximum thrust

Figure 9.5 demonstrates similar behavior to Figure 9.4, save for the fact that the velocities are higher. The maximum induced velocity starts of at a speed of about 22 m/s, and slows down to a speed of about 10 m/s after two meters of travel.

When comparing both plots, it can be concluded that the shape of the plot is identical. The difference between the plots is only apparent in the range of velocities as can be seen in the legend on the right hand side of the plots. The appearance being the same is due to the method used. The only parameter that differs for both cases is the V_0 calculated. The distribution and deceleration rate is the exact same in both cases. In addition, the plots show a kink at around a distance of one meter from the propeller plane. This is the transition between the ZFE and the ZEF. The kink likely happens to due the fact that the semi-empirical method used is constructed using piece-wise functions that have small discontinuities. In reality, it is expected that this kink will be smoothed over as the diffusion is a continuous process.

From Figure 9.4 and Figure 9.5, it is difficult to read specific values at any given distance from the propeller plane. Since the main location of interest in the induced velocity profile at the ground, additional plots were generated for both cases. Figure 9.6 and Figure 9.7 show the profiles at a distance of 1.5 meters from the propeller plane. Both plots include a block dotted line at a velocity of 1.5 m/s, as this is the speed at which particles should not move anymore. Higher speeds will likely cause particles to displace, causing disturbance of the scene.

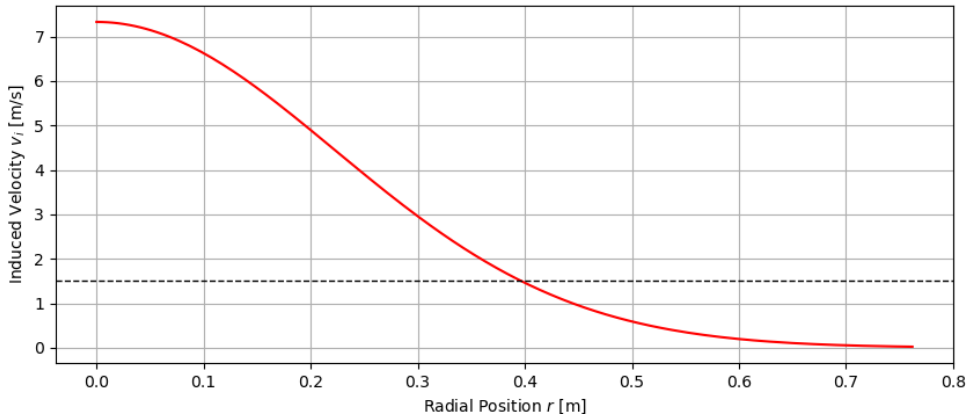

Figure 9.6: Induced velocity at the ground during hover

Figure 9.6 shows how the incoming speed varies over the ground. The maximum velocity shown is a bit over 7 m/s, and at a radial distance of 0.4 meters, the speed is deemed sufficiently low.

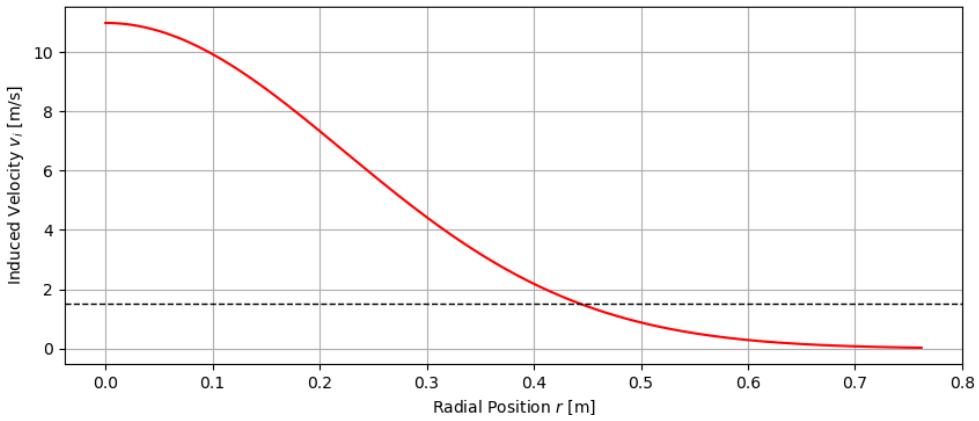

Figure 9.7: Induced velocity at the ground at maximum thrust

In Figure 9.7 , the maximum velocity shown is 11 m/s, and at a radial distance of 0.45 meters, the speed is deemed sufficiently low. From these plots, it can be concluded that the maximum speed at the ground for both cases varies almost ± 40%. The affected area on the area is not nearly impacted as much. The difference in the radius at which the speed is below 1.5 m/s varies ± 10%. From this analysis, it can be concluded that when doubling the thrust, the speed almost doubles, whereas the effected radial distance is not nearly impacted as much.

In order to show the affected area more intuitively, two additional plots were generated showing the area around the propellers in which the speed at the ground is over 1.5 m/s. These plots can be seen in Figure 9.8 in the case of hover and in Figure 9.9 for the maximum thrust case.

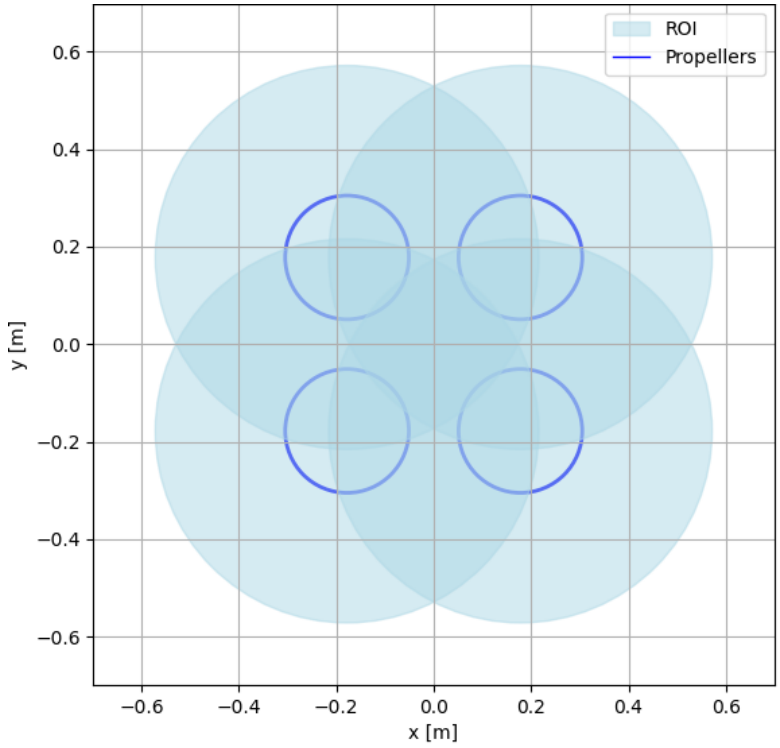

Figure 9.8: The affected area at an altitude of 1.5 meters in case of hover

From Figure 9.8 it can be seen that although the system itself is not that large, the affected area is substantial. The area that might cause disturbance is over 1 x 1 meters. This fact, when considered in tandem with the fact that the system needs to hover above the evidence, means that the scene cannot

be deemed undisturbed and there is a genuine risk of damaging evidence.

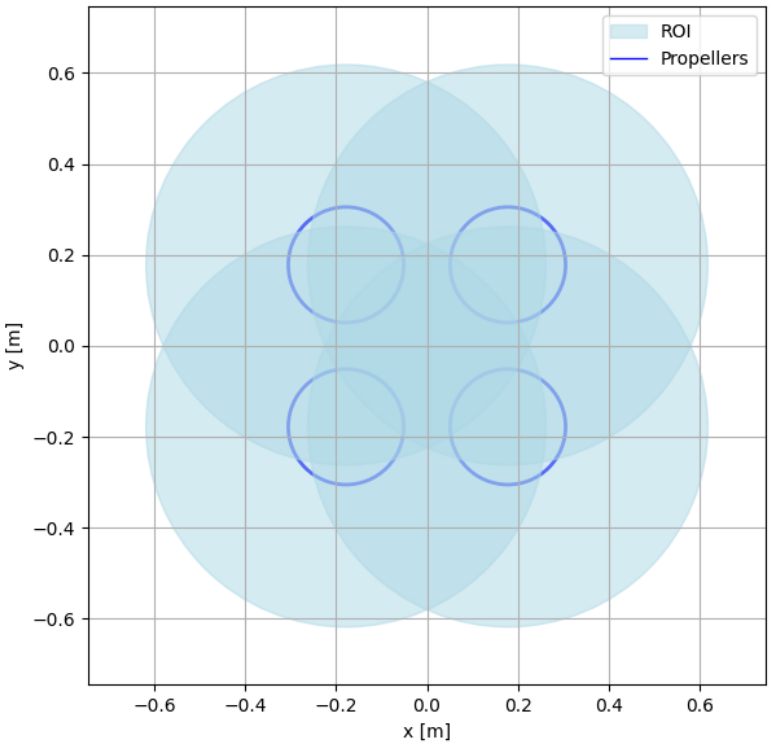

Figure 9.9: The affected area at an altitude of 1.5 meters in case of maximum thrust

When considering the same plot, but in the case of maximum thrust, the situation does not become more favorable. The area increases, but once more not by a drastic amount. The speeds underneath the system are a lot higher than the hover case, so the change of damaging evidence is much higher. Increasing thrust beyond hover when close to evidence should be avoided at all costs.

Now, how high would the system need to fly in order to not disturb the scene? In order to evaluate this the V_{max} is plotted as a function of distance from the propeller plane in Figure 9.10.

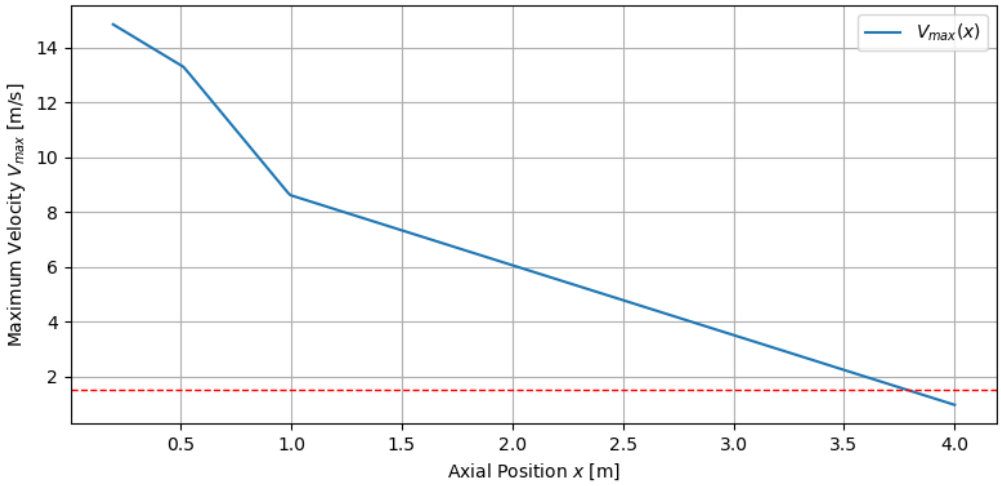

Figure 9.10: V_{max} as a function of axial position for hover

From Figure 9.10, it can be concluded that an altitude of 3.8 meters would not cause the induced velocity at the ground to exceed the 1.5 m/s requirement. When comparing it to the assumption that

the propellers would not impact the flow beyond a distance of ten times the propeller diameter of the first method discussed in Section 9.1, it is quite different. The method would suggest that the flow should not be notably impacted beyond a distance of 2.54 meters. According to the semi-empirical methods, this is not the case. Note that this plot is for the system when it is in hover. The same plot is made for the maximum thrust case and can be seen in Figure 9.11.

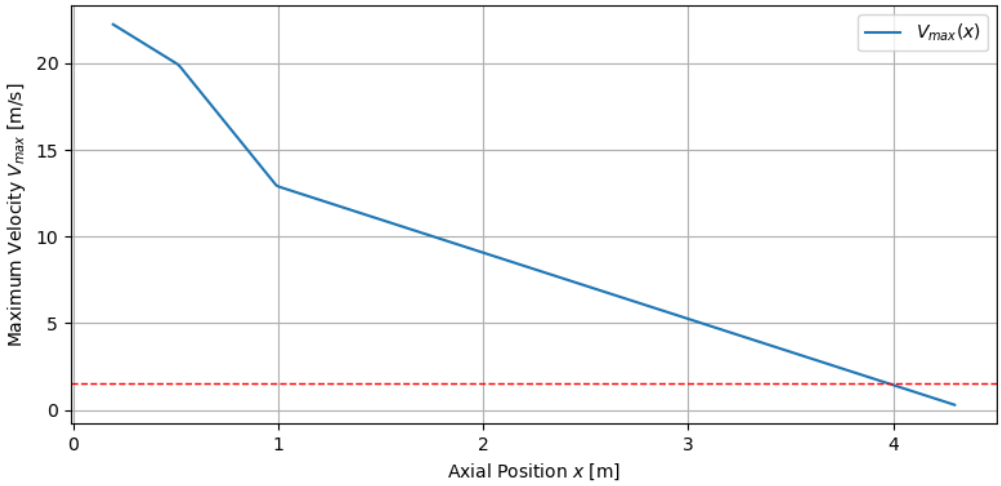

Figure 9.11: V_{max} as a function of axial position for maximum thrust

From this plot it can be concluded that the system would need to fly at an altitude of over 4 meters in order to not disturb the scene. Interestingly, this is not drastically higher than the hover case. However, it is important to reiterate that the velocities are much higher, and the risk of disturbance when not flying at the proper altitude is much higher.

Finally, the values for maximum velocity for each of the methods presented in Section 9.1 are shown in Table 9.4.

Table 9.4: Maximum velocities for all methods considered

	Hover	**Maximum Thrust**
Maximum velocity using thrust [m/s]	13.0	19.4
Maximum velocity using weight [m/s]	12.8	18.1
Maximum velocity using semi-empirical method [m/s]	14.9	22.2

From this table, it can be concluded that the maximum velocities caused by the propellers lie around 14 m/s for the hover case and around 21 m/s for the maximum thrust case. The case that predicts the lowest velocities are the calculations based on the weight, followed by the same calculations but then based on thrust. This is due to the fact that they employ the same method, and there is a bit of excess thrust for both cases. The values calculated are very similar, and do not vary more than ± 7%. In contrast, the semi-empirical method predicts higher velocities and the results differ more significantly from the other methods employed. At worst, it varies ± 23% from the other methods. This occurs when the semi-empirical method is compared to the calculations based on weight in the case of maximum thrust.

9.3. Model Limitations & Recommendations

The semi-empirical method used came with a range of limitations that are important to be considered before discussing the results. This section discusses each of these limitations, their expected affect on the results, and optionally a proposal for how to take each limitation into account.

Firstly, this method only considered axial velocity. This is the velocity in the axial direction to the propeller, i.e. vertically downwards in the case of a quadcopter. In reality, the wake around a rotor is incredibly complex with rotational velocities, also known as tangential velocities, as well. These tangential components can influence the spread of the wake and may redistribute the energy in the radial direction, especially near the tips. By disregarding these, the model may underestimate the lateral extent of the downwash or mischaracterize its shape. However, since axial velocity is the dominant contributor to scene disturbance [2], it is a justifiable simplification for a first-order approximation. For future work, CFD simulations could be used to capture the full 3D wake and quantify the velocity field more precisely.

Secondly, the method assumes that there is no diffusion in the near-field region and no acceleration in the far field-region. In practice, however, diffusion and acceleration affect both regions to some extent. This simplification can affect the accuracy of not only the maximum velocity location but also its decay rate. However, Khan [2] already accounted for this in the coefficients used for his proposed semi-empirical methods. Whilst further accounting for diffusion more accurately would lower peak velocity values, the change would be marginal.

Next, it is important to consider the fact that the interaction between the wakes created by each individual blade of the propellers is neglected. Interaction of two streamlines of accelerating and/or diffusing air is a highly complex phenomenon, which could potentially lead to further diffusion of the flow. Such diffusion could lead to notably lower maximum velocity values at different parts of the flow, improving downwash performance. On the other hand, however, flow becoming more turbulent could lead to increased axial velocities and circulation of the flow, which may once more disturb the rest of the scene. Hence, this is a complex problem that is nearly impossible to theoretically simulate and must once more require the use of CFD simulations. Similar arguments hold for the interaction of wakes from multiple propellers, between the different rotors of the quadcopter, which is an equally complex phenomenon.

Lastly, the interaction of downwash with the ground can lead to a phenomenon known as outwash. This is a lateral outward flow generated near the ground after the downwash interacts with the ground. Although the semi-empirical model fails to account for this, it's effect is negligible as the effect of outwash is only significant when flying at an altitude below 3 rotor diameters, which in this case would be $(0.254m \cdot 3)$ 0.762 meters, whereas this mission's cruise altitude during operation is set to almost double that, at 1.5 meters.

Given all these limitations, it is suggested for future analyses to improve the accuracy of the semi-empirical model. First, and most importantly, the coefficients used in the piece-wise functions defining the flow should most ideally be redetermined through experimentation specifically for the propeller used in this quadcopter's design, as outlined in Section 5.4. In such experimentation, the axial velocities should also be computed such that they can be accounted for. Furthermore, extending the measurement space to both blades of the propeller rather than just one blade shall aid in accounting for areas where wakes between multiple blades interact.

Further downwash quantifications

Other than having more accurate methods of determining the induced velocity, it is also crucial to have methods that can quantify downwash in a more meaningful way. Ultimately, the displacement of particles is what should be avoided. As of right now, there are no calculations that attempt to quantify this. This subsection aims to outline some possible approaches. Firstly, a method is needed to calculate the outwash, as the airflow that moves along the ground is the flow that will displace particles and objects. The simplest approach is to assume the ground as a flat plate that acts as a stagnation point. An illustration demonstrating this is shown in Figure 9.12.

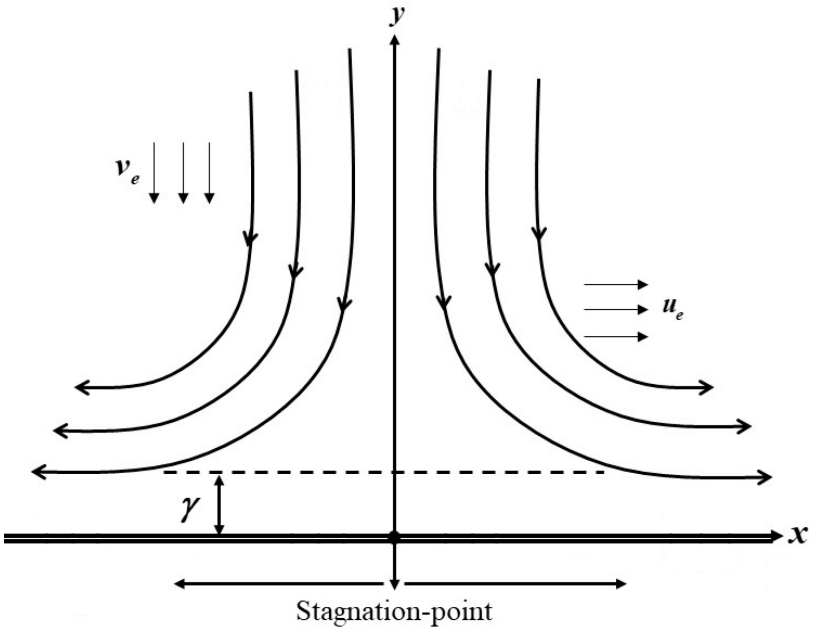

Figure 9.12: Flow profile for a airflow hitting a flat plate[37]

Using this method should allow one to find the velocity along the ground. The next step would be to determine the minimum speed that is required to move a particle. This would entail finding the drag of a particle, the friction between the particle and the floor, leading to the impulse required to make the particle move. Furthermore, if a particle is displaced, it is valuable to calculate the distance it would be moved.

9.4. Verification and Validation

This section aims to demonstrate the verification and validation process used for the downwash calculation methods. Firstly, the model will be unit tested, followed by comparing the generated results with those outlined in the original method [2]. After the verification, the validation process will be briefly discussed.

Verification

Before the results of the code can be deemed accurate, the code used has to be verified. As mentioned, this will be done by first conducting thorough unit tests, followed by plot comparisons between the model used and the paper that the model was taken from.

For the unit testing, running a coverage test using the python package `coverage.py` reveals a total coverage of 97% of the file `Structures_arm.py` with only 4 lines of code not being run as they are related to conditional `if` statements. Figure 9.13 shows the coverage breakdown.

File ▼	function	statements	missing	excluded	coverage
prop_downwash_NEW.py	V_max	7	1	0	86%
prop_downwash_NEW.py	R_max	7	1	0	86%
prop_downwash_NEW.py	v_i	7	1	0	86%
prop_downwash_NEW.py	plot_downwash	31	1	0	97%
prop_downwash_NEW.py	plot_ground_velocity	45	0	0	100%
prop_downwash_NEW.py	print_induced_velocity_prop	7	0	0	100%
prop_downwash_NEW.py	*(no function)*	47	0	0	100%
Total		**151**	**4**	**0**	**97%**

Figure 9.13: Coverage breakdown of verification tests for downwash calculations

Beyond the unit test verification, the results from the model used were also compared to the results from the paper by Khan [2]. The input parameters that were used in the paper were input into the model, and the same plots shown in the paper were generated and compared. The input parameters are as follows: the C_T is 0.1542, the RPM is 5425, and the propeller diameter is 0.254 meters.

The first plot that will be compared is the plot showing the maximum induced velocity as a function of the axial distance from the propeller plane. Note that the method used in this report does not include the area in between the propeller plane and the efflux plane, and this region will therefore not be compared. The plot from the paper and the plot generated by the team are shown in Figure 9.14 and Figure 9.15 respectively.

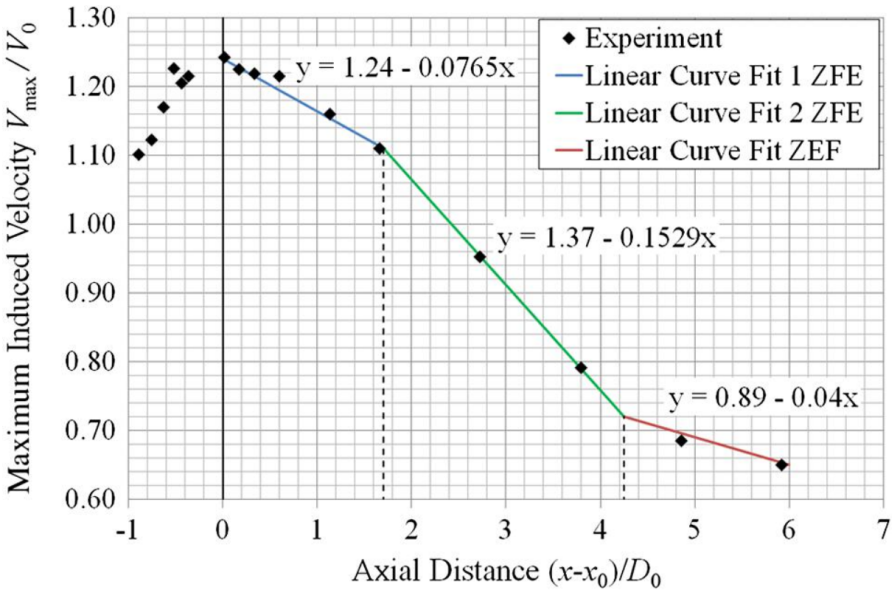

Figure 9.14: Maximum induced velocity over V_0 plot from methodology paper [2]

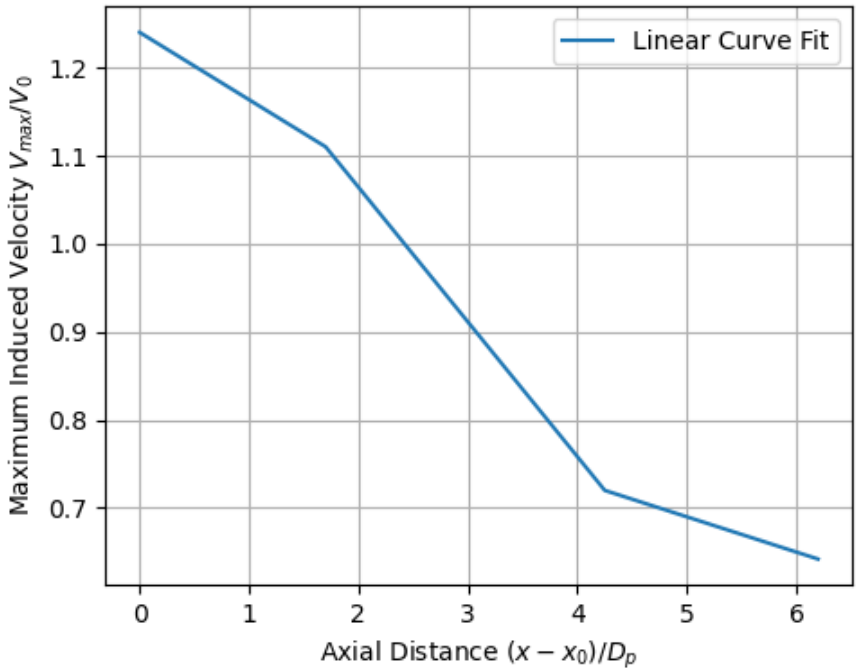

Figure 9.15: Maximum induced velocity over V_0 plot from code used

Both plots show the exact same velocity profile, and the V_{max} calculations along the axial distance can therefore be deemed verified. This means that the only part of the code that needs to be compared to the paper is the induced velocity along the readign distance. Unfortunately, there is no plot in the paper that mimics the heatmap that are used in the results. However, the paper does show a plot that evaluated the induced velocity as function of radial distance at three different axial locations along the flow. The three locations are all in a different region in the flow, and if the plot generated by the code used is the same, all three of the semi-empirical formula's can be verified. The plot shown in the paper can be seen in Figure 9.16, and the plot generated by the code used in Figure 9.17.

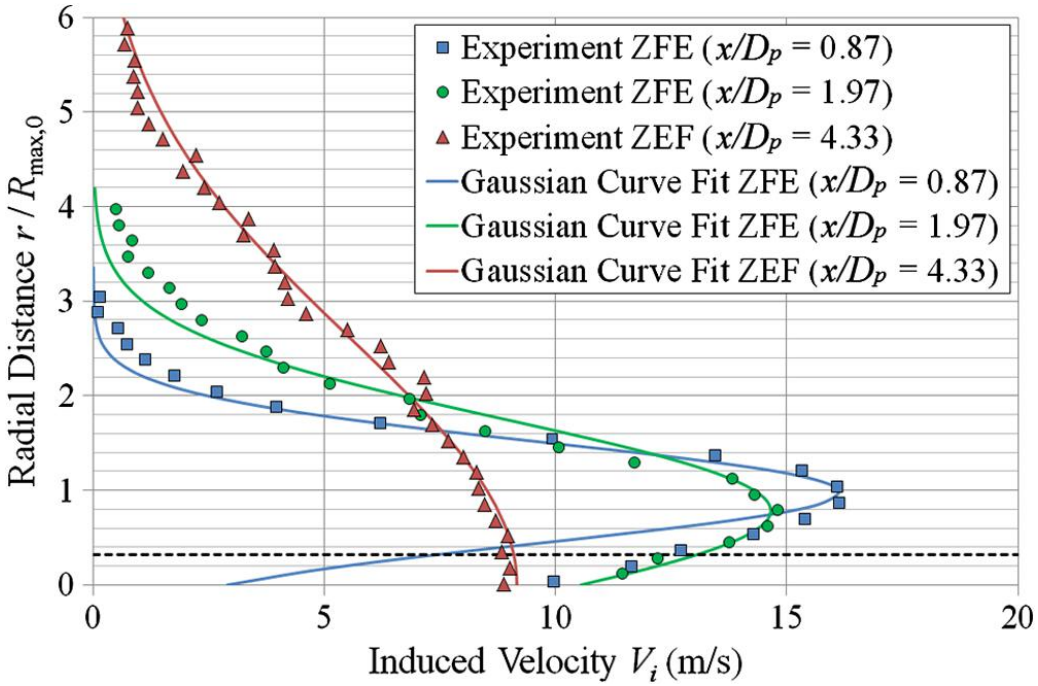

Figure 9.16: Induced Velocity plot at three distances from the propeller plane from [2]

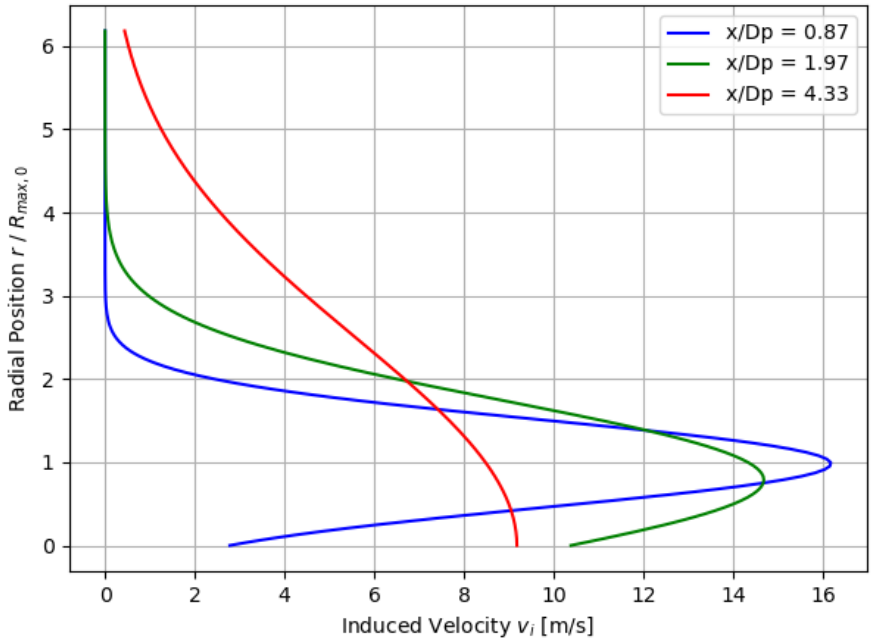

Figure 9.17: Induced Velocity plot at three distances from the propeller plane from the code used

The plot shown in the paper and the plot generated by the code used are identical, and therefore the induced velocity calculations can deemed to be verified. This means that the code works as intended.

Validation

In order to truly determine that the results gathered from the code are viable, they have to validated by comparing them with actual experimental data. In the case of downwash calculations this can be quite difficult to obtain. Downwash is not often considered as a relevant spec by many drone manufacturers. Luckily, the semi-empirical method used by Khan [2], is validated and can therefore be assumed to have some level of legitimacy. However, the coefficients found in that paper were for a different propeller and operational mode. The validation experiments that were used in the paper can therefore not be repurposed to validate the results gathered from the code. Thus, it was decided that the best way to make sure the calculations used are valid, is by applying a safety margin.

9.5. Discussion of Results

When considering the limitations of the method used (Section 9.3) and the lack of validation, it is clear the calculations leave a lot to be desired. Unfortunately, at this time it does not seem likely that the model can be improved without making use of CFD or experiments. This means that a margin is necessary to account for the shortcomings of the method.

An appropriate margin is found by first comparing the three methods used with each other. As mentioned in the results section (Section 9.2), the semi-empirical method can vary by a margin of ± 23% from the other two ways of calculating. This suggests that that is the minimum margin that should be applied. Next, the limitations of the model should be taken into account. As of right now, it is expected that the interaction between the different propeller wakes is likely to cause a deviation of about ± 10%[38]. The other limitations do influence the characteristics of the flow, but are likely to cause more effects in the radial directions. Since they are not likely to impact the axial velocity, they are not taken into account for the margin. Therefore it was decided that the final margin applied to the results should be ± 40%. The final maximum velocities at the efflux plane, 1.5 meters and 2 meters from the propeller plane including their respective margins are shown in Table 9.5. Note that the values are rounded to the nearest integer, as a higher level of accuracy is not warranted.

Table 9.5: Maximum velocities at different axial distances and the margin applied

	Hover	Maximum Thrust
Maximum velocity at efflux plane [m/s]	15 ±6	22 ±9
Maximum velocity at x = 1.5 meters [m/s]	7 ±3	11 ±4
Maximum velocity at x = 2 meters [m/s]	6 ±2	10 ±4

It should be noted once more, that the only way to get accurate results would be through either CFD or experimental testing. Testing would be the most ideal method, and the most attractive in this case, as the components used are available on the market and should therefore be easy to obtain and test in-house.

9.6. Downwash-Driven Design Recommendations

This section aims to cover some areas that were not able to be considered using the methods outlined in Section 9.1. Firstly, the effect of propeller geometry will be outlined, followed by some suggestions on additional downwash mitigation strategies that could be explored in more detail in the future.

Effect of propeller geometry on the induced velocity

As mentioned in previous sections, the semi-empirical method does not take into account the effect of the propeller geometry outside of the diameter and the C_T, the latter of which is based on geometry. While in reality, characteristics such as twist angle, pitch distribution, and chord variation across the blade span do affect the local angle of attack and lift production, these effects are implicitly seen in the experimentally determined C_T value.

Nonetheless, it is still useful to consider how individual geometric parameters could influence the downwash. For example, a lower blade pitch angle generally reduces the induced velocity, since it results aggressive acceleration of the air. However, to maintain the same thrust, this would require increasing the rotational speed, i.e. the RPM, which can reintroduce higher induced velocities and increased energy consumption, as the RPM is directly proportional to the induced velocities as indicated in Equation 9.3. Similarly, increasing the chord length or altering the chord distribution could improve efficiency by reducing tip losses. Whilst this marginally affects the velocity profile of the wake, the maximum velocity reached remains largely unaffected.

Blade twist, which adjust the angle of attack along the blade, can optimize lift distribution. This has a smoothing effect on the wake, but once more does not substantially reduce the maximum induced velocity. Moreover, airfoil selection also place a role, where thicker or cambered sections can enhance lift at the cost of drag, slightly worsening the downwash characteristics.

Despite these theoretical influences, the overall effect of adjusting individual airfoil parameters is relatively minor in practical scenarios. Most commercially available propellers are already optimized for efficient thrust generation, which inherently includes minimizing unnecessary induces velocities. A more detailed investigation into these geometric effects on downwash was considered beyond the scope of this project due to time and resource constraints. Moreover, although a propeller design could be tweaked for slightly more optimal downwash performance, this would come at the cost of propulsive performance. While the minimization of scene disturbance is an important mission requirement, the ability of the quadcopter to sustain flight is of higher importance for the mission to actually be carried out, and hence it remains more critical for propellers to be designed such as to sustain flight.

One parameter that is important to consider and could have positive impact on the downwash is the propeller diameter. From the method formulas, it can be deduced that an increase in diameter increases the V_0, reduces the rate of deceleration and decreases the affected area. From this, it can be concluded that a smaller propeller would be beneficial for downwash. On the other hand, the first method outlined, states that an increase in diameter would lead to a decrease in induced velocity.

However, this method agrees that a smaller propeller would lead to faster deceleration to the flow. This means that in any case, a smaller propeller means that the drone would be able to fly at a lower altitude without causing a disturbance. However, as was discussed in the midterm report[4], smaller propellers are less efficient and require way more power to produce the same amount of thrust when compared to a bigger propeller. A more in dept study should be conducted investigating the impact of decreasing the propeller has on the design and on downwash.

Other downwash reducing possibilities

Outside of modifying the propulsion system, more unconventional techniques can be considered to attempt reducing downwash. Some of the possible ideas are outlined in this section.

Firstly, a diffusion system was considered. This would entail attaching a mesh on the bottom of the system, similar to the mesh that is attached to a standard fan one would use to cool down. Ideally, this mesh would disrupt the flow, making it turbulent and therefore decrease the velocity. Aside from the fact that the impact of such a mesh would be difficult to calculate, some other downsides should be mentioned. First and foremost, attaching a mesh to the bottom of the drone would cause some of the flow to hit the mesh head on, effectively 'pushing' on it. All the force that is 'pushing' on the mesh will be subtracted from the thrust of the system. This would cause the propulsion system to become significantly less efficient, increasing the required thrust, which then causes a snowball effect that increases the weight of the system and by extension, the downwash. Likely, the added benefit of the mesh will be outweighed by this downside of having to generate more thrust. In addition to this, the mesh might interfere with the landing capabilities of the system. Depending on what the optimum distance from the propeller plane is, the mesh might be positioned below the landing gear. This could cause logistical issues. Alternatively, on can make use of objects hanging below the rotors. For example, if one were to hang circular objects below each of the propellers, the flow would be dispersed. And since each object is hanging on it's own, it should not interfere with the landing capabilities of the system.

Similarly, one could add ducts to the propulsive system, which in themselves would not help downwash significantly, but when attaching streamers to the ducts, the flow might be dispersed, lowering the maximum induced velocity. However, this approach is once more not without its challenges. Firstly, the streamers could get tangled with the propellers and damage the propulsive system. This would be catastrophic and would be reason enough to not use the streamers, even if they do significantly decrease downwash. This is also not likely to be the case however. Since the airflow first compresses and then expands, it would only be valuable later in the flow, since the streamers would only be able to impact the flow once the radius of the flow is bigger than the propeller diameter. Even then, the streamers would not be able to impact the flow speed in the middle of the propeller, where the speed are the highest. At best, streamers would be able to decrease the affected area, but it is unlikely to help with the maximum induced velocity.

9.7. Final Remarks

As seen in Table 9.5, the maximum induced axial velocity for hover and maximum thrust are 4-10 m/s and 7-15 m/s ±40% respectively when at an altitude of 1.5 meters. This is certainly higher than the 1.5 m/s velocity that was required at the ground in order to not lift any dust particles from the ground whatsoever, even if just the lower end of the values with safety margins are considered.

The downwash may be reduced in the future with further design iterations. As outlined in Section 9.6, many unique design ideas come with long lists of limitations and possible problems. As such, the most likely design improvements would be decreasing the propeller sizing, or, more importantly, reducing the weight of the quadcopter and hence the required thrust.

However, all commercially available drones disturb the scene they fly in to certain extent. As long as air is being pushed through the rotors downwards in order to sustain flight, it shall be accelerated by some amount. Hence, it is expected that even if downwash is reduced in future design iterations, a certain level of disturbance to the scene is inevitable unless a substantial flight altitude is established, which shall most likely exceed the acceptable altitude for typical indoor operations.

10 - Performance Analysis

After the system has been finalized, a detailed description of its components can be presented. After detailing this, the performance metrics of the complete system can be calculated. Both the final design and its performance metrics will be presented in this section. The performance metrics include the time per mission, total mission time, and area covered per mission and per day were found.

10.1. Final Design

In this chapter, the final design of the Fire-Eye quadcopter is presented. Each subsystem has been reviewed in detail, and component selections have been made based on technical requirements and system integration constraints. Figure 10.1 shows a 3D render of the complete system, while Table 10.1 provides an overview of the selected components which are present in the quadcopter during a mission, including their function, mass, and power consumption.

Figure 10.1: Drone final design.

Table 10.1: Summary of component name, mass, and power consumption

Subsystem	Component Name	Description / Task	Mass [g]	Power [W]
Propulsion	MR Series 10×4.5	Fixed-pitch propellers for lift generation	12.80 (×4)	–
	Selig S1223	Airfoil used in aerodynamic modeling	–	–
	4 × XING 2814	Brushless motors for thrust generation	393.20	393.6 per motor at 85%, 123 at 55% throttle
	T-Motor F45A ESC	Electronic speed controllers for motors	10.00	–
Power	SMC HCL-HP 6S Battery	Power supply for all electronics	1065.00	–
	PDU BEC12S-PRO	Power distribution and voltage regulation	5.00	–
Mapping	Voyant Helium	FMCW LiDAR for 3D environment mapping	150.00	27.00
Forensics	9 × Seoul Viosys CUN66B1G	UV LEDs for fluorescence detection	4.00	33.30
	Arducam IMX462 (Downward)	Camera to capture UV fluorescence	9.00	1.50
Communications	Herelink 1.1	Ground communication and telemetry	68.00	4.00
	Cube Orange+	Flight control and sensor fusion hub	73.00	5.00
	Orange Pi 5	Companion computer for data processing	46.00	5.00
Control & Navigation	ToF (Cruise Speed)	Obstacle detection during flight	7.50 (×2)	0.25
	Arducam IMX462 (Forward)	Forward-facing camera for spatial awareness	9.00	1.50
	IMU (in Cube Orange+)	Provides acceleration and angular rate data	–	–
Frame	Landing Gear	Support for take-off and landing operations	24.00	–
	Skin	Payload protection against environment	120.00	–
	Propeller Arms	Support motors and transmit thrust loads	30.00	–

10.2. Flight Profile

As explained in Section 2.1, the flight consists of multiple sequential phases. For flight, these are take-off, approach, navigation to the scene, execution of the mission itself, return, and landing. For simplicity, the first three active phases, being take-off, approach, and navigation to the target, are grouped under one term as the entry phase. Then, there is the mission phase, which consists of two options, mapping and forensic research. Lastly, there is the return phase, which includes the navigate from scene, return, and landing. The recommended approach is mapping the entire building first, and then doing forensic research of the entire building afterwards. The conditions of each phase will be elaborated upon in the succeeding subsections.

Entry
This phase involves movement only, without any active use of mission payloads. To achieve this movement, the motors provide a thrust-to-weight ratio of two, as this was determined for the thrust for take-off. This phase is approximated to be 90 seconds at most. This is an overestimation, as some pre-mission checks are also performed, guaranteeing beforehand that subsystems perform as desired. Then, take-off and navigation to the site are performed in under twenty seconds, as the quadcopter starts in close proximity, and the thrust is high. It was determined that the thrust-to-weight ratio is 2.25 at take-off.

Mission
The second phase is the mission phase. This has two options. Firstly, it maps the building. This goes faster as opposed to the forensics mission profile due to two reasons. It is not limited by motion blur as it can detect objects up to 63m/s , and the resolution is not limited by a light, allowing for a larger range of distances to be scanned. For both mission profiles, the quadcopter is required to hover, meaning that the thrust-to-weight ratio is one. The throttle setting was computed for this, according to the following formula [39]:

$$T = C_T \rho n^2 D^4 \tag{10.1}$$

This shows that $T \propto n^2$. From this, it was found that the throttle setting was 55%, which has a much lower required power than full thrust.

Mapping
During mapping, all attached components are powered continuously. The required power for this part of the mission is 534W. The quadcopter is expected to fly at an average of 1m/s, since it is not restricted by the capabilities of its components. However, in order to operate safely, meaning it does not crash, it should not go faster than this speed. This gives the operator enough time to respond and the ability to maneuver corners, while also minimizing motion blur. Estimating the coverage area of the mapping mission is hard, since the LiDAR can detect up to five meters, however, most buildings have areas that are smaller than this. A width of 2 meters was assumed, as this is a conservative estimation of an average width for hallways and rooms. This led to a ground coverage rate of 2 m^2/s. The mapping is done in three dimensions, however, the coverage is expressed in square meters, as this translates more conveniently into a mission duration and is more understandable.

Forensics
The forensic mission is not powered continuously. The LEDs receive bursts of power from the capacitor, to avoid overheating, which might occur if the lights are constantly powered. The LEDs are powered for 0.2 seconds. They illuminate a circular area, however, following from **REQ-STK06-MIS19-PAY01** and Table 4.2, is a square area of $0.8^2 m^2$. This is the area that every corner is illuminated. The total width would be more, however areas would be missed if that larger width is assumed. To determine the flight speed for the forensic mission, the motion blur of the chosen cameras was considered. Motion blur is hardly visible for the human eye up to two pixels [1]. The pixel size is found first. From this, the velocity was determined as per the following formula:

$$V_{max} = \frac{pixel\ size}{shutter\ speed} \cdot allowable\ pixel\ size \tag{10.2}$$

Substituting in the system parameters, the maximum velocity to avoid noticeable blur was calculated as 0.53m/s. To stay within this limit, the quadcopter is programmed to fly at 0.5m/s during forensic operations. This is necessary to find two things. Firstly, it leads to the time between each flash. As the illuminated area is square, it is the distance to travel from one side to the other of this area. Here, it needs to flash again to illuminate another area. It was established that the array must be on a loop of 1.6s, where it is on for 0.2s and off for the remaining time. Secondly, it is necessary to calculate the mapped area per second. This follows logically from the illuminated width and the velocity, turning out to be $0.4 \frac{m^2}{s}$.

[1] URL: https://www.vision-doctor.com/en/camera/exposure-time-area-scan-camera.html [Cited 17/06/2025]

Exit

The last phase is returning from the site. This was settled at a time of one minute, with the same conditions as for the entry phase. In reality, this is not necessary, as the descent of the quadcopter requires a thrust-to-weight of less than one. Moreover, a minute is a conservative estimate, especially since the operator is in close proximity. However, this overestimation allows for a margin in the leftover battery power at the end of a mission, possibly required for unexpected phases, such as exit at a different location from the entry point.

10.3. Flight Time

After the flight profiles are established, the total flight time and the total mission time is determined. These are produced to find out if the quadcopter complies with **REQ-STK-01**. Before this was explored, assumptions had to be established. This mission profile as presented above, describes the maximal setting this quadcopter can perform. This means that the battery is fully drained, and that every area that is mapped is new. In reality, once a certain part of the building is larger than the mapping area, this might not always be the case. Moreover, in most buildings, it is the opposite, a floor could be less than the total area that it maps, which also extends the total time that it could take. In addition to that, the power draw is estimated at a 100% efficiency. Another assumption is that everything is taken as averages. This means that the flight speed is constant and the power consumption during each phase is constant, except for the forensic mission. The battery is assumed to starts at 100% charge, which in reality reduces after multiple mission cycles. A conservative assumption was made for the entry and exit phase, determining them as a set time, with a throttle setting of 80%, resulting in a desired thrust-to-weight ratio of 2.25.

The power consumption and maximum time per phase are stated in the table below.

Table 10.2: Power and energy consumption, phase duration, area coverage, and energy per unit area.

Phase	Power consumption (W)	Energy consumed (Wh)	Phase duration (min)	Total area covered per mission (m^2)	Energy per unit area (Wh/m^2)
Entry	1385.0	34.6	1.5	–	–
Mission: Mapping	534.4	111.0	12.5	1495.6	0.113
Mission: Forensics	503.6	111.0	13.2	317.4	0.531
Exit	1385.0	23.1	1.0	–	–

From this table, it is deduced that the total flight time with the mapping configuration is 15 minutes, and is nearly 16 minutes for the forensic configuration. Evidently, the quadcopter cannot complete its mission in one continuous flight. After landing, the battery is switched out, a new one is placed in, and the quadcopter returns to the mission. This turnaround time was chosen to be 10 minutes. Moreover, a total of an hour is given to account for assembly at the start of the day and disassembly at the end. Assuming a working day is eight hours, this means that seven hours are left for the mission. It can be deduced that both configurations can do 16 cycles. This leads to a covered area of 23900 m^2 per day for mapping, and 5080 m^2 per day for the forensic configuration.

10.4. Verification and Validation

After deriving the flight performance characteristics, it is crucial to verify their legitimacy and validate them with real-world cases. Firstly, code verification is performed. In addition to that, validation was conducted, taking the Grenfell Tower as an example.

Verification

One limiting factor for the mission could be on-ground operations during the mission. For example, the battery has to be charged every turnaround. During each new mission, the battery from the previous mission is charged. The C-rating of charging the battery is given, which is one if the battery recharges fully in an hour. For Fire-Eye, the battery has a C-rating of 5, meaning it has a charging time

of 12 minutes. This is assuming that there is 100% charging efficiency. However, this is usually over 95%, meaning it could take a total of 13 minutes. This verifies that this does not pose a limiting factor.

The battery selection for the Fire-Eye raises valid concerns regarding its charging rate, thermal management, and overall longevity. Multiple sources recommend limiting the charging rate to preserve battery health. The supplier of the selected battery specifies a safe C-rating range of 1 to 5, and states that exceeding this range negatively impacts performance and significantly degrades cycle life[2]. To increase battery longevity, it is recommended to use the lowest supported C-rating of 1. Consequently, five batteries are employed in the system to allow battery swapping after each mission. This setup enables concurrent charging of all batteries that are not in the quadcopter at that moment, under a constant current–constant voltage profile at a low C-rate.

The performance metrics shown in Table 10.2 assume complete charge and full discharge of the battery. However, this is not recommended for optimal battery health. A more conservative state-of-charge (SoC) window of 20–90% is generally advised to prolong the lifespan of lithium-based batteries[3].

That said, the Fire-Eye is not expected to undergo a high number of operational cycles, particularly in large-scale or frequent deployments. Moreover, the inclusion of five swappable batteries in the system package further alleviates cycle-related degradation. While full discharges are generally discouraged, in this context, they remain acceptable due to the limited number of total cycles expected.

Under standard assumptions, a LiPo battery subjected to full 100% SoC and 100% DoD yields approximately 600 charge cycles[40]. With five batteries in rotation, this results in a total of 3,000 mission-capable cycles. Given the system's operational requirements—approximately 1500 m^2 coverage per mapping mission and 317 m^2 per forensic mission. This capacity is sufficient even for long-term usage. For reference, a large-scale structure such as a multi-storey apartment building may span around 12,000 m^2in surface area[41]. Based on this, a single battery can cover 157,500 m^2 in mapping mode in 105 cycles, and 156,915 m^2 in forensic mode across the remaining 495 cycles of its estimated lifetime.

Another verification is performed to check the power provided for the complete quadcopter. The total current is calculated to be 62.4A at most, which is during the entry and exit, where all motors are powered directly from the distribution power unit, meaning it is connected in parallel. This is less than the discharge rate.

Validation

To prove compliance with **REQ-STK-01**, the Grenfell Tower is taken as an example. This was given as an example in the project description, and due to its large size, it poses a real challenge for post-fire investigation. The building consists of 24 floors, leading to a total of 11700m^2 [41]. Comparing this with the covered area per day, it can be deduced that the building can be mapped within a week. It can be fully mapped in 4 hours, and fully scanned for human remains in 17 hours. This includes the turnaround times. This means that the mission can be accomplished in 3 days. Even with a safety factor of two to account for areas being covered inefficiently, it is still under a week.

A sensitivity analysis was performed to verify whether half the illumination width would still be able to map the Grenfell Tower in seven days, and it would double the time the forensic mission takes. This leads to a total mission time of five days. This means that, in the case that the LED array does not provide enough power to luminesce human remains, another array could be built and implemented. This could have a smaller directivity angle, meaning more power is provided. Also, if the power is enough but the downwash is too large, the hovering height could be increased if a smaller directivity angle is applied. This would follow from testing in the future.

[2]URL: https://www.smc-racing.com/index.php?route=product/product&product_id=679, [Cited 24/06/2025]
[3]URL: https://batteryuniversity.com/article/bu-808-how-to-prolong-lithium-based-batteries, [Cited 24/06/2025]

11 - Compliance Matrix

In this chapter the requirements compliance matrix of the Fire-Eye is presented in Table 11.1 , The compliance matrix is the last assessment of the design's adherence to the user requirements established earlier in the project by the client. Each requirement is evaluated against the current system implementation, with tick marks indicating compliance. In cases where a requirement is not fully met, the matrix includes the achieved value and is supported by a rationale detailing the cause of non-compliance and, where applicable, the design modifications that would be necessary to achieve compliance.

Table 11.1: Requirements compliance matrix

ID	Requirement	Compliance
REQ-STK01	The system shall be able to fully map a typical apartment building of $500m^2$ within 1 week of operation.	✓
REQ-STK02	The system shall be able to create a 3D mapping of the scene with a resolution of 1 cm.	✓
REQ-STK03	The system shall be able to georeference the map with a resolution of 1 cm.	✓
REQ-STK04	The system shall be able to geolocate detected human remains.	✓
REQ-STK05	The system shall be able to enter scenes through an opening of no larger than 70 x 70 cm.	✓
REQ-STK06	The system shall be able to employ UV fluorescence to detect human remains.	✓
REQ-STK07	The system shall comply with EASA requirements for safe operation of drones.	✓
REQ-STK08	The system shall comply with ILT requirements for safe operation of drones.	✓
REQ-STK10	The system shall not damage forensic evidence.	TBD
REQ-STK11	The system shall have an availability of 99% based on the Dutch climate.	TBD
REQ-STK12	The system shall be 75% by weight recyclable, excluding the payload.	X
REQ-STK13	The system shall have a unit purchase cost of no more than €50,000.	✓
REQ-STK14	The system shall be operable by a licensed 'certified' category UAS operator after 32 hours of training.	✓
REQ-STK15	The system shall be designed in 10 weeks time.	✓
REQ-STK16	The system shall be designed by 10 students.	✓
REQ-STK17	The system shall be manufacturable.	✓
REQ-STK18	The system shall be maintainable by a licensed technician.	✓
REQ-STK19	The system shall be able to operate beyond visual line of sight.	✓
REQ-STK21	The system shall be able to flag regions after localization of human remains.	✓
REQ-STK22	The project shall at all times adhere to the TU Delft code of conduct.	✓
REQ-STK23	The system shall be transportable to various locations in The Netherlands using existing fire department infrastructure.	✓

Table 11.1: Requirements compliance matrix

ID	Requirement	Compliance
REQ-STK25	The system shall not cause harm or endanger the operating crew or bystanders.	✓
REQ-STK26	The system shall be operable in a temperature range of −5 to 50°C for at least 60% of nominal operating time.	✓

While reviewing the compliance of all user requirements, it became clear that most requirements have been met within the scope of the Fire-Eye system. However, a number of individual requirements stood out due to the need for clarification, client discussion, or specific design considerations. Several requirements that either required additional discussion with the client, introduced interpretational challenges, or highlighted meaningful design trade-offs are discussed.

The first case is **REQ-STK03: The system shall be able to georeference the map with a resolution of 1 cm**. During the process, it was clarified that this requirement refers to the accuracy of the system's own position within the generated map, ie, the accuracy of the quadcopter's location itself rather than the accuracy of the geolocation of individual points on the map. This interpretation was used as a reference in the design process and in the trade-off of the mapping subsystem.

Next, **REQ-STK05: The system shall be able to enter scenes through an opening of no larger than 70 × 70 cm** was initially challenging due to the tight constraint relative to the required drone footprint and stability margin. Following consultation with the client, it was agreed to increase the maximum allowable opening to 70 × 70 cm rather than the previously agreed on sizing of 40 x 40 cm, which still ensures access to confined spaces.

Two additional requirements were removed during the design phase following client discussions. These were:

- *REQ-STK09: The system shall not displace debris weighing more than <TBD> grams from its point of origin.* This was removed as its purpose was already addressed by REQ-STK10, and further constraints would unnecessarily restrict propulsion design without added forensic benefit as the client wants a zero displacement.
- *REQ-STK24: The system shall be able to conduct the mission in a partially collapsed building of <TBD>m^2*, which was considered redundant as its intent is already fully covered by REQ-STK01

At this stage, compliance with **REQ-STK10** and **REQ-STK11** is to be determined. First **REQ-STK10: The system shall not damage forensic evidence** will be discussed. It is clear from the downwash analysis that the propulsion system produced too much downwash to not move any dust. However, it is not clear at this stage if the induced velocity caused by the propulsive system is enough to move particles that are significant to the investigation. Further research should be conducted in this area, as mentioned in Section 9.3.

Regarding **REQ-STK11: The system shall have an availability of 99% based on the Dutch climate**, this requirement is currently marked as TBD. Further quantification of mission availability under various weather scenarios (including wind, temperature, and rain) will need to be carried out in the post-DSE phase when the project continues into testing or prototyping.

In terms of sustainability, **REQ-STK12: The system shall be 75% by weight recyclable, excluding the payload** was found to be non-compliant. Although most structural and electronic components are recyclable, the battery, which represents a significant portion of the total system mass is not. Additionally, the use of glass fiber-reinforced materials for structural elements complicates recyclability due to the processing limitations of such composites.

REQ-STK14: The system shall be operable by a licensed 'certified' category UAS operator after 32 hours of training, the 32 hours is based on the average duration of certified UAV training programs focused on photogrammetry and mapping [1], these include training and certification for the pilot to operate the drone after examination.

[1] URL: https://eudroneport.com/drone-training/ [Cited 16/06/2025]

Lastly, **REQ-STK26: The system shall be operable in a temperature range of –5 to 50°C for at least 60% of nominal operating time** has been met. All components used in the payload and supporting electronics were selected with this environmental range in mind and validated throughout the design to ensure reliable operation.

12 - Operations and Logistics

The successful deployment of any advanced aerial system depends not only on its technical capabilities but also on how reliably, safely, and efficiently it can be integrated into existing operational frameworks. This chapter evaluates the technical robustness of the Fire-Eye System. The RAMS analysis assesses the system's reliability, availability, maintainability, and safety, ensuring it can perform consistently and safely in mission-critical scenarios.

12.1. RAMS Analysis

The RAMS analysis is conducted to verify that the system performs to the highest standards of reliability, availability, maintainability, and safety. This section evaluates the design and operational characteristics of Fire-Eye, assessing its capability to function consistently across different scenarios, reducing the risk of failure, and protecting user safety.

Reliability

Reliability refers to the quantitative measure of how likely a system is to operate without failure over a specific period. It is essential to express this numerically, as it will make it clearer to align with the stakeholders' needs and comply with the testing guidelines. The parameter is the Failure Rate (FR), which indicates the number of failures per unit of operational life. Although it may be less intuitive than the Mean Time Between Failures (MTBF), the FR is a valuable mathematical concept commonly used in engineering and statistical analyses.

An estimation of the reliability for the system and subsystems can be deduced from parameters like the Take-Off Weight or partial weight of the subsystems, design role, complexity level, technological age, and maintenance. To estimate the total failure rate of the system, the bottom-up or top-down method is used. In the bottom-up method, the total failure rate of the system is the summation of each subsystem as seen in Equation 12.1 where λ is the failure rate of the subsystem.

$$\lambda = \sum_i \lambda_{E_i} \tag{12.1}$$

However, the top-down method relies on the allocation of the system failure rate value, which is based on historical data. In the paper [42], this method is applied to existing aircraft, but not to quadcopters. However, the same approach is allowed, yet only the values are different as seen in paper [43].

- Technological Age Index (IA) resembles the technology level used during the design process. A lower index indicates newer technology.
- Complexity Index (IC) is an index for the complexity of the quadcopter. A lower index means a low level of complexity.
- Role Index (IR) highlights the importance of the drone's role. A higher IR relates to a more important role.

With these definitions, the failure rate of the aircraft can be determined as seen in Equation 12.2.

$$\lambda = \left(\frac{\lambda}{\text{MEW}}\right) \cdot \text{IR} \cdot \text{IC} \cdot \text{IA} \cdot \text{MEW} \tag{12.2}$$

Where $\frac{\lambda}{\text{MEW}}$ is the failure rate divided by the Maximum Empty Weight and is assumed to be equal to $1.8 \cdot \frac{\text{failures}}{1000\,\text{FH} \cdot t}$. Here, FH stands for flight hours and t is time. The estimated failure rate of the system is presented in Table 12.1.

Table 12.1: Failure Rates by Component

IA	IC	IR	MEW [g]
0.6	0.5	1.5	1901
Total Failure Rate			1.5

To calculate the failure rate per subsystem, the subsystem weights and historical data were used as inputs in Equation 12.3 and Equation 12.4. In this equation, λ represents the system's failure rate, K_i is a normalized failure rate coefficient specific to each subsystem, W_i denotes the weight percentage, and λ_i refers to the non-normalized failure rates. The K_i values were sourced from empirical data and the final results are summarized in table Table 12.2.

$$K_i = \frac{\lambda_{i_{\text{avg}}}\%}{W_{i_{\text{avg}}}\%} \tag{12.3}$$

$$\lambda_i = \lambda \frac{K_i W_i\%}{\sum_i \lambda_{i_{\text{nn}}}} \tag{12.4}$$

Table 12.2: Failure rate per subsystem

Subsystem	Mass [g]	W [%]	K_i	$\lambda_{i_{\text{nn}}}$	λ_i
Structures	174	9.2	2.6	25	0.1
Propulsion	444	23.4	1.3	58	0.2
Battery	1065	56.0	2.8	103	1.0
Payload	218	11.5	3.2	63	0.2

Since the top-down method is used, the failure rate per subsystem sums up to 1.5. In the future, a more detailed analysis can be used where more subsystems and more failure rates are taken into account for better failure rate estimations.

Availability

This parameter is of utmost importance for systems that need to be deployable at any time. It measures the number of times when the system is available or ready to deploy with respect to the number of times in which the system is required. The drone has to have a high availability, since it ought to adhere to requirement XXX, claiming that the drone has to be operational 99% of all times. Furthermore, taking into account weather conditions according to requirement REQ-STK11. To achieve this, the MTBF and the Mean Time To Repair (MTTR) should be calculated for each subsystem. MTTR represents the time needed for repairs. At the mission site, repairs may not be feasible since some damaged subsystems requiqre components to be shipped. This negatively impacts its availability in case this happens. Table 12.3 summarizes the estimated hours for each subsystem and the overall availability. This is calculated using Equation 12.5.

$$Availability = \frac{MTBF}{MTBF + MTTR} \cdot 100\% \tag{12.5}$$

Table 12.3: Availability of subsystems

Subsystem	MTBF (hrs)	MTTR (hrs)	Availability [%]
Structures	700	2	99.7
Propulsion	600	3	99.5
Battery	400	2	99.5
Payload	500	1	99.8
Total			**98.5**

To maintain safe operation, all subsystems must function properly. If one fails, Fire-Eye cannot operate. However, spare components can be carried along to enhance availability. For instance, extra propellors, camera, and lenses can be swapped if needed. Other components, such as the rotor, FC and structural damages may not be viable which require advanced tools to repair. Overall system availability is determined by multiplying the availability values of each subsystem which results in a total availability of 98.5% for Fire-Eye. While carrying spare parts for each subsystem could provide nearly 100% availability, it would also increase hardware costs. Ultimately it is up to the user to decide which spare parts are worth to bring to the mission site.

Maintainability

In quadcopter design, maintainability refers to the likelihood that a component can be kept in, or returned to, an operational state within a defined period. A widely accepted metric to assess this is Maintenance Man Hours per Flight Hour (MMH/FH) which represents the labor hours spent on maintenance relative to the flight time. This is estimated at the system level using Equation 12.6.

$$\text{MMH/FH} = \frac{1}{6} \cdot \text{IRM} \cdot \text{CDTM} \cdot \text{IC} \cdot \text{IA} \cdot \text{MEW}^{0.25} \tag{12.6}$$

Where IRM is Maintenance Role Index which is standard set at 1.5 for commercial quadcopters and CDTM is the Design to Maintain Coefficient which reflects the maintainability during the design phase derived from statistical data. According to [42], CDTM can be estimated based on the extent of maintenance considered in the design process. However, no realastic values were to be found. Therefore, a more intensive subsystem analysis has to be performed to estimate the MMH/FH.

Maintenance checks

Regular preventative maintenance is essential as some parts of the system need more frequent checks than other. This is either because they are more likely to fail or because they play a key role in the quadcopters functionality. In Table 12.4, maintenance tasks are divided into three categories: high, medium, and low frequency. High-frequency tasks are done in between every mission, medium ones every week, and low-frequency tasks about once a month.

Table 12.4: Frequency of maintenance task per subsystem

Subsystem	Maintenance Task	Frequency
Motors	Lubrication	Medium
	Check waterproof seals	Medium
	Inspect for damage	High
	Perform benchmark tests	Low
	Inspect for corrosion	Medium
Camera & Sensor	Clean lens	High
	Clean sensor	High
	Calibrate system	Medium
Sensor System	Calibrate system	Medium
	Perform benchmark tests	Low
	Inspect for damage	High
Propellers	Inspect for damage	High
	Tighten bolts	Low
Structure	Inspect for damage	High
	Check waterproof seals	Medium
Batteries	Recharge battery	High
	Perform benchmark tests	Low
Flight Control System	Calibrate system	High
	Perform benchmark tests	Low
UV LED System	Inspect for damage	High
	Clean LEDs	High
Cabling	Inspect connections	Low

In most cases, high-frequency maintenance focuses on the exterior of the quadcopter, where basic visual checks and quick tasks can be completed. This ought to be done during the turnaround time. However, medium and low-frequency maintenance involves disassembling the quadcopter and working on more complex internal components which require extended time and effort.

Safety

Due to the densely populated areas in which the mission takes place, safety is of high importance and has been carefully considered throughout the entire design process. Since the quadcopter is unmanned, no onboard operator is required, unlike in helicopters. This reduces the risk to human life significantly. Nevertheless, additional measures have been implemented to ensure safety on the ground and around the mission perimeter.

In the following chapter, Chapter 13, a comprehensive Technical Risk Assessment is conducted and mitigation strategies are established into the design process which enhances both safety and reliability.

Furthermore, routine maintenance and redundancies help minimize the risk of failure which ensures that the quadcopter remains safe even if a component fails. For instance, if the signal is lost, the quadcopter will attempt to restore the data link. If it fails to do so, it will automatically land after 60 seconds to allow for future retrieval and to prevent potential harm to the environment. This is specified as TR-MIS-NAV-04 in Table 13.4.

13 - Technical Risk Assessment

Effective risk management is essential to ensuring the reliability and resilience of any complex system. This chapter outlines the key technical risks that may affect the system and describes how they will be managed. Section 13.1 identifies and categorizes the risks, including newly identified risks added during the most recent system review. This is followed by an assessment of their likelihood and impact in Section 13.2. Section 13.3 presents the initial risk maps, and Section 13.4 details the mitigation strategies along with an updated risk map incorporating the new risks.

13.1. Risk Identification

Defining risks is a vital phase of design. This way, one can account for possible mishaps and setbacks and minimize their occurrence and influence. To formulate risks, different phases of the system deployment were defined and ordered. Furthermore, the mission risks were organized by subsystem. The risks have been assigned an identifier related to a phase and/or subsystem, which can be seen in Table 13.1.

Table 13.1: Identifiers of Risk Definitions

Phase / Subphase	ID Prefix
Manufacturing	MFG
Assembly, Integration and Testing	AIT
Commission	COM
Mission	MIS
Maintenance	MNT
End of Life	EOL

Subsystem	ID Prefix
Forensics	MIS-UV
Material	MIS-MAT
Frame	MIS-FRM
Battery	MIS-BAT
Navigations	MIS-NAV
Mapping	MIS-MAP
Communications	MIS-CMS
Propulsion	MIS-PROP
Control	MIS-CTRL
Environment	MIS-ENV

After the risks have been identified and assigned unique identifiers, their consequences are assessed. Each risk is assigned to a specific project member, who is primarily responsible for managing and mitigating it. Risks that have been documented in previous reports [3] are excluded from this section to avoid redundancy. Therefore, only the newly identified risks, along with their associated consequences and responsible team members, are presented in Table 13.2.

Table 13.2: Technical Risk Definitions added since Midterm Report [4]

ID	Risk	Consequence	Responsible Person
	Manufacturing		
TR-MFG-02	Incorrect materials used due to supplier error	Reduced structural integrity, increased mass, system failure	MW
TR-MFG-03	Tooling/machine malfunction during production	Delays in part production and possible quality issues	ND
	AIT		
TR-AIT-02	Improper wiring or cable routing during assembly	Short circuits, signal interference, or degraded sensor performance	AA
TR-AIT-03	Calibration errors during integration	Subsystem performance degrades or is inaccurate	ND

Table 13.2: Technical Risk Definitions added since Midterm Report [4]

ID	Risk	Consequence	Responsible Person
	Mission		
	Forensics		
TR-MIS-UV-09	Operator misinterprets UV data	Missed human remains or false positives	NK
TR-MIS-UV-10	Landing gear obstructs UV light or camera	Missed human remains	JS
	Energy Source		
TR-MIS-BAT-05	Battery connector loose or disconnects during operation	Power loss leading to crash	AA
	Navigation		
TR-MIS-NAV-04	RF signal blocked	Incorrect navigation or systemcrash	DM
	Communications		
TR-MIS-CMS-07	Data intercepted or jammed	Mission hijacked or data lost	DM
	Control		
TR-MIS-CTRL-04	Control signal interference from nearby devices	Loss of control or erratic behavior	OB
	Environment		
TR-MIS-ENV-01	Toxic or corrosive air	Performance degradation	ND
TR-MIS-ENV-02	Environmental collapse during flight	Total system loss, scene becomes hazardous, areas already covered change significantly	MW
TR-MIS-ENV-03	System contaminates the scene	Evidence invalidated	NZ
	End-of-life		
TR-EOL-02	No disposal plan for hazardous components (e.g., batteries)	Environmental or regulatory issues	MW

13.2. Assigning Probability and Impact

To figure out which risks are of most importance, each risk is assigned a score from one to five for both probability and impact. The definitions can be found in Table 13.3.

Table 13.3: Ranking System for Probabiltiy and Impact

Score	Degree of probability	Degree of impact
1	Rare: Very unlikely to occur	Negligible: minimal to no impact
2	Unlikely: Minor chance of occurence	Low: minor inconvenience, should not noticably affect mission
3	Possible: Might happen	Moderate: Noticiable impact on system and mission
4	Likely - Likely to happen at least once during lifetime	Significant: Major impact, system will likely not meet mission goal
5	Almost certain - Expected to happen more than once during lifetime	Critical: Mission fails, and severe damage is done to system or site

Method

To obtain consistent and unbiased estimates of the risk values, a method has been devised. Firstly, two people will individually assign values for both probability and impact to each of the risks. A third party will be asked to do the same for the risks that fall under their subsystem. For example, the power systems engineer was asked to evaluate the scores for all risks concerning the battery. After all three parties have assigned the risks, the average value will be taken and rounded to the nearest integer. After both scores have been assigned, the numbers will be multiplied to get a total risk score. The higher the risk score, the more important it is to take this risk into account.

13.3. Risk Map

The risks are ordered in a risk map, where the x-axis represents impact and the y-axis represents probability. The more important the risk, the closer it will be to the top right. The assigned risk values for each of the risks in Table 13.2 are presented in Figure 13.1.

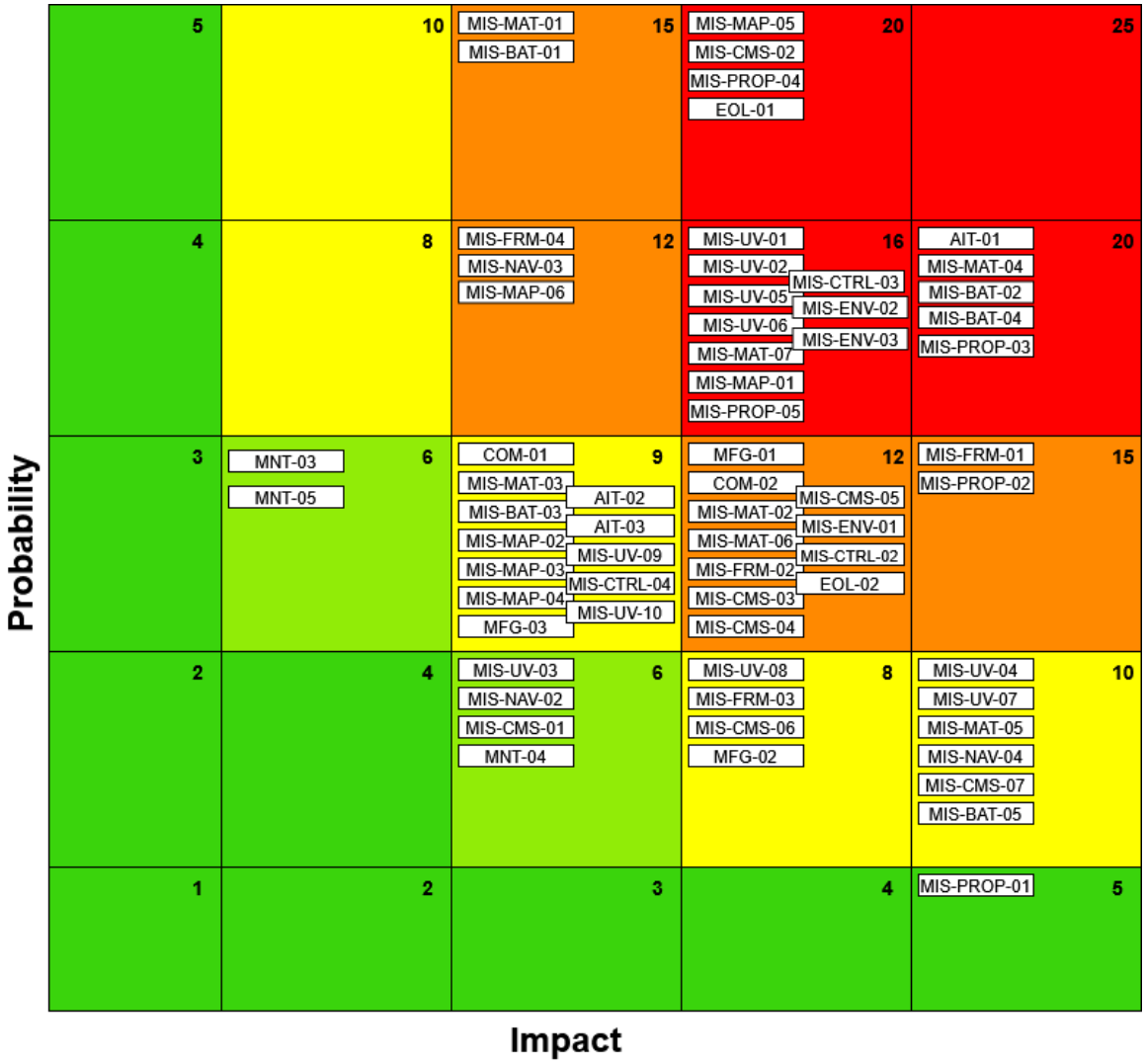

Figure 13.1: Pre-Mitigation Risk Map

13.4. Mitigation and Contingency Plans

As can be seen in Figure 13.1, many of the risks lie in the red, orange and yellow areas of the risk map. These risks are considered severe enough to necessitate a mitigation strategy to reduce their probability of occurrence, and a contingency plan for what to do should they occur.

The mitigation strategies and contingency plans for the newly identified risks are presented in Table 13.4.

This results in an updated score for probability and impact. The method used to assign the new probability and impact scores is the same as described in Section 13.2. It is important to note that the participants could not see the pre-mitigation scores to ensure that the scores did not artificially decrease.

Table 13.4: Mitigation and Contingency Strategies

ID	Mitigation	New probability	Contingency	New impact
TR-MFG-02	Perform incoming material inspection	1	Replace parts with verified material	2
TR-MFG-03	Inspect and maintain tools regularly; have backups available	1	Outsource to alternate supplier or manufacturer	2
TR-AIT-02	Use cable management standards, perform system-level electrical checks	2	Diagnose and rewire faulty components	2
TR-AIT-03	Use automated or guided calibration procedures	1	Recalibrate and revalidate affected systems	1
TR-MIS-UV-09	Provide clear user interface	2	Cross-reference with other data types (visual)	2
TR-MIS-UV-10	Consider camera field of view when designing landing gears	1	Change flight path to cover previously obstructed areas	3
TR-MIS-BAT-05	Use secure locking connectors, add strain relief	2	Replace connectors	3
TR-MIS-NAV-04	Include inertial navigation backup	1	Hover in place; auto-land if link not restored within 60 seconds.	2
TR-MIS-CMS-07	Encrypt communications and storage	1	Use a 'kill switch'	3
TR-MIS-CTRL-04	Use shielded components and select interference-resistant frequencies	2	Reconnect manually or initiate failsafe mode	2
TR-MIS-ENV-01	Seal openings well	2	Decontaminate the system after mission	2
TR-MIS-ENV-02	Coordinate with emergency services for risk status	2	Pull out UAS or go to non-critical area	2
TR-MIS-ENV-03	Ensure system is cleaned before mission	2	Notify forensic team and flag potentially compromised areas	3
TR-EOL-02	Develop a battery disposal/recycling protocol	1	Work with certified waste handlers	2

Post Mitigation and Contingency Risk Map

Now that the scores have been updated, a new risk map can be generated. The risk map can be found in Figure 13.2.

As can be seen in Figure 13.2, most risks have been moved into low-risk areas. The exception here is **TR-MIS-PROP-04**. Even with the mitigation and contingency strategies, it still ends up in an orange area. This indicates that the risk is still considered moderate and requires continued attention.

The primary contributor to this residual risk is the downwash effect, which, although reduced compared to the initial design discussed in the midterm report [4], still presents a concern. In the current configuration, the downwash is significantly lower, making the situation more manageable. Further strategies for minimizing downwash and its impact are presented in Chapter 9. These approaches are

expected to help reduce the risk associated with **TR-MIS-PROP-04** even further, potentially bringing it into a lower risk category in future assessments.

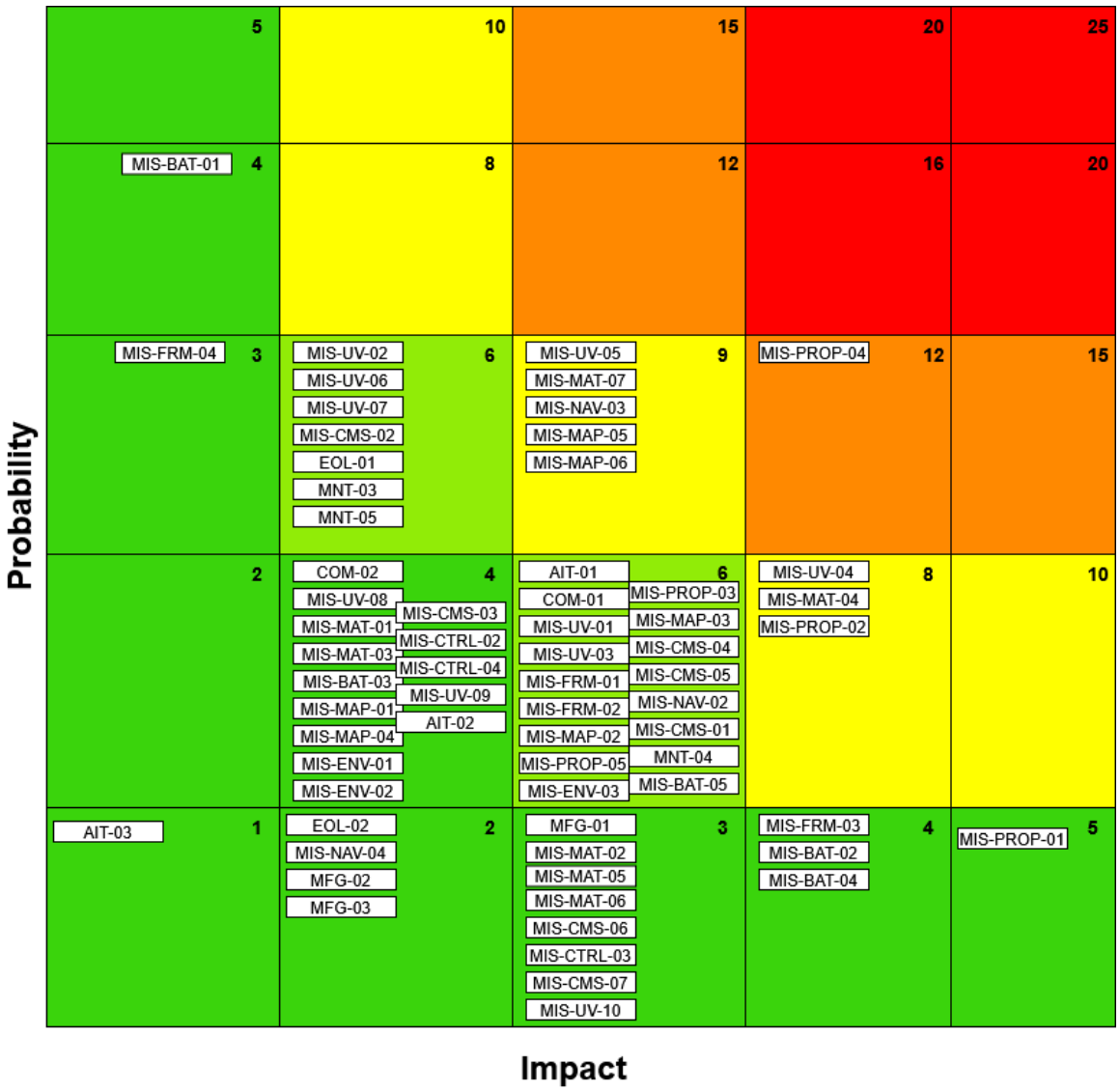

Figure 13.2: Post-Mitigation Risk Map

14 - Sustainability Approach Strategy

Sustainability was a constant presence in the design process, and was evaluated continuously. Building on what has been stated in the Project Plan [1], the Baseline Report [3] and the Midterm Report [4], this chapter aims to reemphasize the sustainability goals, their importance, and order of importance. Furthermore, the design will be evaluated, and steps that should be taken in the post-DSE phases of the design will be outlined.

14.1. Sustainability Approach

As was mentioned in the Baseline Report [3], the sustainability approach for Fire-Eye is divided into three focus points: Environmental Sustainability, Social Sustainability and Economic Sustainability. For further elaboration on each point and the associated goals, refer to [3].

Order of prioritization

It was determined that the measures in the sustainability approach will only be taken where requirements can still be met. In addition, certain criteria related to sustainability were prioritized over others, as they have an associated formal requirement. These are the recyclability (**REQ-STK12**), ease of use (**REQ-STK14**) and the unit cost (**REQ-STK13**).

This was reflected in the trade-off to select the design configuration [4]. Sustainability and Cost accounted for 15% and 10% respectively. Furthermore, the ease of use requirement was accounted for in the complexity sub-criteria of the safety criteria. In total, the total weight of all the criteria related to sustainability was 34% of the total weight. This is in line with the aforementioned philosophy of not compromising on the design functionality, while still taking sustainability into account.

14.2. Sustainability of Design

This section details how Fire-Eye meets key sustainability requirements, focusing on material recyclability, power subsystem challenges, and design principles that promote repairability, upgradeability, and energy efficiency. Through these approaches, Fire-Eye aims to balance rigorous functional demands with responsible resource management.

Material Recyclability: Fire-Eye's design addresses material recyclability to meet **REQ-STK12** (75% recyclability by weight, excluding payload) through strategic material selection, modular architecture, and end-of-life planning. The system prioritizes materials with well established recycling pathways to balance performance and recyclability effectively. An overview of the sustainability and recyclability approach for the different structural components and materials selected can be found in Table 14.1:

Table 14.1: Material Specifications, Recyclability, and Key Technical Challenges

Component	Material	Recyclability	Key Challenges
Propeller Arms	Polyetheretherketone with 30% carbon fiber (PEEK-CF30)	The thermoplastic nature of the PEEK matrix allows it to be remelted repeatedly at temperatures around 341°C[1]. Furthermore, pyrolytic recovery processes can retain up to around 80% of the original fiber tensile strength [44].	Recycling is energy intensive and may cause some fiber damage.

[1]URL: https://prod1-plate-attachments.s3.amazonaws.com/attachments/721abf1b07/Multiplast_PEEK_CF30.pdf [Cited 17/06/2025]

Table 14.1: Material Specifications, Recyclability, and Key Technical Challenges

Component	Material	Recyclability	Key Challenges
Body Frame	Polycarbonate (PC)	PC is a thermoplastic polymer that is recyclable through mechanical processes such as shredding and remelting, with very small effects on its properties[2].	Susceptible to UV degradation and yellowing over time; mechanical properties can decline with repeated recycling. Contamination can affect recyclability and melt consistency.
Landing Legs	Epoxy matrix with T700 carbon fibers (CFRP)	Recycling of thermoset-based CFRP is limited due to its non-melting matrix. Among available methods, chemical solvolysis has shown promise for fiber recovery without significant morphological degradation. Allows for partial recovery of carbon fibers, with overall decomposition efficiency around 90%. In optimal cases, over 70% of original tensile strength was retained [45].	Solvolysis requires careful solvent handling and may weaken fibers.
Propeller Blades	Glass fiber reinforced polymer (GFRP)	GFRP can be thermally decomposed, allowing partial recovery of glass fibers. However, due to changes in fiber morphology and degradation of material properties during recycling, the recovered fibers generally have reduced mechanical integrity. Consequently, recyclate is better suited for lower-grade, non-structural uses rather than direct structural applications [46].	Material strength is reduced and emissions can occur during processing.
Fasteners	Aluminum	Aluminum is highly recyclable via conventional smelting processes, with recovery rates reaching up to 95%. It exhibits no quality loss through repeated recycling[3].	Recycling requires significant energy and proper material separation.

Power Subsystem Recyclability: Batteries present one of the most significant challenges to recyclability in the Fire-Eye system. With the battery accounting for approximately 47% of the total system mass, achieving the overall 75% recyclability target becomes effectively impossible. While this is far from ideal, alternative end-of-life strategies can help reduce the environmental impact of the batteries.

Once the batteries have degraded to the point where they are no longer suitable for use in Fire-Eye, they may still hold sufficient capacity for lower energy applications. This would make them viable for reuse in less demanding systems, extending their functional lifetime, and delaying disposal. Moreover, this secondary use can reduce the demand for new batteries in those applications, contributing further to resource efficiency. It must be mentioned that while this does lower the environmental impact of the batteries, they must still eventually be disposed of.

Although LiPo batteries are technically recyclable, current recycling processes are underdeveloped

[2]URL: https://www.aboutpolycarbonate.com/wp-content/uploads/2024/06/Polycarbonate_Circularity-1.pdf [Cited 17/06/2025]

[3]URL: https://en.wikipedia.org/wiki/Aluminium_recycling [Cited 17/06/2025]

and rarely implemented. As a result, Fire-Eye's battery cannot be meaningfully considered recyclable. Most end-of-life LiPo batteries are still discarded rather than processed, due to safety concerns, low material recovery, and high costs[4]. However, future advancements in battery technology, such as the ability to restore degraded batteries to their original capacity [47], could allow for possibly 100% of the battery to be reusable for high energy applications. Additionally, the size and expansion of the global EV market, and a growing shift towards more sustainable practices could result in an increase in research concerning the recyclability of batteries, which will serve to further decrease the environmental impact of Fire-Eye over time.

Motor Recyclability: Fire-Eye employs four XING 2814 880KV brushless motors [5], composed of several recyclable materials. The bell and base are manufactured from 7075 Aluminum; a high-strength, corrosion resistant alloy that is widely recycled [6].

Additional components include copper windings in the stator, steel shafting, and Japanese NSK 11×5×5 mm bearings. Copper and steel are readily recyclable[7] [8].

Furthermore, the use of set screws, rather than adhesives, and hex-bolt shafts improves disassembly potential. Motor wires are sheathed for durability, but this may slightly hinder material separation unless stripped.

While small motors are not often prioritized for individual recycling, their materials have high reuse value. Companies like Sims Metal Management are advancing the recovery of copper, aluminum, and steel from such units [9]. Moreover, motors in good condition could also be repurposed in non-critical or educational drone systems.

Design for Repairability and Upgradability: Where possible, a modular design was implemented to enable component replacement rather than full unit disposal, reducing waste and improving maintainability. This also allows for system upgrades without having to replace the entire quadcopter, which lowers material consumption in the long term.

In line with this goal, the mapping payload was designed to be fully removable, to allow for easy switching from mapping to forensic functionalities between flights. The UV payload, while not designed to be removable during the mission, will be attached simply so that it can be easily removed when in need of replacement.

Furthermore, the landing gear and quadcopter arms are attached in such a way that allows for removal and replacement if needed (see Chapter 7).

Lightweight Optimization: The energy consumption of Fire-Eye was reduced through careful design decisions aimed at minimizing system weight while still achieving mission objectives. An extensive component database was analyzed to identify the lightest effective combination of battery and motor that could meet the system's power and endurance requirements. Additionally, lightweight yet durable materials were selected for structural components such as the quadcopter arms and landing gear, further reducing overall required energy.

Energy Efficient Operation: Maintaining a high level of energy efficiency benefits Fire-Eye both operationally and environmentally. To reduce unnecessary energy consumption, payloads only operate when required. The mapping payload is only activated in regions that require mapping, while the UV system, which uses significant energy, is flashed intermittently based on mission needs. This strategy minimizes energy waste, extends mission duration, reduces thermal load, and supports sustainability goals by lowering the system's overall energy demand.

Minimal Scene Disturbance: Out of respect for victims and their families, attempts were made to minimize debris displacement by the system. It is important to preserve the sensitive forensic scenes Fire-Eye will investigate. However, given the time constraints, it has not yet been possible to guarantee

[4]URL: https://www.eaclubs.org/post/good-to-know-battery-recycling-developments-and-challenges [Cited 17/06/25]
[5]URL: https://rcdrone.top/products/iflight-xing-x2814-fpv-motor [Cited 17/06/2025]
[6]URL: https://ilfproducts.co.uk/7075-aluminium-alloy-eco-friendly-recycling/ [Cited 17/06/2025]
[7]URL: https://internationalcopper.org/resource/copper-recycling/ [Cited 17/06/2025]
[8]URL: https://www.rubicon.com/blog/steel-recycling/ [Cited 17/06/2025]
[9]URL: https://www.theenvironmentalblog.org/2024/10/electric-motor-recycling/ [Cited 17/06/25]

an acceptable level of scene disturbance. In the post-DSE phase of the design, further steps should be taken to minimize the downwash, as described in Section 9.6.

Inclusive Use Design: In line with **REQ-STK14**, system complexity has been kept to a minimum to guarantee ease of use for the operators with minimal training needed. This extends to the modular design. The different payloads are easy to replace and should not add an unacceptable level of complexity to the design.

Safe Materials and Manufacturing: Toxic composites, hazardous adhesives, etc. will be avoided in favor of materials with low health risk and exposure toxicity.

Affordability: The selected system components emphasize a balance between cost and performance. Commercial-off-the-shelf parts have been used where possible. Furthermore, the cost of the system is €36,000, which is well within the €50,000 limit set out in **REQ-STK13**.

Extended Product Lifetime: As described in the functional analysis (Appendix A), Fire-Eye will be inspected at the end of every mission for any signs of wear to identify potential failures before they occur. The use of five batteries also extends their lifetime as slow charging can be implemented[10]. This approach will extend the system's operational lifespan and reduce or prevent unexpected downtime. Additionally, the previously mentioned focus on upgradability and repairability ensures that individual components can be replaced or improved without needing to replace the entire system, reducing waste, lowering costs, and contributing to the system's long-term sustainability.

Sustainability Assessment

As previously mentioned, the 75% recyclability requirement (**REQ-STK12**) is not met by Fire-Eye. This is largely due to the battery making up approximately 52% of the total system mass excluding payload, as described above. The current system is approximately 34% recyclable by mass, excluding the forensic and mapping payloads. It is worth noting, however, that many of the system components currently considered non-recyclable have recyclable casings. These have been excluded as the exact mass of the component housing is not known. While this would likely only bring the recyclability percentage up a small amount, it is still worth separating and recycling these casings where possible to avoid unnecessary material waste.

A key contributor to this limitation is the use of a lithium polymer battery. While essential for energy density and performance, these batteries remain a major challenge for recyclability due to their complex chemistry, safety risks, and limited recycling infrastructure, as describe previously.

Despite this obstacle, the current recyclability of Fire-Eye excluding the battery remains relatively high at 69%, thanks to the use of recyclable metals and polymers with established recovery pathways. This partial recyclability supports resource conservation and reduces the environmental impact associated with manufacturing and disposal.

Understanding how important it is to improve battery sustainability, Fire-Eye's design focuses on ways to maximize battery lifespan, and then to reuse batteries in less demanding applications once they no longer meet full performance needs. It also looks ahead to future recycling technologies that could make battery recovery more practical. At the same time, the system uses components that are easy to repair and upgrade, helping to extend its overall lifespan. Together, these strategies help reduce the environmental impact throughout the drone's entire life cycle.

While falling short of the 75% recyclability goal is not ideal, it reflects current technological and industrial limitations in battery recycling rather than a neglect of sustainability principles. Advances in battery technology and recycling are expected to improve this situation in the future, allowing Fire-Eye and similar systems to better align with circular economy objectives. Moreover, in the post-DSE phase, more steps can be taken to improve on all aspects of sustainability.

Further Steps

While the design achieves important sustainability goals, several opportunities remain to enhance Fire-Eye's sustainability in the upcoming post-DSE phases, including the following:

[10]URL: https://www.ufinebattery.com/blog/how-to-slow-charge-a-lithium-ion-battery/ [Cited 24/06/2025]

- *Battery Technology Improvements:* As previously discussed, given that the battery represents a significant portion of Fire-Eye's total mass and presents a major challenge to recyclability, future development should focus on both improving end-of-life handling and adopting advanced battery technologies. This includes exploring emerging chemistries such as solid-state or silicon-anode batteries, which offer higher energy densities and improved recyclability [11], potentially reducing both system mass and environmental impact. In parallel, practical strategies should be developed for managing degraded LiPo batteries, such as establishing partnerships with secondary-use platforms or recycling initiatives, integrating modular battery chemistries for easier material recovery, and implementing comprehensive life cycle management plans that ensure safe disassembly, traceability, and reuse.
- *Advanced Recycling Partnerships:* Establish partnerships with specialized recycling facilities that handle thermoplastics composites and lithium polymer batteries, to maximize material recovery and minimize landfill waste.
- *Operational Procedures:* Develop guidelines for field operators on sustainable use practices, including battery reuse cycles, payload management, and maintenance protocols to extend product lifetime.
- *Downwash Minimization:* Minimizing downwash remains a key priority for Fire-Eye, particularly due to its impact on preserving the integrity of sensitive forensic scenes. As outlined in Section 9.6, further aerodynamic analysis, including propeller optimization, is necessary to reduce scene disturbance while maintaining operational effectiveness. Simulation and physical testing in controlled environments should be prioritized to evaluate and refine downwash behavior. This effort not only enhances technical performance but also supports social sustainability by respecting the forensic and emotional sensitivity of the environments in which Fire-Eye operates.
- *Supply Chain Sustainability:* Evaluate suppliers for environmental certifications and ethical practices to strengthen social and economic sustainability throughout the Fire-Eye supply chain.
- *Finalization of Inclusive Use Features:* To fully satisfy **REQ-STK14**, additional work should be done to refine the user interface and control systems to support intuitive operation by non-specialists. Human factors testing should be used to assess accessibility and ease of use, and a quick-reference operator guide and minimal training protocol should be developed based on feedback from test users.
- *Improved Lifecycle Monitoring:* Lifecycle monitoring shall be expanded to include real-time diagnostics, predictive maintenance based on usage, and a digital logbook to track system health across missions.
- *Validation of Component Modularization:* While the system is designed to be modular, further testing is needed to confirm the reliability of fasteners under repeated use, the compatibility of modules with future upgrades or substitutes, and the durability of interconnects under wear and vibration to ensure consistent performance.
- *Sustainability Reporting and Traceability:* To increase transparency and help future operators assess sustainability performance, a standardized reporting format should be developed. This would include a digital sustainability datasheet with each unit, traceability labels for key components detailing material origin and recyclability, and QR-coded maintenance logs and end-of-life guidance directly on the hardware.

Administrative Strategy

To continuously monitor our progress and check compliance with sustainability goals, sustainability will be a topic of discussion for each design decision. The sustainability officer will remain the main point of contact for the group if any issues related to sustainability come up. In addition, they will initiate conversations with the group if they deem it necessary.

Furthermore, in the post-DSE phases, dedicated tracking and evaluation of sustainability performance will continue. This includes monitoring implementation of recommended improvements, reassessing material choices, and validating end-of-life strategies. Maintaining this focus beyond the DSE

[11] URL: https://www.grepow.com/blog/what-is-a-silicon-anode-lithium-ion-battery.html [Cited 17/06/25]

stage is essential to uphold Fire-Eye's long-term sustainability commitments and adapt to emerging technologies or operational feedback.

15 - Production Plan

This chapter presents the Manufacturing, Assembly, and Integration (MAI) Plan developed for the Fire-Eye system. The purpose of the MAI Plan is to provide a clear, time-ordered outline of the steps required to transition from individual components to a fully assembled and operational product. It details the workflow necessary to realize the design in physical form, ensuring systematic construction, alignment with quality standards, and traceability throughout the production process.

The production plan is primarily illustrated by the flowchart presented in Figure 15.7, which outlines the sequence and interrelation of activities required to realize the complete Fire-Eye system. Three different main phases can be differentiated: Material Procurement, which refers to the step in the production process in which all the required materials, tools and components are sourced. Secondly, in the Fabrication Processes, the procured raw materials are transformed into specific system components through various manufacturing processes. Finally, the Assembly phase consists of integrating all subsystems and components into a fully functioning system. This includes both mechanical and electrical assembly.

Throughout all production stages, quality control and verification procedures are implemented to ensure compliance with design specifications and to maintain system reliability. These checks are critical to reduce downstream issues during integration and testing.

The first phase, Material Procurement (PP1), consists of three parallel activities: the acquisition of raw materials, commercially available subsystem components, and required manufacturing tools. The raw materials (PP1-1) refer primarily to the base materials needed or fabricating the system's structural components. These include various polymers, metals, and composite sheets (note Figure 15.1) identified during the design phase. On the other hand, the component procurement (PP1-2) covers all off-the-shelf items selected for the payload (Chapter 4), propulsion (Chapter 5), and power (Chapter 6)subsystems. This includes critical parts such as the battery, motors, propellers, electronic speed controllers (ESCs), as well as sensors, cameras, and computing units required for mapping, forensics, control, and navigation. Then, tool acquisition (PP1-3) involves preparing the equipment necessary for the upcoming fabrication processes. The tools identified include: CNC Lathe (HAAS ST-10) [1], Laser Cutter (Epilog) [2], FDM 3D Printer (Ultimaker S5)[3] and Hot plat welder (EXTOL Rapid Conductor 1015) [4]. These tools are essential for executing the manufacturing tasks described in the subsequent phase.

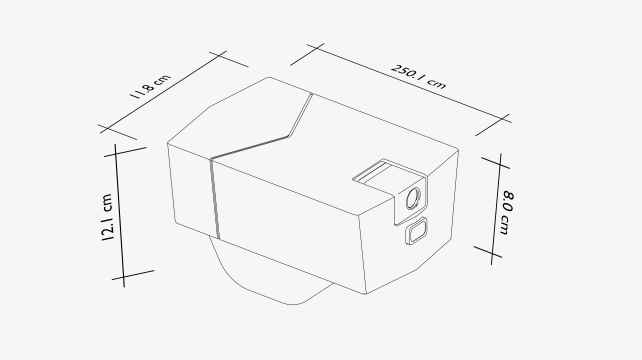

Figure 15.1: Overview of system´s bus dimension

Next, the Fabrication Process (PP2) can further be divided into fabrication of the propeller arms (PP2-1), landing gear struts (PP2-2), and hub skin (PP2-3). The propeller arms' manufacturing begins

[1]URL: https://www.haascnc.com/machines/lathes/st/models/standard/st-10.html [Cited 18/06/25]
[2]URL: https://www.epiloglaser.com/nl/ [Cited 18/06/25]
[3]URL: https://ultimaker.com/3d-printers/s-series/ultimaker-s5/ [Cited 18/06/25]
[4]URL: https://www.extolinc.com/technology/hot-plate-welding/rapid-conductor-specifications/ [Cited 18/06/25]

with preparing the PEEK material, which is then machined through CNC machining with mounting holes drilled at intervals as well. Laser cutting is then used to cut out the elliptical holes for the cooling system, after which the surface is treated through sanding and an anti-static coating. For the landing gear struts, carbon fiber is cut to size using a diamond-coated saw, and then bonded to 3D printed polycarbonate joints with epoxy. For the hub skin, the polycarbonate (PC) sheets are cut to size and their edges deburred. A mount of the removable LiDAR sensor can be 3D printed with hinges. A hot plate is then used for welding PC sheets together to form the bus. For post processing of the skin, acetone vapor is used for smoothing, followed by inserting EVA foam into the arm sockets for the arm joints. For each of these three subphases, quality control checks are conducted to ensure the fabricated parts are ready for assembly.

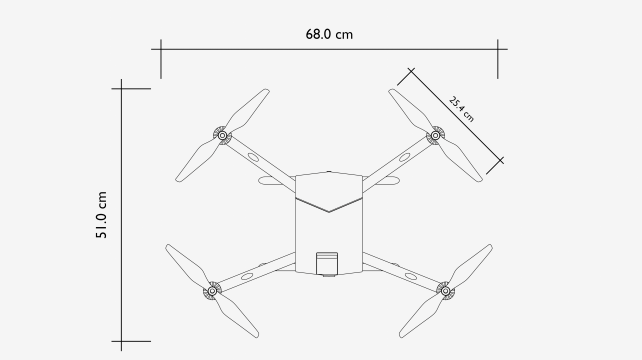

Figure 15.2: Top view of quadcopter layour

Finally, the Assembly phase (PP3) can begin using the manufactured and commercially available parts, ensuring the total size of the quadcopter remains within the constraints shown in Figure 15.2. Beginning with the power and propulsion subsystem (PP3-1), the motors are first attached to the individual arms. The propellers are then also attached to the motors themselves, and adjusted for clearance as per Figure 15.4. Next, the battery and ESC are attached to the hub interior as well. For the structural assembly (PP3-2), the propeller arms are then inserted into the hub sockets and secured with screws. Similarly, the landing gear can be bonded to the underside of the hub. These steps can be seen in Figure 15.3. Lastly, for mounting the payload and avionics (PP3-3), first the mapping system can be installed by first mounting the LiDAR sensor to a 3D printed bracket, which is then attached to the hub, as visible in Figure 15.6. The forensic system is installed, including the bandpass filter and NoIR. The control system assembly is then also be mounted and attached to the ESCs.

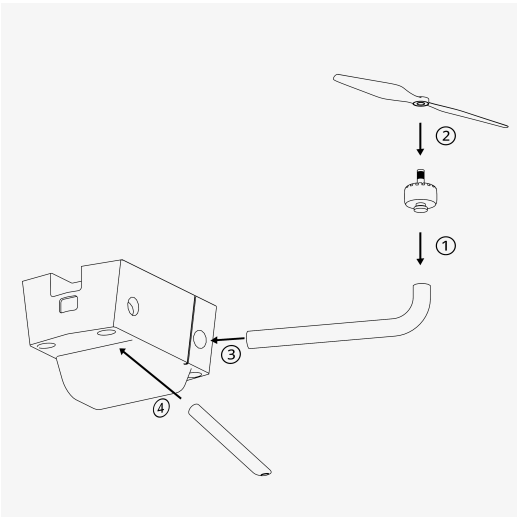

Figure 15.3: General overview of structural assembly steps

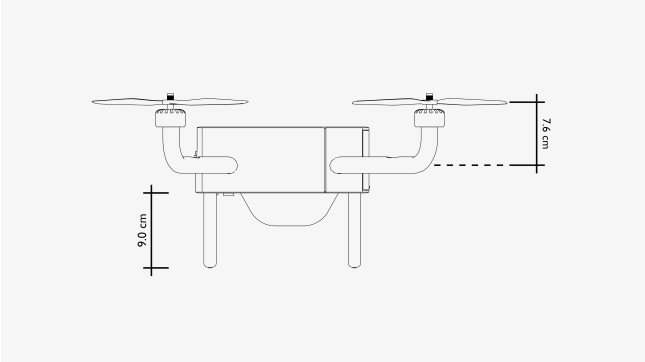

Figure 15.4: Visualization of propeller clearance

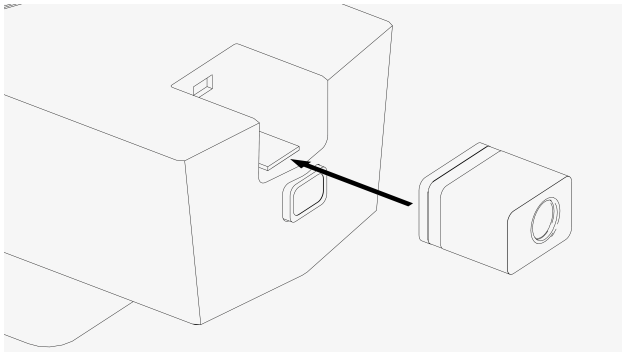

Figure 15.5: Visualization of LiDAR mounting onto bus

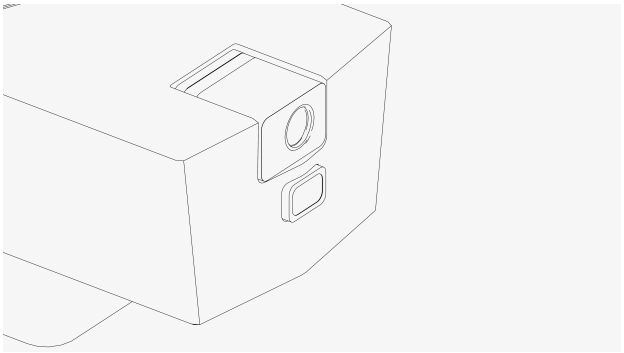

Figure 15.6: Visualization of LiDAR mounted onto bus

After the system has been assembled, a final round of quality assurance and control checks (PP4) is conducted to complete the production process. These checks include component level validation, as detailed in their respective sections: propulsion subsystem (Section 5.6), power subsystem (Section 6.5), and downwash verification (Section 9.4). Other checks involve calibration procedures for onboard cameras to ensure image accuracy and alignment and performance verification of the LiDAR system to confirm correct data acquisition and range accuracy.

Once all tests have been successfully passed, comprehensive documentation is compiled. This ensures traceability, supports future maintenance, and facilitates operational readiness of the final system.

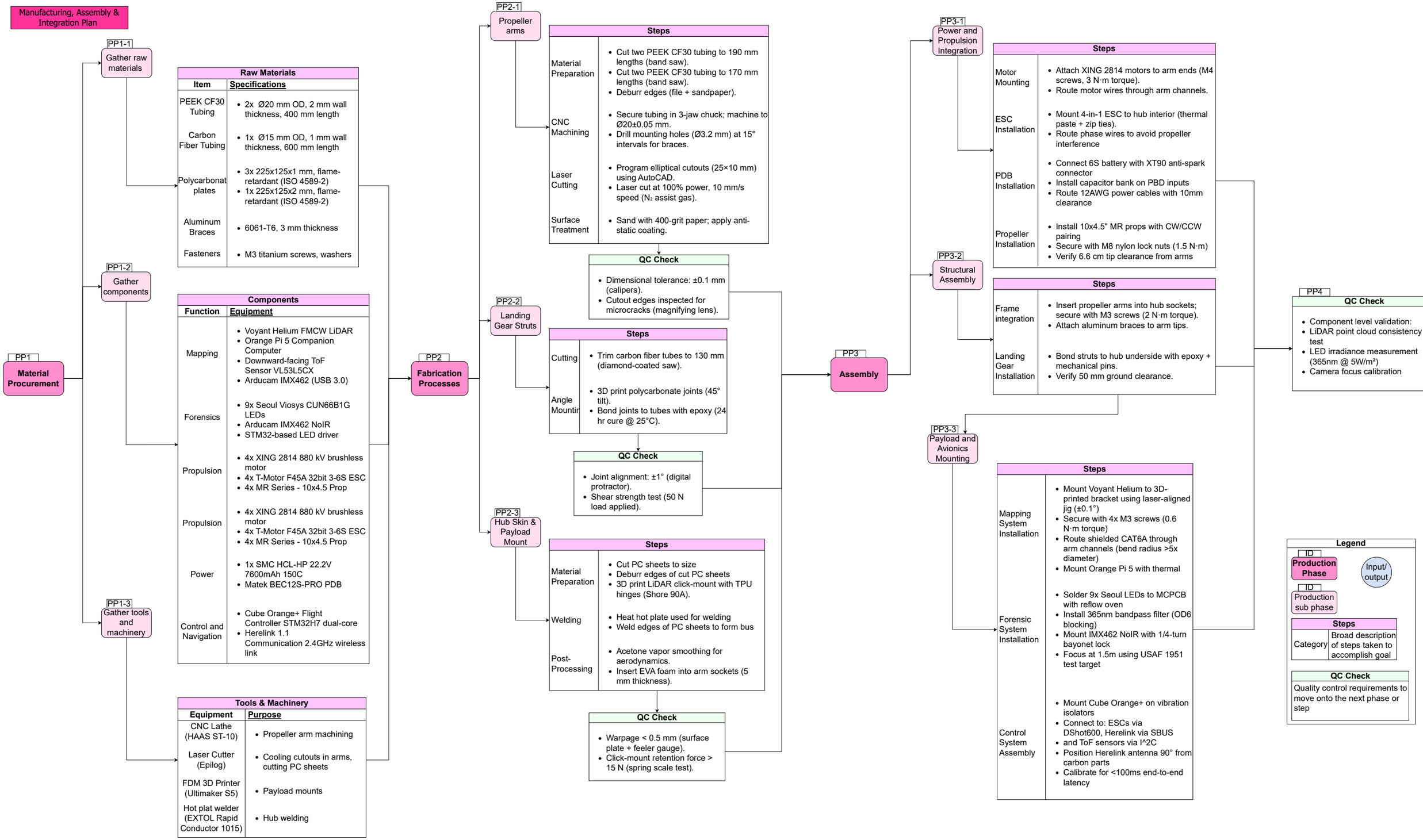

Figure 15.7: Flow of production steps required to assemble finished Fire-Eye system.

16 - Post DSE Phase

16.1. Project Design & Development Logic

The Project Design and Development Logic diagram describes all the steps required to design and develop the quadcopter for Fire-Eye. It highlights activities that will take place after the DSE has come to an end. This includes finalizing the design, prototyping, obtaining certifications, manufacturing, and sales & marketing. The system is an iterative process as depicted in Figure 16.1 with the associated feedback loops at the iteration checkpoints.

The process begins with the design phase, followed by prototyping and testing. Once the prototype successfully demonstrates the functionality of the quadcopter, the necessary documentation and certifications must be obtained from the EASA and ILT. Upon approval, a manufacturing plan and sales strategy can be developed in parallel. After final product testing and logistics planning, large-scale production can begin. The project's success can then be assessed based on customer satisfaction and sales performance.

16.2. Gantt Chart

In Figure 16.2, the post-DSE project Gantt chart is illustrated. While it follows from the PD&D, it shows the anticipated start and end dates of each phase along with their estimated durations. This chart provides an initial timeframe although it may be revised as the project progresses. To maintain clarity, the iteration loops are not shown.

16.3. Cost Breakdown Structure

The cost breakdown structure aims to show the contribution of post-DSE activities to the overall product cost, were Fire-Eye's development to continue. The Cost Breakdown Structure, CBS includes both recurring and non-recurring costs incurred throughout development and manufacturing. Operational and maintenance cost are not included in the CBS as these costs are incurred by the party operating the quadcopter and as such are not a factor in determining the unit cost. The estimation cost followed from the items in the CBS as shown in Figure 16.3, the development tree details the items that need to be performed before the product can enter into scale production, they are the non-recurring costs as once the development phase ends the product is finalized and changes are no longer necessary. Development items include finalizing the detailed design done by engineers, contributing to the design labor cost, performing product verification and validation tests as well as prototyping and the development of software used throughout the quadcopter[1]. It was estimated that a total of over €290,000 is needed to develop and finalize the Fire-Eye product. The majority of this cost is attributed to the finalization of this design which is estimated to take 10 full-time engineers 10 weeks[2]. The second highest contributor to the overall development cost is the testing of the product, this includes the verification and validation of the product, certification as well as prototyping[3]. The certification cost is likely an overestimation as EASA charges €23850 for the certification of a very light VTOL. VTOL's are classified as any heavier-than-air vehicle that can take-off vertically, whether drones are included in this not specified as they Fall under different CS regulations[4]. Production costs are recurring costs for each quadcopter and are divided into the cost of all components and the manufacturing cost to assemble the quadcopter as a whole. Table 16.1 shows the cost of each component. The system is sold with 5 batteries to allow batteries to be changed throughout the mission. This decreases downtime of the system as one battery can charge while another is in the system performing the mission. This preserves battery health as the batteries can be charged slower, decreasing the wear on the battery per cycle.

[1] URL: https://www.nationaleberoepengids.nl/salaris/software-developer [Cited 17/06/2025]
[2] URL: https://www.nationaleberoepengids.nl/salaris/ruimtevaart-engineer [Cited 17/06/2025]
[3] URL: https://design1st.com/how-much-do-hw-prototypes-cost/ [Cited 17/06/2025]
[4] URL: https://eur-lex.europa.eu/legal-content/EN/TXT/?uri=CELEX:32019R2153 [Cited 17/06/2025]

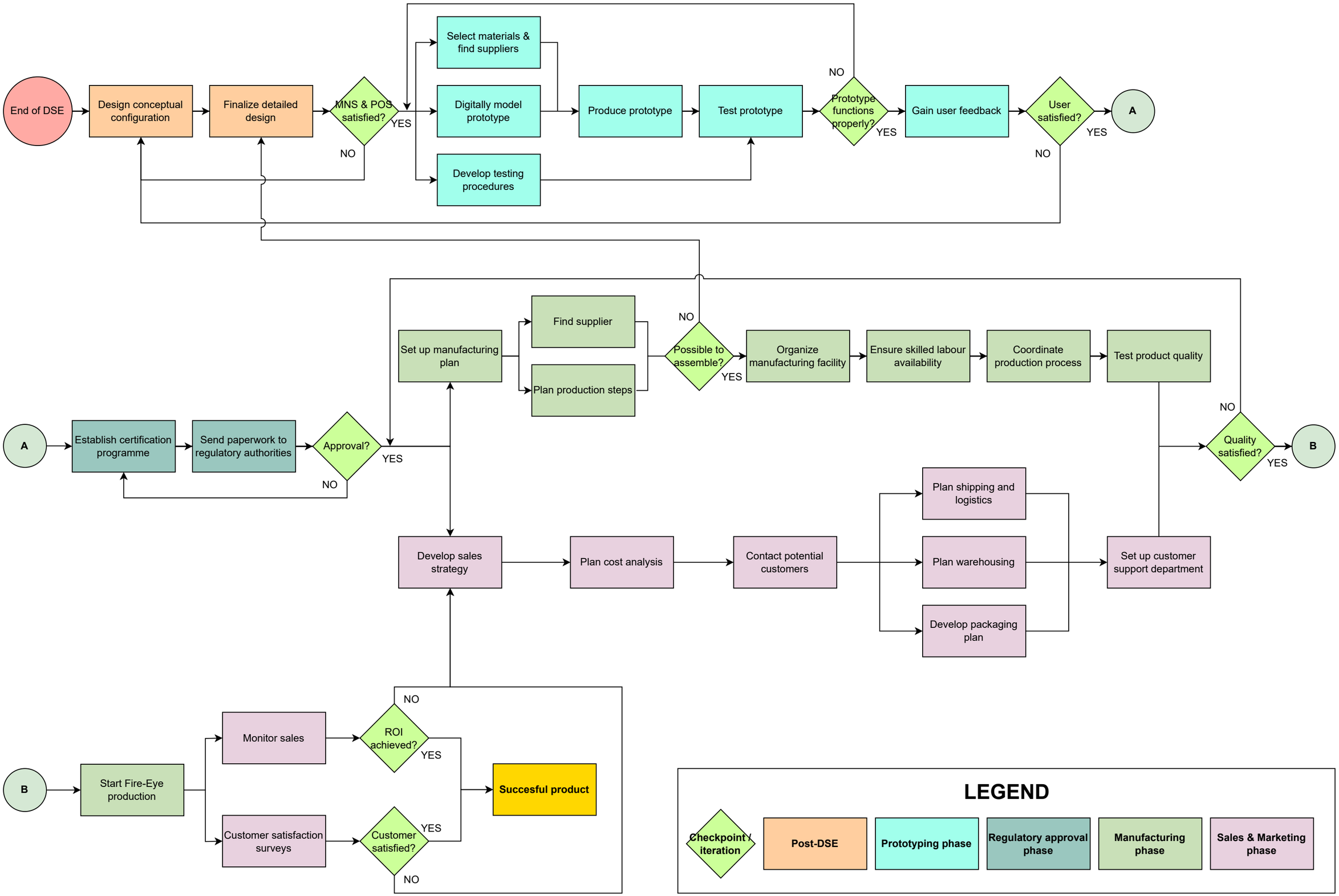

Figure 16.1: Project Design and Development Logic

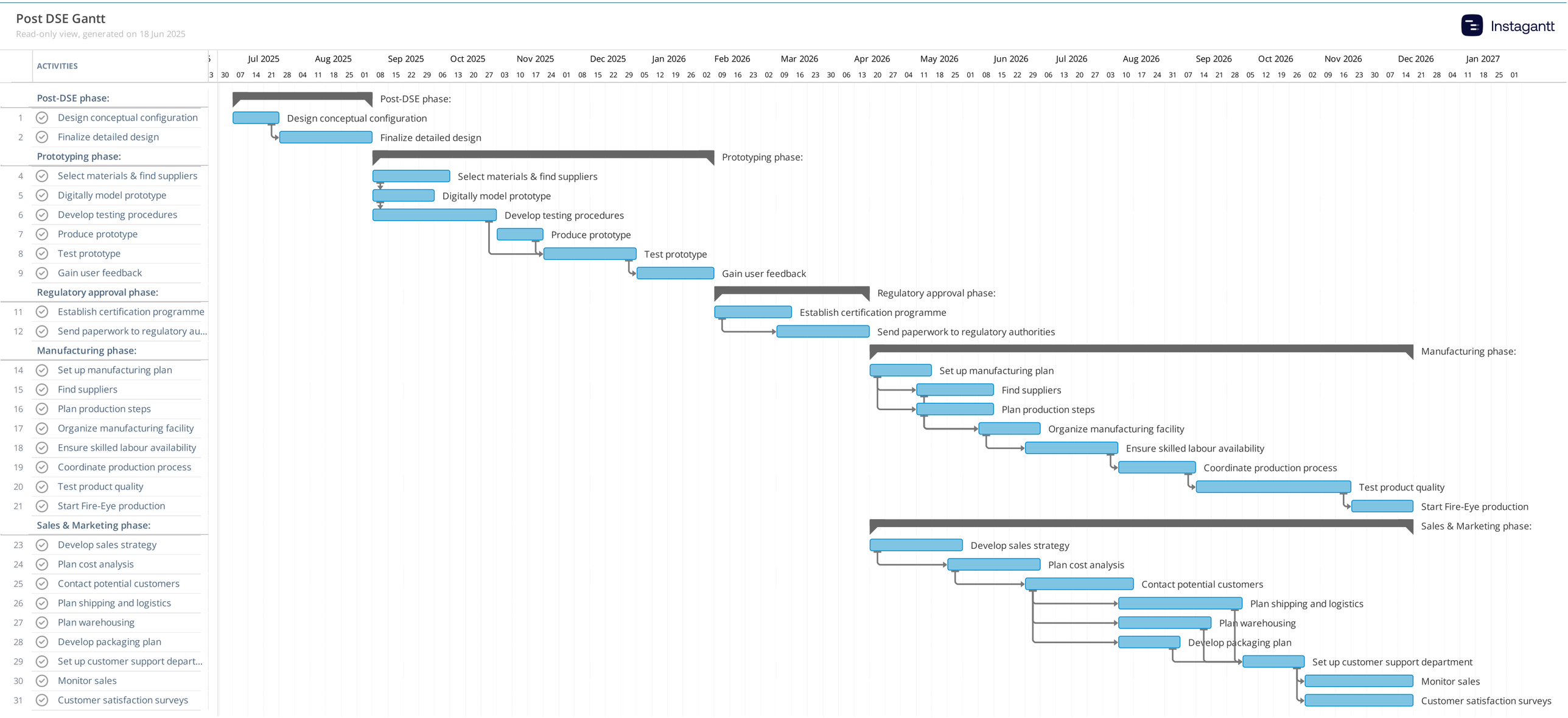

Figure 16.2: Post DSE Gantt Chart

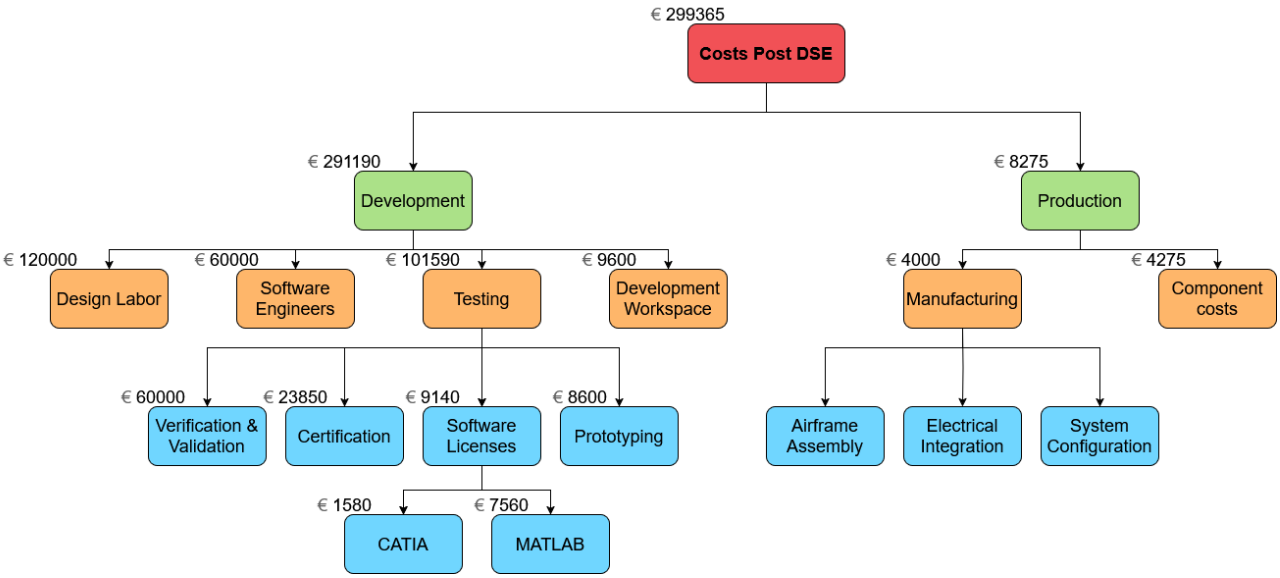

Figure 16.3: Cost breakdown structure [5] [6] [7]

Table 16.1: Payload Components cost in €

Component Name	Qty Needed	Unit Price (€)	Total Cost (€)
Voyant Carbon	1	1305	1305
Herelink 1.1	1	726	726
HCL-HP 22.2V 7600mAh 150C G10 Protection Plates	5	120	600
Step down DC-DC converter	1	6	6
PCB	1	5	5
Seoul Viosys CUN66B1G	10	4	40
2MP IMX462 Camera (1)	2	40	80
Orange Cube+	1	447	447
Orange Pi 5	1	250	250
Smart AP PDB	1	80	80
ToF for Cruise Speed	2	30	60
PDU BEC12S-PRO	1	27	27
ESC	4	33	132
XING 2814 Motor	4	39	156
Propellers	4	9	35
PEEK CF30 Material	1	200	200
Stepup DC-DC converter	1	5	5
Total			4275

As Chapter 3 explains, the target market of Fire-Eye is fire departments within the Netherlands. As there are 13 drone teams within the Dutch fire brigade the product will be priced such that if 10 drone teams purchase the Fire-Eye system the revenue will be break even, this corresponds to a unit cost of €36,400 [8]. Additional revenue from the other three drone teams can be used to expand into new markets within Europe, this results in €109,200 profit that can be used to expand into neighboring European countries.

[8] URL: https://www.brandweernederland.nl/onderwerpen/specialisme-team-digitale-verkenning-tdv/ [Cited 17/06/2025]

17 - Conclusion

Investigating a building where a fire has occurred is inherently challenging. For forensic purposes, it is essential that the scene is minimally disturbed, and the loss of structural integrity poses a threat to the safety of investigators. This drives the need for a system capable of mapping interiors and locating human remains in post-fire structures without human presence. Fire-Eye aims to satisfy this need.

Following a market analysis and thorough trade-off process in the Mid-term, a modular quadcopter configuration was identified as the optimal concept for the Fire-Eye mission. Building upon this concept, subsystems were refined and optimized to arrive at the detailed preliminary design. The purpose of this report was to describe and justify preliminary design of the Fire-Eye system.

The Fire-Eye systems features specialized payload elements for its mission. Its solid-state LiDAR sensor can generate 3D maps at a resolution below the 1 cm requirement, even in total darkness. The forensics subsystem combines a high efficiency UV light and a low-light camera, capable of detecting human remains while. The quadcopter's structure is lightweight yet sturdy, featuring high-performance materials such as carbon fiber and carbon-reinforced PEEK. Adopting an X-frame configuration, it can fit through any 70x70 cm entry, meaning it can enter scenes through doors and most windows. In the central hub, the subsystems are packed into a compact arrangement and encased in a skin, protecting electronics from hostile post-fire environments. A modular sensor mount allows operators to tailor the payload to the match mission's needs.

Performance analysis revealed that the system delivers a flight time of 15 minutes in its mapping configuration, with the forensic configuration slightly extending flight time. Additionally, the system was deemed to be stable in hover conditions in stability analysis. Further time should be spent improving the model, as the attitude control is not yet known. This is necessary in order to determine if the system is able to fly complex flight paths, which is crucial to the mission. A sensitivity analysis should be conducted as well, to further improve the controllability of the Fire-Eye.

Finally, it is important to mention the unit costs of the system. Including the engineering costs, cost of components and cost of manufacturing and assembly, the total unit cost is determined to be €36,000. With this unit cost, ten systems need to be sold to break even. Likely, the unit cost will change as the design matures even further. However, since the unit cost is well below the €50,000 required, it is not likely it will exceed this limit in the future.

However, there are some requirements that the design does not meet. Importantly, the downwash was deemed too high to be acceptable. The induced velocity exceeds 1.5 m/s at the flight altitude. Any velocity that is higher than this will displace dust and other particles. However, at this stage it is not known to what extend the downwash will interfere with the scene, as the speed at which certain evidence will be damaged or objects will be moved is currently unknown. Further research should be conducted into quantifying downwash in a more meaningful and intuitive way. Additionally, the system does not meet the recyclability requirement. The aim was to have 75% of the mass of the system be recyclable. Currently, the system sports a recyclability by mass of 34%. Note that these percentages do not include the payload. They do however include the battery, which accounts for 52% of the total system weight. This is the main reason the recyclability goal is not met, as the battery used is not deemed to be recyclable. If recyclability is to be improved, this is the first area that should be examined.

Moving forward, the design will be iterated further and eventually finalized. It is recommended that this will be done making use of experiments, as the validation of the performance parameters is not sufficient as of now. Special attention will be given to the disturbance and recyclability as these are the most critical area's of the design as it stands at the moment. Once the design is deemed to meet the requirements, the next phases will start. This will include prototyping, obtaining certifications, manufacturing and marketing. These phases themselves are still part of the iterative process, and the design could be revisited at each stage.

References

[1] Ameen, A., Brunner, O., Dahmen, D., Delnoij, N., Keating, N., Ma, D.-K., Sabel, J., Torreño Diez, H., Wassenaar, M., and Zaheer, N., "Project Plan: Fire-Eye," Tech. rep., Technical University Delft, Delft, 5 2025.

[2] Khan, W., and Nahon, M., "Development and Validation of a Propeller Slipstream Model for Unmanned Aerial Vehicles," *Journal of Aircraft*, Vol. 52, No. 6, 2015, pp. 1985–1994.

[3] Ameen, A., Brunner, O., Dahmen, D., Delnoij, N., Keating, N., Ma, D., Sabel, J., Torreño Diez, H., Wassenaar, M., and Zaheer, N., "Baseline Report: Fire-Eye," Tech. rep., Technical University Delft, Delft, 5 2025.

[4] Ameen, A., Brunner, O., Dahmen, D., Delnoij, N., Keating, N., Ma, D., Sabel, J., Torreño Diez, H., Wassenaar, M., and Zaheer, N., "Midterm Report: Fire-Eye," Tech. rep., Technical University Delft, Delft, 5 2025.

[5] Liu, Y., Kan, Z., Li, H., Gao, Y., Li, D., and Zhao, S., "Analysis and modeling of the aerodynamic ceiling effect on small-scale propellers with tilted angles," *Aerospace Science and Technology*, Vol. 147, 2024, p. 109038.

[6] Federal Emergency Management Agency, and United States Fire Administration, "FIREFIGHTER AUTOPSY PROTOCOL," Tech. rep., Federal Emergency Management Agency, 10 1994.

[7] Thompson, O. L., Russell, J. A., Stockman, S. K., Swall, J. L., and Simmons, T., "Assessing the effectiveness of alternate light sources in the search for skeletal remains," *Journal of Forensic Sciences*, 2025, pp. 1–8.

[8] "Perspective on the future of forensic science," Tech. rep., NFOA, 9 2023.

[9] Sharma, B., Chandra, G., and Mishra, V., "AICAI 2019 : 2019 Amity International Conference on Artificial Intelligence : proceedings : February 4-6, 2019, Amity University Dubai, Dubai International Academic City," *2019 Amity Inernational Conference on Artificial INtelligence (AICAI)*, 2019, pp. 824–827.

[10] Georgiou, A., Masters, P., Johnson, S., and Feetham, L., "UAV-assisted real-time evidence detection in outdoor crime scene investigations," , 5 2022.

[11] Kendall Martin, "Introducing Indoor Capture: Revolutionizing Large-Scale Indoor Data Capture | Skydio," , 5 2023.

[12] Surmann, H., Slomma, D., Grobelny, S., and Grafe, R., "Deployment of Aerial Robots after a major fire of an industrial hall with hazardous substances, a report," 2021.

[13] Blaga, S., "Autonomous Navigation for an Attitude-Stable Flapping Wing Air Vehicle Obstacle Avoidance Strategies Using Time-of-Flight Sensors," Tech. rep., Delft University of Technology, Delft, 4 2025.

[14] Davison, A. J., "Real-time simultaneous localisation and mapping with a single camera," *Proceedings of the IEEE International Conference on Computer Vision*, Vol. 2, 2003, pp. 1403–1410.

[15] Gupta, T., and Li, H., "Indoor mapping for Smart Cities-An affordable approach: Using kinect sensor and ZED stereo camera," *2017 International Conference on Indoor Positioning and Indoor Navigation, IPIN 2017*, Vol. 2017-January, 2017, pp. 1–8.

[16] Behroozpour, B., Sandborn, P. A., Wu, M. C., and Boser, B. E., "Lidar System Architectures and Circuits," *IEEE Communications Magazine*, Vol. 55, No. 10, 2017, pp. 135–142.

[17] Bachman, C. H., and Ellis, E. H., "Fluorescence of Bone," *Nature 1965 206:4991*, Vol. 206, No. 4991, 1965, pp. 1328–1331.

[18] Schut, E., Breedijk, R. M., Hilbers, M. F., Hink, M. A., Krap, T., Aalders, M. C., and Williams, R. M., "On the glow of cremated remains: long-lived green photo-luminescence of heat-treated human bones," *Photochemical and Photobiological Sciences*, Vol. 23, No. 9, 2024, pp. 1641–1657.

[19] Krap, T., Busscher, L., Oostra, R. J., Aalders, M. C., and Duijst, W., "Phosphorescence of thermally altered human bone," *International Journal of Legal Medicine*, Vol. 135, No. 3, 2021, pp. 1025–1034.

[20] Ljungkvist, E., and Thomsen, B., "Interpretation of a fire scene with ultraviolet light An assessment of the possible utilisation of ultraviolet light at fire scenes and subsequent recommendations for procedures," *Forensic Science International*, Vol. 297, 2019.

[21] Ye, H., Sau, K., Van Zeijl, H., Gielen, A. W., and Zhang, G., "A review of passive thermal management of LED module," , 1 2011.

[22] Gregory, N., and O'Reilly, C. L., "Low-Speed Aerodynamic Characteristics of NACA 0012 Aerofoil Section, including the Effects of Upper-Surface Roughness Simulating Hoar Frost," Tech. rep., N.P.L., 1970.

[23] Pérez Gordillo, A. M., Escobar, J. A., and Lopez Mejia, O. D., "Influence of the Reynolds Number on the Aerodynamic Performance of a Small Rotor," *Aerospace*, Vol. 10, No. 2, 2023.

[24] Dongre, A., Kadu, P., and Munghate, S., "Design of Modified Propeller for Crop and Vegetation Monitoring," *International Research Journal of Engineering and Technology*, 2020.

[25] Leclerc, M. A., Bass, J., Labbé, M., Dozois, D., Delisle, J., Rancourt, D., and Desbiens, A. L., "NetherDrone: a tethered and ducted propulsion multirotor drone for complex underground mining stope inspections," *Drone Systems and Applications*, Vol. 11, 2023, pp. 1–17.

[26] Dai, X., Quan, Q., Ren, J., and Cai, K.-Y., "Efficiency Optimization and Component Selection for Propulsion Systems of Electric Multicopters," *IEEE TRANSACTIONS ON INDUSTRIAL ELECTRONICS*, Vol. 66, No. 10, 2019.

[27] Bohorquez, F., Samuel, P., Sirohi, J., Pines, D., Rudd, L., and Perel, R., "Design, Analysis and Hover Performance of a Rotary Wing Micro Air Vehicle," *Journal of the American Helicopter Society*, 2003.

[28] Loenbaek, K., Bak, C., Madsen, J. I., and Dam, B., "Optimal relationship between power and design-driving loads for wind turbine rotors using 1-D models," *Wind Energ. Sci*, Vol. 5, 2020, pp. 155–170.

[29] Liu, J., and Zhou, F. M., "Structural Optimization of Frame of the Multi-Rotor Unmanned Aerial Vehicle through Computational Structural Analysis You may also like The Vibration Response of the Helicopter Coupling with Aircraft Gun," 2020.

[30] Megson, T., *Aircraft Structures for Engineering Students*, 7th ed., Butterworth-Heinemann, 2017.

[31] Hibbler, R., *Mechanics of Materials*, si ed., Vol. 10, Pearson Education Limited, 2018.

[32] TOKUTAKE, H., OKADA, S., SUNADA, S., TANABE, Y., and YONEZAWA, K., "On-board Downwash Speed Estimation of Drone Rotor-Based State Observer," *TRANSACTIONS OF THE JAPAN SOCIETY FOR AERONAUTICAL AND SPACE SCIENCES*, Vol. 65, No. 6, 2022, pp. 21–38.

[33] Adaika, Z., Boumehraz, M., and Mahmoudi, A., "Data-driven Diagnosis of Quadcopter Thrust Fault Using Supervised Learning with Airframe Vibration Signals," *2024 2nd International Conference on Electrical Engineering and Automatic Control, ICEEAC 2024*, Institute of Electrical and Electronics Engineers Inc., 2024.

[34] Beard, R. W., and McLain, T. W., *Small Unmanned Aircraft: Theory and Practice*, P R I N C E T O N U N I V E R S I T Y P R E S S, 2012.

[35] Hamill, G., and Kee, C., "Predicting axial velocity profiles within a diffusing marine propeller jet," *Ocean Engineering*, Vol. 124, 2016, pp. 104–112.

[36] Tan, R. , and Yüksel, Y., "Seabed scour induced by a propeller jet," *Ocean Engineering*, Vol. 160, 2018, pp. 132–142.

[37] Zainal, N. A., Nazar, R., Naganthran, K., and Pop, I., "Unsteady Separated Stagnation-Point Flow Past a Moving Plate with Suction Effect in Hybrid Nanofluid," *Mathematics 2022, Vol. 10, Page 1933*, Vol. 10, No. 11, 2022, p. 1933.

[38] Ko, J., and Lee, S., "Quantification of wake interaction effects on multi-rotor configurations in forward flight," *Aerospace Science and Technology*, Vol. 135, 2023, p. 108188.

[39] Barnes W. McCormick, *Aerodynamics, Aeronautics, and Flight Mechanics*, 1979.

[40] De Vries, H., Nguyen, T. T., and Veld, B., "Increasing the cycle life of lithium ion cells by partial state of charge cycling," *Microelectronics Reliability*, Vol. 55, 2015.

[41] "Grenfell Tower Inquiry," , 1 2021.

[42] Giovingo, D., and Corpino, S., "RAMS and Maintenance cost assessment in a Multidisciplinary Design Optimization environment," 2019.

[43] Petritoli, E., Leccese, F., and Ciani, L., "Reliability and Maintenance Analysis of Unmanned Aerial Vehicles," *Sensors (Basel, Switzerland)*, Vol. 18, No. 9, 2018, p. 3171.

[44] Pickering, S. J., "Recycling technologies for thermoset composite materials—current status," *Composites Part A: Applied Science and Manufacturing*, Vol. 37, No. 8, 2006, pp. 1206–1215.

[45] Vogiantzi, C., and Tserpes, K., "A Preliminary Investigation on a Water- and Acetone-Based Solvolysis Recycling Process for CFRPs," *Materials*, Vol. 17, No. 5, 2024.

[46] Tao, Y., Hadigheh, S. A., and Wei, Y., "Recycling of glass fibre reinforced polymer (GFRP) composite wastes in concrete: A critical review and cost benefit analysis," *Structures*, Vol. 53, 2023, pp. 1540–1556.

[47] Qiu, B., Zhou, Y., Liang, H., Zhang, M., Gu, K., Zeng, T., Zhou, Z., Wen, W., Miao, P., He, L., Xiao, Y., Burke, S., Liu, Z., and Meng, Y. S., "Negative thermal expansion and oxygen-redox electrochemistry," *Nature*, Vol. 640, No. 8060, 2025, pp. 941–946.

A - Functional Analysis

As described in the Baseline Report [3], one of the first steps in a design is to define the structure of the mission, and the functions it will perform.

A.1. Mission Architecture

The mission architecture was initially defined by analyzing all the groups necessary to complete the mission. These groups include: Air Segment, Control/Communications, Ground Segment, Subject, Mission Ops, and Development Segment. Each of these groups represents a distinct component or function necessary for mission success, and these were elaborated on in [3].

The mission architecture diagram in Figure A.1 shows the connections between the segments, illustrating a cohesive system of collaboration required to achieve mission success.

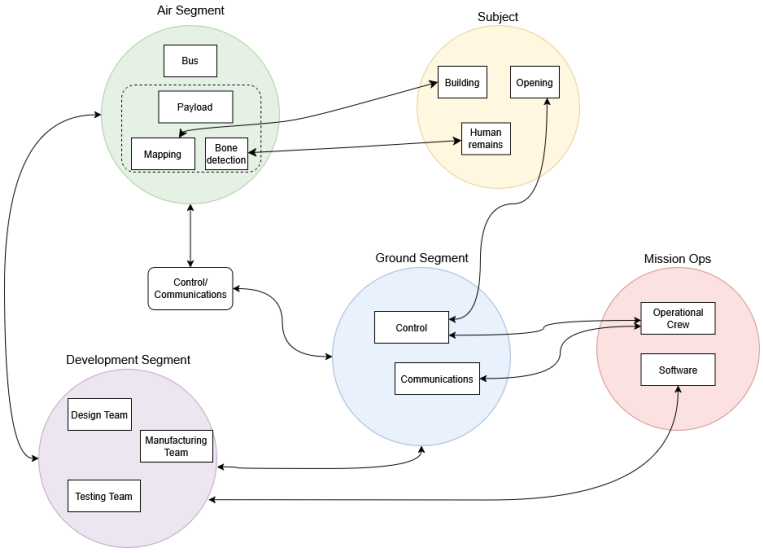

Figure A.1: Mission Architecture

A.2. Functional Flow Diagram

The Functional Flow Diagram (FFD) is a visual representation of the sequential and logical order of the decomposed functions of the system to visualize how different operations flow from start to finish. Each box represents a function, and arrows show dependencies.

The Functional Flow Diagram was used to help stakeholders understand system responsibilities, interdependencies, and control logic at each stage. It was also used to identify the desired capabilities of the mission and its systems, which were then translated into functional requirements.

The functional analysis began by defining the functions that describe everything the design should do. To define these functions up to a sufficient level of detail, several phases were determined, and further sub-phases and divisions were subsequently defined. The main phases included: Development, Certification/Regulatory approval, Manufacturing, Assembly, Integration & Testing (AIT), Commissioning, Pre-mission checks, Mission, Post-mission, Maintenance, Storage and End of Life; covering the full life cycle of the system. The mission phase was further broken down into sub-phases, including Take-off, Approach, Operation, Return and Landing. Note that phases, sub-phases and their components were colour-coded to facilitate diagram interpretation. For an in-depth explanation of each phase and sub-phase, see [3].

Furthermore, hardware components were assigned to each of the functions. The selection choice

was guided by user requirements, performance specifications, environmental constraints, and system integration compatibility. The resulting FFDs can be seen in Figure A.2 and Figure A.3.

A.3. Functional Breakdown Diagram

Whilst the FFD displayed the logical order of the flow of functions performed by systems, the Functional Breakdown Diagram (FBD) shows the unordered functions grouped by function packages. As can be seen in Figure A.4, the FBD is a hierarchical 'AND tree', by which the functions of all systems are subdivided.

The FBD was developed by organizing all functions from the FFD into more intuitive categories. After this, functions were divided into further sub-functions for a more detailed overview. Moreover, the hardware or general system responsible for each function was also defined, as well as a unique ID-numbering system that can be used to correlate the FBD and FFD together.

It should be noted that the categories, or 'function packages' in the FBD are *not* the same as the phases in the FFD. Instead, these function packages may group many similar functions or functions performed by similar systems/hardware together. The function packages were defined as follows: Development, Certification, Production & Integration, Commissioning, Main Mission, Stand-by, and End of Life. These packages were explained in [3].

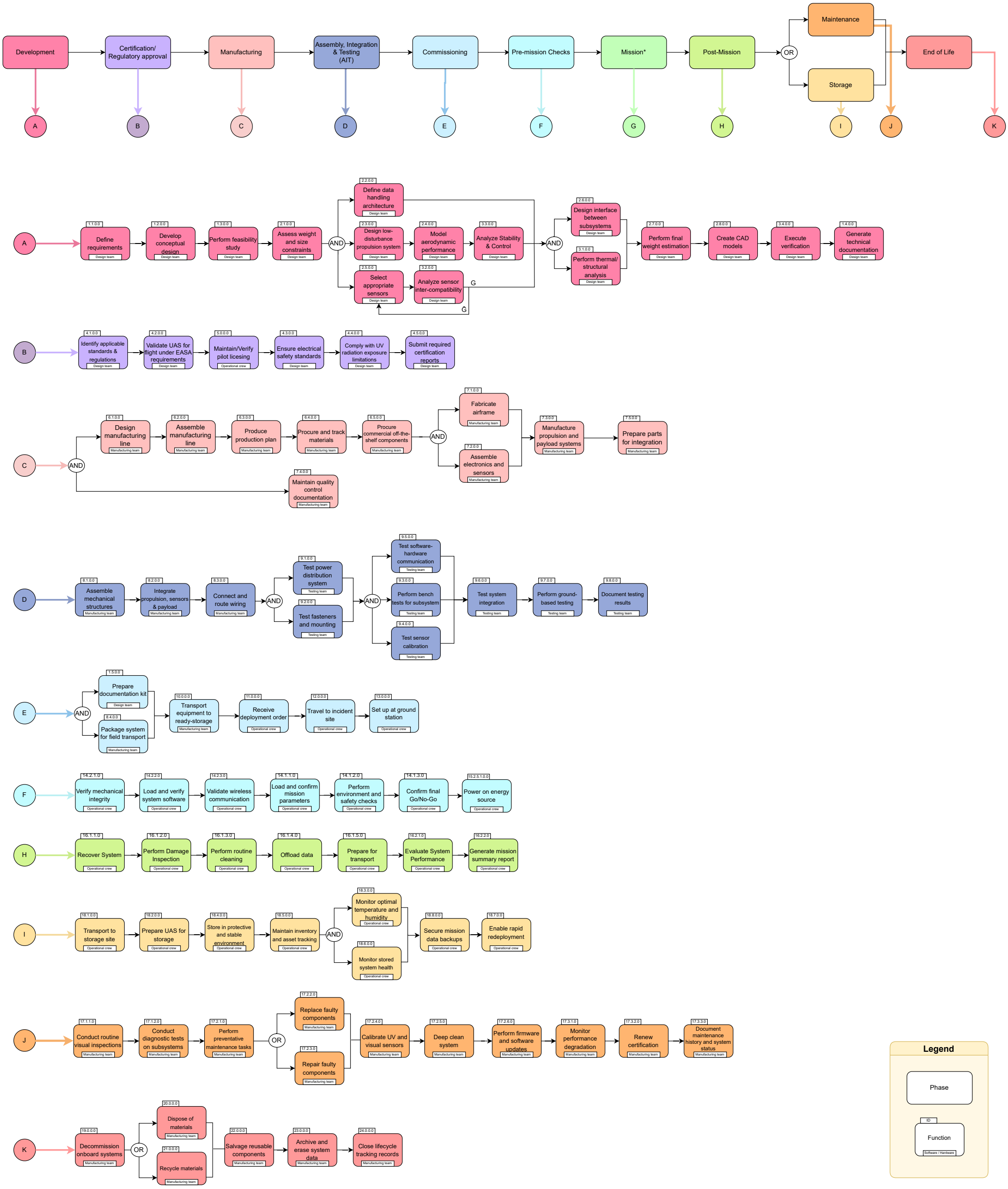

Figure A.2: Functional Flow Diagram

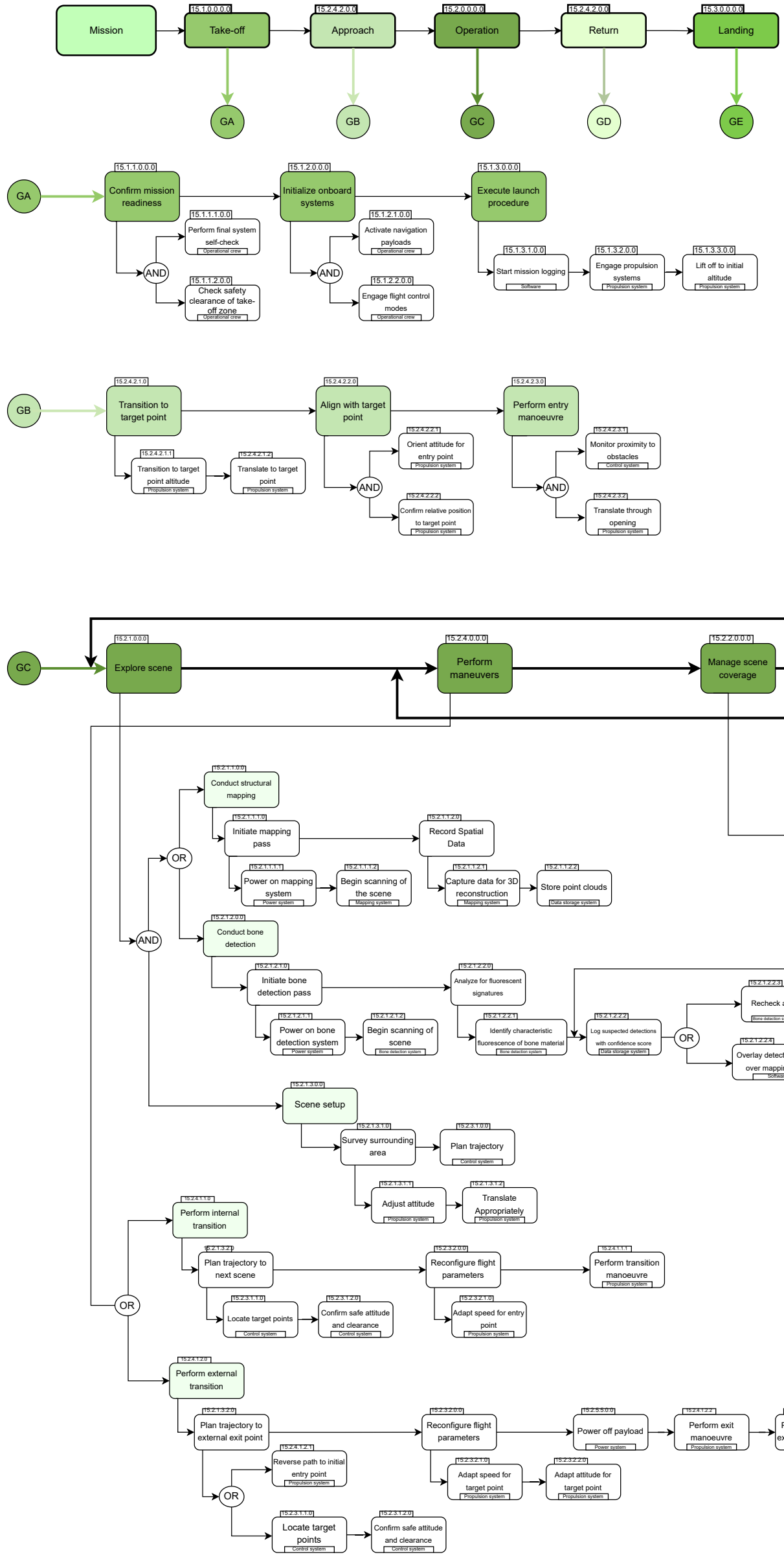

Figure A.3: Functional Flow Diagram of Mission

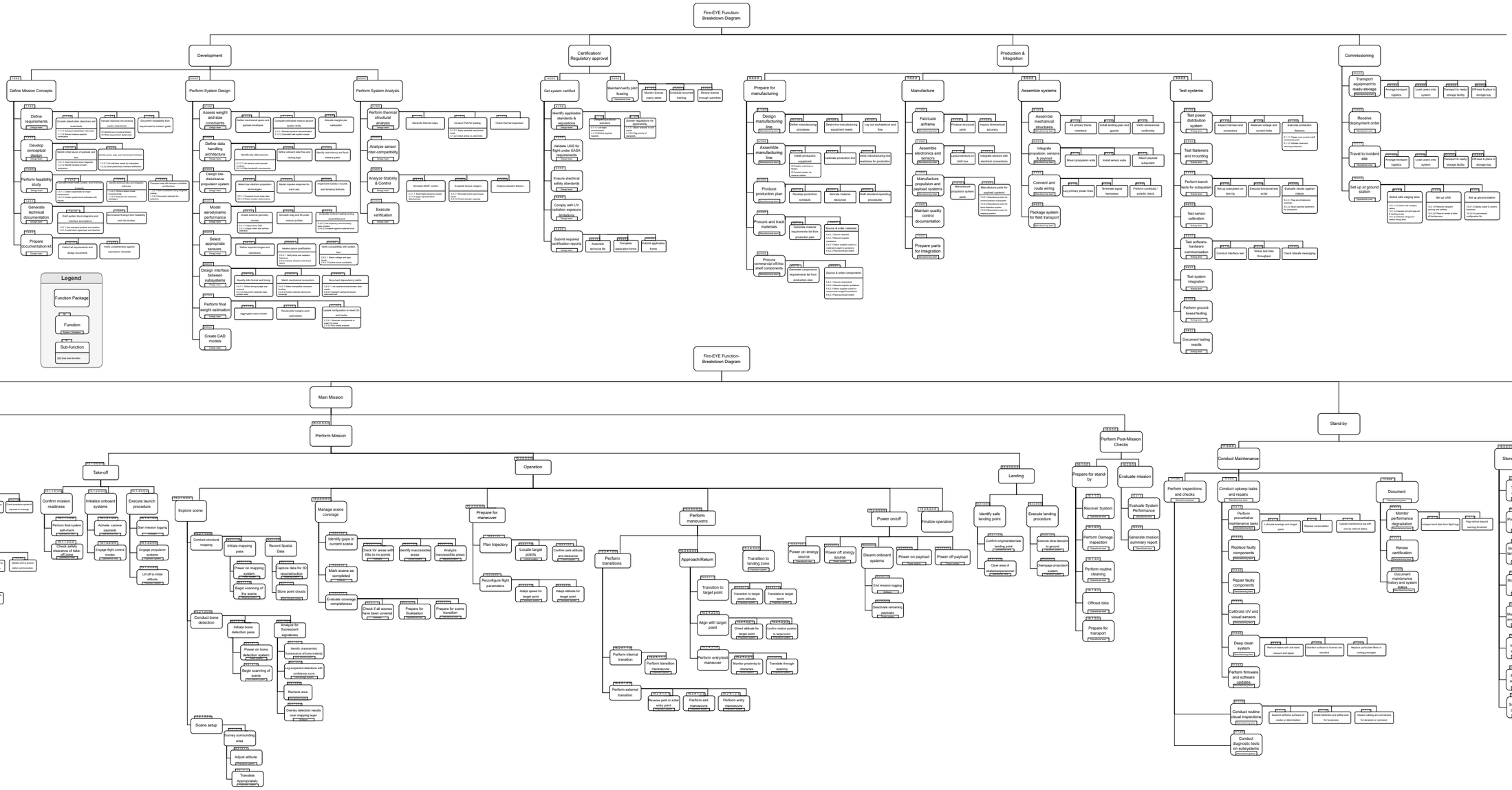

Figure A.4: Functional Breakdown Diagram